CHARACTERIZING THE ROLE OF THE POLYCOMB REPRESSIVE COMPLEX 1 IN THE CONTEXT OF HISTONE-MUTATED PEDIATRIC HIGH-GRADE GLIOMAS

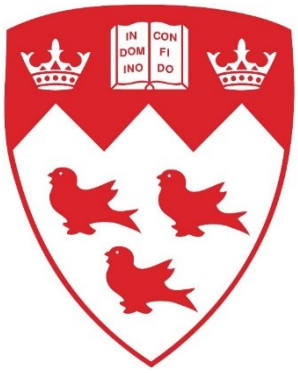

Elias Jabbour

Division of Experimental Medicine, McGill University, Montreal

June 2020

A thesis submitted to McGill University in fulfillment of the Experimental Medicine program requirements for a Master of Science (M.Sc.)

Abstract

Within the increasingly expanding spectrum of glial tumors, high-grade gliomas (HGGs) are one of the most aggressive variants and a leading cause of death by cancer in children. Previous genomic investigations have highlighted that a significant proportion of pediatric HGGs harbor somatic mutation on genes coding for histone proteins. A large proportion of brain midline HGGs including diffuse intrinsic pontine gliomas (DIPGs), an aggressive and invasive subtype of HGGs that arises from regions within the brainstem, have Lysine-to-Methionine missense mutations at residue 27 (K27M) of histone 3 variants (H3). H3-K27M induces an overall decrease in tri-methylated lysine 27 histone mark on H3 (H3K27me3), a post-translational modification associated with gene expression silencing through a series of epigenetic events orchestrated by the Polycomb complex group (PcG): the Polycomb Repressive Complex 1 (PRC1) and 2 (PRC2). Our lab showed that H3-K27M mutations prevents PRC2 from spreading H3K27me3 from CpG islands into repressive domains. While several PcG recruiting mechanisms have been suggested, the general consensus remains that a subset of PRC1 complexes recognize the H3K27me3 mark deposited by PRC2, catalyze the deposition of a repressive ubiquitin molecule on histone H2AK119 or mediate long-range chromatin contacts. Since the H3-K27M mutation has been shown to deregulate H3K27me3 deposition, we hypothesize that PRC1 is redistributed and is involved in tumorigenesis of H3-K27M pHGGs. To this effect, using Chromatin-immunoprecipitation followed by high-throughput sequencing of RING1B (ChIP-seq) (core component), CBX2 (canonical component) and the H2AK119ub modification, we characterized the distribution of PRC1 within the genomes of H3-K27M and isogenic H3-K27M CRISPR/Cas-edited (KO) HGG cell lines. We show increased PRC1 and PRC2 overlap at H3K27me3 sites in H3-K27M mutant cells. Canonical PRC1 was highly

recruited to H3K27me3-enriched promoters but was not associated with global changes in expression. We also observed PRC1 redistribution at promoters in the presence of H3-K27M. Nevertheless, promoters with gain or loss of PRC1 recruitments were not associated with clear changes in gene expression profiles or in their overlap with other histone modifications. While our results show PRC1 redistribution in H3-K27M HGGs, a better characterization of PRC1's contribution to tumorigenesis would require the generation for PRC1-depleted H3-K27M HGG contexts.

Résumé du projet

Dans le spectre, de plus en plus étendu, des tumeurs gliales, les glioblastomes (GBM) sont les variantes les plus fréquentes et les plus agressives chez l'adulte, ainsi que la cause principale de décès par cancer chez l'enfants. Des recherches antérieures ont mis en évidence, qu'une proportion importante de GBM pédiatriques contient une mutation somatique des gènes codants pour des protéines histones. Les gliomes pontiques intrinsèques diffus (DIPG), un sous-type agressif des GBM pédiatriques, ont une mutation faux-sens, Lysine-en-Méthionine, au résidu 27 (K27M) des gènes codants des variants de l'histone 3 (H3). Cette mutation d'histone entraîne une modification des profils de méthylation et d'expression de l'ARN, qui pourraient conduire à la formation et la progression de ces cancers. Des recherches supplémentaires ont prouvé que les régulations épigénétiques de l'expression génique sont altérées suite à la diminution globale de l'histone tri-méthylée de la lysine 27 (K27me3). Ces événements épigénétiques sont généralement orchestrés par une famille de protéines connue sous le nom de complexes Polycomb : Complexe répressif 1 (PRC1) et 2 (PRC2). Malgré les nombreux mécanismes de recrutement suggérés, le consensus demeure que la forme canonnique du complexe PRC1 (cPRC1) reconnaît la marque H3K27me3 déposée par PRC2 et catalyse le dépôt d'une molécule d'ubiquitine sur l'histone H2A. Ceci contribue probablement à la repression de l'expression des gènes et à la compaction de la chromatine. Comme il a été démontré que les mutations H3-K27M dérèglent les dépôts de H3K27me3, nous émettons l'hypothèse que la redistribution de PRC1 est impactée par cette dérégulation et a un impact sur le développement des GBMs H3-K27M.

En utilisant l'immunoprécipitation à la chromatine (ChIP) suivie d'un séquençage à haut débit de RING1B (facteur central), CBX2 (facteur canonique) et de la modification H2AK119ub, nous

avons pu caractériser la distribution de PRC1 dans les génomes des lignées cellulaires H3-K27M et leurs contrôles H3-K27M KO. Nous observons une accumulation de PRC1 et PRC2 couplée aux sites de H3K27me3 dans les conditions H3-K27M. cPRC1 est fortement recruté au niveau des promoteurs enrichis en H3K27me3 mais n'est pas associé à des changements globaux au niveau de la transcription. Nous observons également une redistribution de PRC1 aux promoteurs dans les conditions H3-K27M. Cependant, le recrutement de PCR1 aux promoteurs n'était pas clairement associé à des changements d'expression ou à des modifications d'histones. Notre approche a mis en évidence un modèle de redistribution de PRC1 qui justifie à l'avenir la génération des modèles knock-out de PRC1 pour une meilleure caractérisation de sa contribution à la formation de ces GBMs.

Table of Contents

List of Abbreviations

1p/19q: short arm of chromosome 1 and long arm of chromosome 19

ATAC-seq: Using Assay for Transposase-Accessible Chromatin using sequencing

ATCC: American type culture collection

ATRX: Alpha-Thalassemia/Mental Retardation Syndrome X-Linked

CBTRUS: Central Brain Tumor Registry of the United States

CBX: Chromodomain protein

CGI: CpG-rich island

CGIs: CpG-rich islands

ChIP: Chromatin immunoprecipitation

CNS: Central Nervous System

cPRC1: canonical Polycomb Repressive Complex 1

CRISPR: Clustered Regularly Interspaced Short Palindromic Repeats

DIPG: Diffuse Intrinsic Pontine Gliomas

EED: Embryonic Ectoderm Development protein

EZH1: Enhancer of Zest 1

EZH2: Enhancer of Zest 2

G34R: Glycine-to-Arginine substitution at residue 34

G34V: Glycine-to-Valine substitution at residue 34

GBM: glioblastoma

H1: Histone Protein 1

H2A: Histone Protein 2A

H2AK119ub: mono-ubiquitinated lysine residue 119 of H2A

H2B: Histone Protein 2B

H3.1: Histone Variant 3.1

H3.2: Histone Variant 3.2

H3.3: Histone protein variant 3.3

H3: Histone protein 3

H3K27ac: Acetylated lysine residue 27 of histone 3

H3-K27M: Lysine-to-methionine mutation of residue 27 of histone 3

H3K27me1: monomethylated lysine residue 27 of histone 3

H3K27me3: demethylated lysine residue 27 of histone 3

H3K27me3: trimethylated lysine residue 27 of histone 3

H3K4me1: trimethylated lysine residue 4 of histone 1

H3K4me3: trimethylated lysine residue 4 of histone 3

H4: Histone Protein 4

HDAC: Histone Deacetylase

Hox: Homeotic

IDH: Isocitrate Dehydrogenase

IDH: Isocitrate Dehydrogenase

K27M: Lysine-to-methionine mutation of residue 27

K27me3: trimethylated lysine residue 27

LINE: Long Interspersed Nuclear Element

lncRNA: long non-coding RNA

LTR: Long terminal repeats

mESC: mouse Embryonic Stem Cells

MGMT: O6-methylguanine-DNA methyltransferase

NCI: National Center Institute

NF-1: Neurofibromatosis type 1

PcG: Polycomb Group

PCL: Polycomg-like homolog proteins

Ph/HPH: Polyhomeotic homologous protein

pHGG: pediatric high-grade glioma

PRC1: Polycomb Repressive Complex 1

PRC2: Polycomb Repressive Complex 2

PRE: Polycomb Response Elements

PRE: Polycomb Response Elements

RING1: Really Interesting New Gene

SAM: sterile alpha motif

SEER: Surveillance, Epidemiology and End Results

SINE: Short Interspersed Nuclear Element

SUZ12: Suppressor of Zeste 12

TCGA: The Cancer Genome Atlas

TERT: Telomerase Reverse Transcriptase

TF: Transcription Factors

TrxG: Trithorax Group

WHO: World Health Organization

List of Figures

List of Tables

Acknowledgments

Upon the completion of this thesis, I would be concluding a life-altering two-year chapter at McGill University. As a first-generation college student, this graduate degree represents yet another educational milestone for myself as well as my family who has relentlessly supported me throughout the years. **To all fellow first-generation, underprivileged and minority scientists, this one is for you!**

I cannot begin to describe the many ways in which these two years have been my absolute best and my absolute worse. My journey in research has been, for the lack of better words, a love/hate relationship: I hated every failure, I relished every success and more frequently, vice-versa. Nonetheless, this experience has been quite representative of life as a whole. As I have learned by heart now, life is always tough, but one needs to find peace within its chaos to enjoy it and thrive. Certainly, there are numerous lessons that I have acquired throughout this academic journey on both a professional and, most importantly, a personal level. These are life-long realizations that I will strive to carry with me throughout the different walks of my career, and I would have never reached them had it not been for the astounding support I received from the Nada Jabado laboratory:

Michele, you have been a colleague, a mentor, a friend and a sister to me throughout these past two years. You have cheered with me at every high time and was there for me at every low time. I would have never imagined I could learn so much from a single person, let alone an entire degree. You are a walking institution and I am very blessed to have crossed paths with you. Words will not do justice to the impact and inspiration you have left on me. You were a role

model for values I now learned how to live by, and I am eager to see the many successes you are still to reach.

Ashot, you adopted me as a supervisee when nobody would (literally, even you did not want to). You have tolerated all my flaws and were always a reference I could go to. I have learned so much from you, whether in terms of my "Nobel Prize Worthy"- ChIP-seq experiments or almost everything else. You have guided me academically, professionally, scientifically and (profoundly) personally. I have learned from you the importance of patience and I am very grateful for all the time you have spent teaching me. At many times you were the only person listening when everyone else was only hearing me. Maybe I do not show it often and I always give you a hard time, but you are truly one of my few role models. Effortlessly, you have shown me what a true scientist is, and I shall strive to live by the ethical principles and values you have bestowed upon me.

Djihad, you revitalized my passion for science and research. You made time for me every time I needed assistance and even took on my supervision as your responsibility. We quickly became a team and developed passion for our project. Working with you has been immensely rewarding, motivating and enjoyable. You truly re-ignited my faith in Science, and I cannot begin to describe how grateful I am for having been under your mentorship!

Cathy and Damien, you have both been true parents to me in the lab. You immensely helped me out in whatever ways you could and supported me throughout my many optimization steps. I know for a fact that you will miss me when I leave because I guarantee you that I will miss working with you even more.

Andrea, Shakour and Shriya, I am very happy that you all survive my constant badgering, singing and jokes. Working with you, or alongside you, has been quite rewarding. You all generously provided practical or conceptual assistance whenever I needed it and were there to support me whenever I needed to release some heat. I wish you all the best of luck in your future endeavours!

While I would like to share my appreciation in detail for every member I have worked with, I am highly limited by the page numbers of this draft. Therefore, I would like to thank Amira for her early assistance and for sharing all her research tricks, Leonie and Nikoleta for all their relentless administrative help, their prompt assistance and their words of encouragement, Augusto and Gaya for their energy and for making lab-work so dynamic. Finally, Adam… I am going to leave it blank for you.

Finally, I would like to thank Dr. Nada Jabado for providing me with an astounding platform and opportunity. You have provided me with unwavering support from my initial recruitment up until the very last moment. You believe in my potential and were always the choice of my role model discussion throughout all my interviews. Undoubtedly, I have learned so much from your constant supervision and developed from your exquisite guidance a true passion for a multidisciplinary career.

Contribution of Authors

Chapter 1: Literature Review and Introduction

Chapter 1 was drafted by the MSc candidate, Elias Jabbour. Editorial review was done by Dr. Ashot Harutyunyan and Dr. Nada Jabado (Supervisor).

Chapter 2: Rationale and Hypothesis

Chapter 2 was drafted by the MSc candidate, Elias Jabbour. Editorial review for this part was done by Dr. Ashot Harutyunyan and Dr. Nada Jabado (Supervisor).

Chapter 3: Materials and Methods

Chapter 3 was drafted by the MSc candidate, Elias Jabbour. Editorial review for this part was done by Dr. Michele Zeinieh and Dr. Nada Jabado (Supervisor).

Chapter 4: Results

Chapter 4 was drafted by the MSc candidate, Elias Jabbour. Editorial review for this part was done by Dr. Djihad Hadjadj and Dr. Nada Jabado (Supervisor).

Figure 3 was used from Springer Nature. March 19, 2019 (open source, no permission was needed). (https://creativecommons.org/licenses/by/4.0/)

All ChIP-seq and Western blot experiments for RING1B, CBX2 and H2AK119ub (in all cell lines) were performed by the MSc candidate, Elias Jabbour.

Other ChIP-seq, RNA-seq experiments and CRISPR/Cas9 H3-K27M KO models were already performed by members of the Dr. Nada Jabado Laboratory as in Harutyunyan et al. (12) and Krug et al. (13) as highlighted in Chapter 3.

All figures and analyses were performed by the MSc candidate, Elias Jabbour.

Chapter 5: Discussions

Chapter 5 was drafted by the MSc candidate, Elias Jabbour. Editorial review for this part was done by Dr. Djihad Hadjadj and Dr. Nada Jabado (Supervisor).

Chapter 6: Conclusion

Chapter 6 was drafted by the MSc candidate, Elias Jabbour. Editorial review for this part was done by Dr. Djihad Hadjadj and Dr. Nada Jabado (Supervisor).

Chapter 7: Future directions

Chapter 7 was drafted by the MSc candidate, Elias Jabbour. Editorial review for this part was done by Dr. Djihad Hadjadj and Dr. Nada Jabado (Supervisor).

Chapter 1: Literature Review and Introduction

1.1 Epidemiology of pediatric high-grade gliomas

Gliomas are the most common central nervous system tumor in children (1, 13). While most of these tumors are classified as low-grade gliomas and have very promising survival rates that extend, in 87% of cases, to 20 years or more, 30% of gliomas are of higher grade and are associated with inferior outcomes (1). Pediatric high-grade gliomas (pHGGs) are a heterogenous group of tumors that annually affect 0.86 children per 100,000 (1, 34, 37). As the leading cause of cancer-related deaths in children, pHGGs are classified by the WHO as grade III (anaplastic astrocytoma) or grade IV tumors (glioblastoma) (1). Even among survivors, these tumors constitute a significantly higher rate of morbidity (37).

Statistical studies by the Central Brain Tumor Registry of the United States (CBTRUS) show an increase pHGGs incidence between 2007-2011 and 2012-2016 across age groups (1). Similarly, a report from the NCI's Surveillance, Epidemiology and End Results (SEER) program displays a significant increase in HGG incidence rates with an average annual change of 3.01% (1). Nonetheless, this rise can be explained by the development of new diagnostic tools, the adoption of more precise classification criteria as well as changes in reporting frequencies (1). While many studies have attempted to unravel potential environmental risk factors associated with gliomas, none have hitherto been able to establish a significant causal relationship (1). Prior exposure to radiation, seen more frequently in adult populations, remains the only tentative etiological factor associated with HGGs (38). Additionally, many genetic syndromes are known to be associated with these tumors; most notably, Turcot syndrome, Li-Fraumeni and Neurofibromatosis type 1 (NF-1) syndrome (38).

1.2 Clinical Presentations and Treatment

Patients diagnosed with pHGGs manifest various symptoms that are largely determined by tumor location and individual age (1). Interestingly, the duration between onset of symptoms and diagnosis is inversely related to tumor grade, whereby high-grade gliomas are diagnosed sooner than their low-grade counterparts upon initial symptom manifestation (1).

Focal symptoms include weakening of one or both sides of the body (homo/monoparesis), dysphasia, aphasia and recent memory impairment (38). Some symptoms may arise due to the increased cranial pressure and may include headaches, nausea and emesis (38). While most headaches are non-glioma related, it is specifically headaches that awaken children from sleep, involve vomiting or progress in severity which warrant further imaging investigations (38). It should be mentioned that infants tend to experience more skull elasticity which delays symptoms related to intracranial pressure thus rendering diagnosis more challenging (1).

Clinically, proliferation index assessment shows an overall inverse relationship between division rate and progression-free survival; however, recent studies highlight better associations between prognosis and molecular classification (explained below) that are independent of proliferation indices (38).

Maximal surgical tumor resection remains key in managing high-grade gliomas both in children and adults (38). Tumor resection allows for the obtention of tissue for pathological assessments, alleviates intracranial pressure and reduces tumor volume (38). Given that high-grade gliomas are widely infiltrative, it is often burdensome to distinguish normal and malignant tissue boundaries intra-operatively (38). This is further exacerbated by the need to maximally preserve neural functions (38). While many studies have assessed the success of different therapeutic approaches,

whether surgical, chemical, radiative or a combination of those, none of them incorporate the distinct molecular characterization of these tumors introduced next (38).

While treatment of high-grade gliomas has changed and evolved throughout the past 10 years, the standard method of care remains at the level of maximal surgical resection followed by chemotherapy and radiation (116). Specifically, Temozolomide, an orally administrated alkylating agent, is increasingly being used for the treatment of high-grade gliomas (116, 117). Focal radiotherapy is currently the standard method of care for children with high-grade gliomas and has been shown to increase survival by 3 months (118). While many mutated genes and altered signaling pathways have been characterized in high-grade gliomas, most trials of single-agent targeted therapies have shown little promising results – an effect that was largely due to the significant molecular heterogeneity of these tumors (116). This serves to highlight the importance of molecular characterizations of each tumor as a key approach for the proper development of therapeutic regimen (118).

1.3 Molecular classification of high-grade gliomas

The large spectrum of gliomas can be clustered into two categories: “diffuse gliomas” and “non-diffuse gliomas” based on growth patterns (4). The significant increase in the molecular understanding of Central Nervous System (CNS) tumors has motivated the incorporation of molecular diagnostics into the characterization of gliomas (4). Until the 4th edition of the World Health Organization (WHO) Classification of Tumors of CNS, these molecular characteristics were used solely as supplemental information to tumors which were mainly defined by their histology (4). Growing evidence that a “combined molecular-histological” approach may be superior in diagnosing tumors has paved the way for a fundamental change in brain tumor classification (4). This notable change in classification was a central aspect of the 4th edition of the

WHO classification of CNS tumors released in 2016, whereby several categories now, partly or entirely, incorporate genotypic definitions (4).

Gliomas constitute a very diverse range of intrinsic central nervous system tumors with glial precursor cell lineage as suspected cells of origin (4). The first group of gliomas, known as diffuse gliomas, is characterized by the large infiltration of tumors into the neighboring brain parenchyma (4). In contrast, the second group shows more restricted growth patterns and is known as non-diffuse gliomas (4). Diffuse gliomas are the most frequent glioma subtype and include three separate tumors: diffuse astrocytoma, oligodendrogliomas and oligoastrocytomas (mixed oligodendroglial and astrocytic phenotype) (4). Recurrent point mutations in the isocitrate dehydrogenase 1 and 2 (*IDH1/2*) in WHO grade II and III diffuse gliomas (all three subgroups), as well as secondary glioblastomas arising from low-grade tumors, has encouraged the inclusion of these molecular diagnostics in glioma classifications (4). In fact, diffuse gliomas, with similar histology, showed different clinical outcomes that were better associated with the mutation state of the *IDH* genes (4). This observation subsequently drove the decision to incorporate *IDH* mutation as a diagnostic marker for the characterization of gliomas (4). Similarly, *IDH* mutation state was closely associated with the complete 1p/19q codeletion (short arm of chromosome 1 and long arm of chromosome 19) (4). In fact, studies eventually demonstrated that *IDH* mutant gliomas can further be separated into two groups (4). The first group shows presence of *IDH* mutations, the 1p/19q codeletion and Telomerase Reverse Transcriptase (*TERT*) promoter mutation, which characterizes oligodendrogliomas (4). In contrast, the second group shows presence of *IDH* mutations, Alpha-Thalassemia/Mental Retardation Syndrome X-Linked (*ATRX*) and *TP53* mutations without the 1p/19q codeletion and is specific to astrocytoma (4). It should be noted that

these molecular associations were found to supersede histological appearances and are more accurate for diagnosing *IDH*-mutant diffuse gliomas (4).

Of interest to this study, histone 3 K27M mutant gliomas were added to the WHO list of diffuse glioma molecular classification (4, 63). This neoplasm is characterized by astrocytic differentiation patterns and the presence of a Lysine-to-Methionine substitution on residue 27 of the histone 3 protein coded by either *H3F3A* or *HIST1H3B/C* genes (4, 63). These tumors frequently occur in children and are located in the brainstem (ventral pons), spinal cord and/or thalamus (4, 63). While these neoplasms show variable histology and grading, their aggressive progression and poor prognosis unanimously define them as WHO grade IV (4, 63). These mutations occur in 80% of midline HGG and are now recognized as a distinct entity of the 2016 WHO classification of central nervous system tumors (63).

While non-diffuse gliomas are not directly relevant to this study, it is important to highlight that these malignancies often include ependymomas, pilocytic astrocytoma and are also associated with characteristic molecular alterations (4).

1.4 (Epi)genetics of High-grade Gliomas

Within the increasingly expanding spectrum of glial tumors, high-grade gliomas are the most common and aggressive type and are associated with a 10% survival rates only two years after diagnosis (1, 2, 3). These tumors show great molecular differences between children and adults (4, 5). Previous lack of understanding of these distinctions drove many efforts, including our group, to unravel the molecular characteristics of pediatric gliomas (4, 5, 6).

Early genomic investigations have highlighted that a significant proportion of pediatric HGGs harbor somatic mutation in genes coding for histone proteins. Histones are key proteins involved

in the maintenance of chromatin structure and the regulation of gene expression (63). Histones assemble into octamers (H2A, H2B, H3 and H4) that bind to DNA to form secondary structures and regulate transcriptional access (63). Genes coding for histone protein H3, in specific, are found to frequently harbor somatic mutations in HGGs (63). In fact, the presence of such mutations is strongly correlated with tumor type, age of afflicted patients and cells of origin (2, 11, 13). Such histone mutant HGGs comprise around a third of total pediatric glioblastoma cases and are further subdivided into specific recurrent mutation groups highlighted below (11).

Diffuse intrinsic pontine gliomas (DIPGs), an aggressive and invasive subtype of pediatric HGGs that arises from regions within the brainstem, shows a Lysine-to-Methionine missense mutation at residue 27 (K27M) of the histone 3 variant (H3) genes: either *H3F3A* (70-80%, H3.3 variant) or *HIST1H3B/C* (18%, H3.1 variant) (5, 7, 8, 12, 13). H3-K27M diffuse gliomas were unequivocally associated with poor prognosis and more aggressive clinical patterns in children even when they demonstrated low-grade histological characteristics (7). A second recurrent histone mutation, Glycine-to-Valine/Arginine (G34R/V) at residue 34 of the protein variant H3.3, is found in tumors of older pediatric populations (young adolescents), arise from supratentorial regions of the brain and is associated with a better prognosis (7, 8, 9, 17). The association between histone 3 mutations, different spatiotemporal contexts and tumor aggressivity hints at the exquisite connection between epigenetic deregulation events and specific neuro-development windows (17).

Histone H3.3-K27M mutations, which will be the focus of this study, are present in the majority (>70%) of high-grade infiltrative midline gliomas arising from the thalamus, pons or spinal cord (7). The histone H3.3 variant is known to be associated with transcriptionally active regions, open chromatin conformations and telomeres (34). Nonetheless, there exists a total of 30 different histone 3 variants, which explains the limited contribution (3-17%) of histones harboring these

point mutations to the total histone 3 pool (11). However, the small proportion of mutated histones was found to be sufficient in leading to global molecular and epigenetic changes driving tumorigenesis (5).

While the H3-K27M mutation is arguably strong driver of tumorigenesis, it is often associated and cooperates with other genomic alterations (7). For instance, they are frequently accompanied by *TP53* and *ATRX* (chromatin remodeler) mutations (7). Similarly, a subset of H3-K27M diffuse midline gliomas were associated with missense point mutations that affect *ACVR1,* a gene encoding activin A receptor type-1 membrane protein (7). These mutations were found to constitutively activate the BMP-TGFβ signaling pathway and contribute to tumorigenesis (7). It should be noted that the presence of H3-K27M mutation is mutually exclusive with the *IDH1* mutations mentioned above (7).

While several cooperating mutations have been enumerated above, it should be mentioned that these only represent a subset of the genes usually affected in GBMs. For instance, studies using GBM and LGG datasets from The Cancer Genome Atlas (TCGA) have shown that at least one out of 36 genes implicated in the organization of chromatin were subject to genetic alterations in 54% of these tumors (6). Most notably, genes coding for Histone Lysine methyltransferases (*SETD2*), DNA methyltransferases and chromatin configuration ATPases (*SMARCA4* and *ARID1A*) are found mutated in 1-3% of gliomas (6, 115).

1.5 Polycomb Repressive Complexes

1.5.1 Introducing PRC1 and PRC2

During development, epigenetic regulation of genes is one of the most prominent mechanisms through which cell-identity and cell-fate are defined (10). Among these chromatin

regulatory systems, the Polycomb (*PcG*) and the Trithorax groups (*TrxG*) are key evolutionarily conserved processes that work antagonistically to modulate gene expression during differentiation (10). First identified in Drosophila 70 years ago, *PcG* genes were thought to only regulate Homeotic *(Hox)* genes since mutations in many members of the Polycomb groups led to embryonic transformations and developmental aberrations (10). Soon enough, more members of *PcG* and *TrxG* were found to be implicated in other biological processes such as proliferation, senescence and cancer (10).

Polycomb complexes, which will be the center of this study, are recruited to specific DNA segments known as the Polycomb Response Elements (PREs) in Drosophila (10). These then modulate gene expression by modifying chromatin state at targeted genes through chromatin remodeling and/or post-translational modification of the N-terminal tail of histone proteins (10). By doing so, they drive the inheritance of silenced or active chromatin conformations through normal (and abnormal) development and differentiation (10). In mammalian systems, unmethylated GC-rich regions, known as CpG islands or CGIs, recruit PcG complexes similarly to PREs in drosophila (10).

Biochemical purification analyses have led to the identification of two main PcG machinery: Polycomb Repressive Complex 1 (PRC1) and Polycomb Repressive Complex 2 (PRC2) (10). These two complexes show a significantly greater diversity and complexity in mammals then in drosophila (10).

Despite their diverse assemblies in mammals, both PRC1 and PRC2 consistently incorporate specific core factors (10). PRC1 complexes all share a highly conserved core catalytic factor, RING1 (either RING1A or RING1B), which then associates with one of the 6 Polycomb Group Ring-Finger domain proteins (PCGF1-6) (10). This core assembly mediates the catalysis of a

single ubiquitin molecule on histone H2A lysine residue 119 (H2AK119ub) (10). Meanwhile, the functional core of PRC2 in mammals requires the presence of one of the two SET-domain-containing histone methyltransferase enhancer of zeste (EZH1 or EZH2), the suppressor of zeste protein (SUZ12), embryonic ectoderm development protein (EED) and CAF1 histone-binding proteins RBBP4/7 (10). This core assembly mediates the catalysis of another type of post-translational modification (mono-/di-/tri-methylation) on histone H3 lysine 27 residues (H3K27me1/2/3) (10).

Initially suspected to be repressive, PRC1-mediated H2AK119ub deposition is dispensable for gene repression as seen in mice and drosophila studies (10). This is in contrast with PRC2-mediated methylation of H3K27 which shows a stronger repressive role (10). Nonetheless, growing evidence hints at the repressive function of H2AK119ub in specific sites (21, 51). For instance, H2AK119ub deposition impairs the placement of active H3K4me3 around promoters and is involved in RNA polymerase II pausing (42).

1.5.2 Complexity of Assembly of PRC1 and PRC2

PRC1, studied here, assembles into either canonical or non-canonical subtype of complexes (10). Core components PCGFs are able to bind to different accessory proteins due to minor alterations in their RAWFUL domain and consequently lead to formation of these different PRC1 complexes (PRC1.1-1.6) (15). Canonical PRC1 (cPRC1) incorporates PCGF2/4 proteins in association with RING1A/B and are usually defined by the presence of one of the 5 human chromobox proteins (CBX2, CBX4, CBX6, CBX7 and CBX8) (10). These CBX proteins allow for PRC1 to recognize methylated H3K27 residues (catalyzed by PRC2) and leads to one of many suggested dynamic interplays between PcG complexes (10). In addition, cPRC1 are composed of a Polyhomeotic homologous (Ph) protein (PHC1, PHC2 or PHC3) (10). These PHCs contain a

domain known as the sterile alpha motif (SAM) which is essential for the PcG-mediated chromatin long-range looping activity of PRC1 (10). In contrast, non-canonical PRC1 complexes (ncPRC1) are composed of either one of the 6 PCGF proteins in association with the RING1 catalytic factor but are devoid of CBX proteins (10). In ncPRC1, a zinc-finger domain and YY1-binding protein (RYBP) or its paralog (YAF2) occupy the CBX binding site and define ncPRC1 (10). Non-canonical PRC1 complexes then uniquely associate with a panoply of other accessory proteins to form diverse subtypes of PRC1 complexes (ncPRC1.1, ncPRC1.3/5 and ncPRC1.6) (10). Given the multitude of different associations that each PCGF can form with combinations of accessory proteins, it is instinctive to mention that binding affinities, recruitment mechanisms and gene regulatory functions of ncPRC1s greatly differ and are still the subject of numerous investigations in the field (15).

While some studies have shown the possible association of PCGF2/4 with RYBP in formation of ncPRC1.2/4, the most defined complexes remain at the level of PCGF1, PCGF3/5 or PCGF6 (10). For simplicity, a table is provided below that illustrates the identified constituents of each of the aforementioned ncPRC1 complexes (10):

Table 1. Table showing the different accessory proteins that associate with each subtype of non-canonical PRC1 complexes.

Complex	**Accessory Proteins**
ncPRC1.1	KDM2B, BCOR, SKP1A, USP7
ncPRC1.3/5	AUTS2, CK2, FBRS, WDR5, DCAF7
ncPRC1.6	CBX3, E2F6, HDAC1, HDAC2, MAX, MGA, TFDP1, WDR5, L3MBTL2, EHMT1

Similarly, PRC2 demonstrates diverse compositions through its association with different non-stochiometric subunits that are known to regulate its activity (10). Proteomic analyses in human cells have identified two alternative assemblies of PRC2: PRC2.1 and PRC2.2 (10). PRC2.1 is defined by the presence of one of the three mutually exclusive Polycomb-like homolog proteins (PCLs): PHF1, PHF19 or MTF2 (10). Currently under rigorous investigation, these PCLs are suspected to enhance the catalytic activity of EZH2 towards the H3K27me3 mark state (10). In contrast, PRC2.2 incorporates zinc-finger proteins JARID2 and AEBP2 which also enhance the catalytic and chromatin binding activity of PRC2 (10). These diverse assemblies also confer upon PRC2 different recruitment abilities as highlighted next (10).

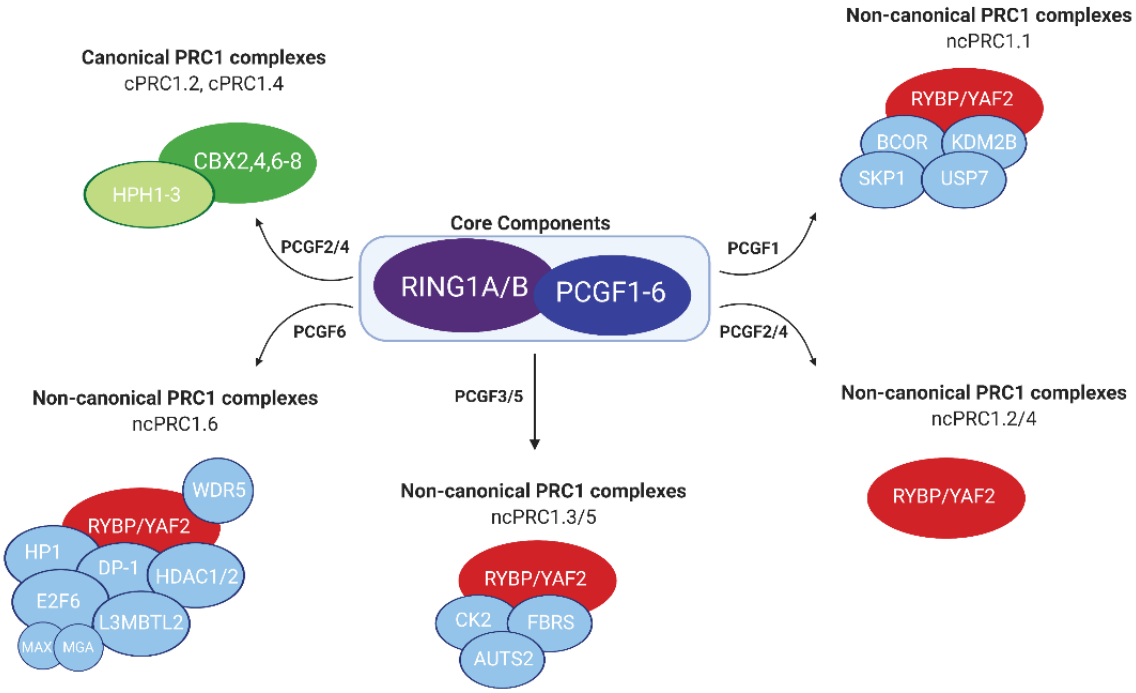

Figure 1. Illustration showing the different compositions of PRC1 complexes.

Core constituents RING1A/B and PCGF1-6 are common to all PRC1 complexes and define the catalytic activity of PRC1. This core assembly then associates with PCGF2/4 to form canonical PRC1 complexes and recruits CBX and HPH factors. Non-canonical PRC1 complexes can incorporate any of the 6 PCGFs in the absence of CBX proteins. In ncPRC1 complexes, RYPB/YAF2 substitute for CBX and associate with different accessory proteins to define numerous non-canonical variants.

Created using BioRender.com

1.6 PcG recruitment

Originally, recruitment of PcGs was thought to be hierarchal whereby PRC2-mediated H3K27me3 deposition leads to the subsequent recruitment of PRC1 through CBX incorporation (reader of H3K27me3) (10). More recently, multiple genome-wide analyses have identified many PcG sites occupied by PRC1 yet devoid of H3K27me3 (10, 28, 62). Similarly, not all PRC2 sites showed PRC1 enrichment in ESCs (28). These observations have then welcomed many other

recruitment hypotheses that include both PcG-interplay and PcG-unique mechanisms (10). Also, studies have unraveled the potential interaction of PcG with transcription factors as a means of recruitment to target sites (10, 16). Some long non-coding RNAs (lncRNAs) can also recruit PcG complexes, but their specific role remains under investigation (10, 27). Here we will focus on the two prevalent modes of recruitment which are increasingly being adopted by the scientific community.

As highlighted above, PcG complexes show enrichment at unmethylated CpG islands which are suspected to be the equivalent of Drosophila PREs in mammalian systems (21, 28). Initially, a "canonical recruitment" model was adopted whereby PRC2 is recruited first, mediates the deposition of H3K27me3 and subsequently attracts PRC1 (21, 28). Alternatively, studies have recently reported a "non-canonical recruitment mechanism" whereby ncPRC1 localization to CGIs and deposition of H2AK119ub precede PRC2 recruitment (21, 24). In this model, JARID2, a sub-stochiometric component of PRC2.2, recognizes H2AK119ub and helps tether PRC2 to PcG target sites (21, 24, 29). This mechanism is heavily implicated in Xist-mediated Polycomb repression inactivation of the X chromosome (21, 24, 29).

As mentioned earlier, the canonical model was then challenged by the independent occupancy of PRC1 to some CGIs, the presence of H2AK119ub at sites devoid of PRC2 and the large maintenance of PRC1 recruitment pattern and catalytic activity in systems lacking PRC2 (21). Soon enough, a PRC2-independent biological link between unmethylated CGIs and PRC1 was discovered that includes KDM2B's association to a subset of PRC1 complexes (21). ncPRC1.1, of specific interest to our neuronal context, is recruited to unmethylated CGIs through the ZF-CxxC domain of the KDM2B it incorporates (16, 21). This provides an alternative mechanism of

PRC1 recruitment independent of H3K27 modifications (16, 21). PRC1 recruitment to these CGIs was equally important for gene repression through H2AK119 ubiquitination (16, 21).

Similarly, ncPRC1.6, defined by the presence of PCGF6, was found to cluster unique sites of PRC1 recruitment independent of PRC2 components (21). Interestingly, ncPRC1.6 overlapped with MGA/MAX and E2F6 transcription factors and was later shown to interact with these factors to illustrate yet another modality through which PRC1 can independently be recruited to chromatin (21).

It eventually became apparent that only PRC1 complexes incorporating PCGF2/4 and CBX proteins depend on the presence of H3K27me3 for recruitment (21). This subset of PRC1 complexes, better known as cPRC1, show a great dependency of PRC2 and mediate little H2AK119ub deposition when compared with their ncPRC1 counterparts (21).

It was only recently that these two recruitment pathways were simultaneously and more clearly addressed (28). Using mESC lacking either cPRC1 (CBX7), PRC2 (EED and SUZ12) or ncPRC1 (RYBP) essential components as well as systems with combinatorial inactivation of these different PcG complexes, it became clear that the two aforementioned pathways work in well-defined contexts (28). These two pathways co-occurred at only 15% of PcG target sites and were both required for the maintenance pluripotency of mESC (28). In fact, it was only the simultaneous disruption of the two recruitment pathways that pushed mouse embryonic stem cells to differentiate (28). Interestingly, disruption of only one of either the PRC2-independent or PRC2-dependent PRC1 recruitment mechanism was largely compensated by the other which was then enough to maintain repression of target genes (28). This redundancy in PRC1 recruitment prevented the ectopic expression of lineage-specific genes and maintained stem-cell properties in mESC by hampering access to TFs and halting RNA polymerase II elongation (28). Nonetheless,

there were many genomic sites that exclusively showed PRC1 recruitment using only one of the two suggested pathways and where disruption of one pathway did not show compensation by the other (28). Unfortunately, a more contextualized understanding of the two recruitment mechanisms is still lacking up until this date (28). Nevertheless, the panoply of recruitment mechanisms highlights functional redundancies that maintain essential epigenetic regulation across cell divisions and developmental timeframes through a combination of different interactions (16).

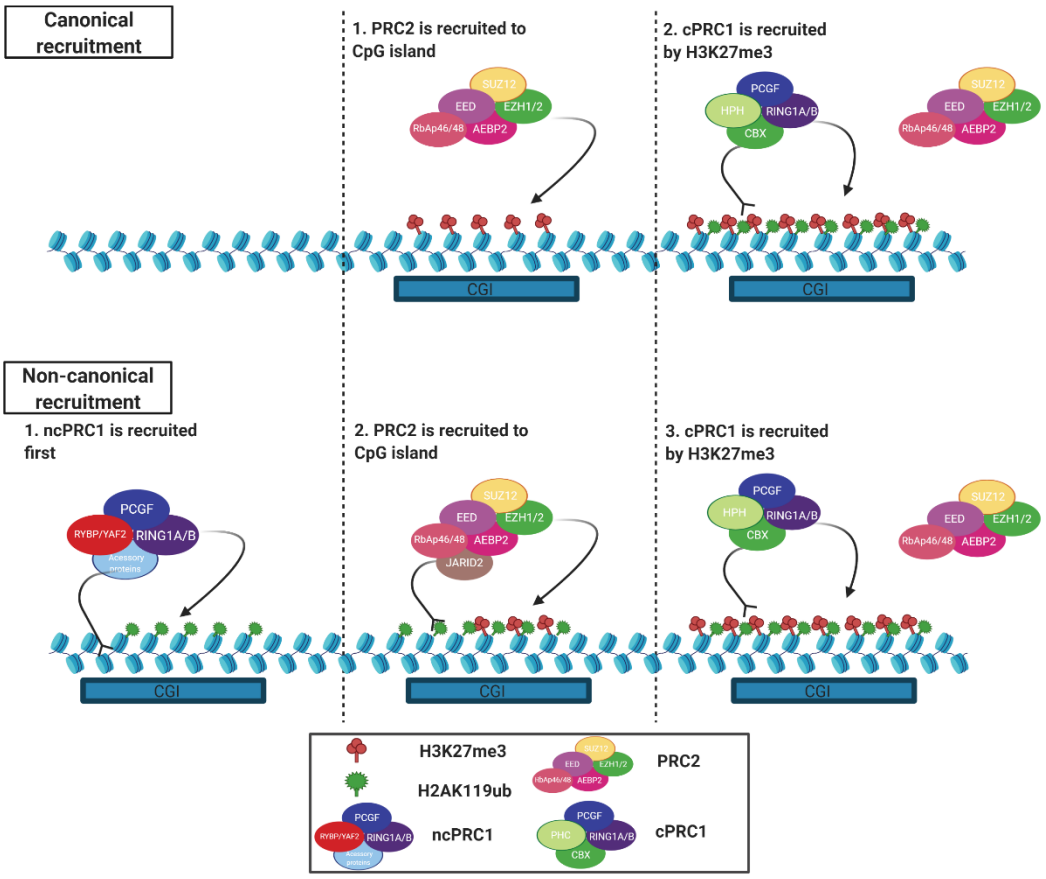

Figure 2. Illustration of the two consensus PRC1 recruitment mechanisms.

In the canonical recruitment mechanism, PRC2 mediates the tri-methylation of H3K27 which then recruits cPRC1 complexes through CBX binding. In the non-canonical recruitment mechanism, ncPRC1, through DNA binding abilities of various accessory proteins, is recruited to specific targets first. H2AK119ub deposited by ncPRC1 then recruits PRC2.2 which subsequently mediates the deposition of H3K27me3. Finally, cPRC1 is recruited by

H3K27me3 to these sites and mediates further H2AK119ub deposition and gene silencing events. *Created using BioRender.com*

1.7 Histone marks and the H3-K27M mutation

Pediatric diffuse intrinsic pontine gliomas, now recognized as an independent molecular high-grade glioma entity in the 2016 WHO classification, harbor the most frequent oncohistone, H3-K27M, and comprise almost a third of pediatric high-grade glioma cases (12, 17). This somatic heterozygote lysine-to-methionine substitution is found in all tumor cells upon tumor diagnosis, spread and autopsy (12). As specified earlier, this mutation can occur in both canonical (H3.1 or H3.2) and non-canonical (H3.3) histone variants and has a limited contribution (3-17%) to the total H3 pool (12). Nevertheless, this somatic heterozygote mutation shows a dominant impact on reducing the overall levels of the repressive H3K27me3 mark in tumor cells (12). In vitro analyses show that H3-K27M mutations drastically affect the catalytic activity of EZH2 (catalytic core of PRC2) (12). However, the precise mechanism through which reduced H3K27me3 drives neoplasm formation and progression was subject to fervent discussions (12). The ambiguity surrounding the precise cell of origin of DIPGs as well as the need to introduce the H3-K27M mutation in specific neurodevelopmental windows has highlighted the need for isogenic and tumor-specific studies (12). To tackle this question, our group used human primary pediatric high-grade glioma cell lines where the H3-K27M mutation was either already present, manually overexpressed or edited out by CRISPR techniques (12). Using mass spectrometry of these cell lines, H3K27me3 levels were significantly reduced in H3-K27M contexts when compared with isogenic H3-K27M knock-out cell lines (12, 13). Less drastically, H3K27me2 (a lower repressive state mediated by PRC2) also show reduction in H3-K27M cell lines whereas H3K27me1 demonstrates a moderate increase (12).

The observation that H3-K27M severely affects the trimethylated mark falls in line with the catalytic preference of PRC2 for lower methylated states (H3K27me0 and H3K27me1) over H3K27me2 (10, 12). Using chromatin-immunoprecipitation followed by high-throughput sequencing (ChIP-seq), the widespread domains of H3K27me3 in histone wild-type HGG cell lines were in contrast with their remarkably restricted pattern in H3-K27M cell lines (12). These broad domains were substituted for H3K27me3 localized peaks reminiscent of embryonic stem cells (12). Meanwhile, H3K27me2 was found to occupy widespread regions and to resemble H3K27me3 distribution in wild-type HGG cell lines (12). By epigenetic mapping of SUZ12, a core component of PRC2, it was observed that H3K27me3 deposition in H3-K27M HGGs was restricted to PRC2 binding sites (12). The complete overlap of H3K27me3 with SUZ12 in H3-K27M HGGs was striking when compared with wild-type HGGs where H3K27me3 could be found outside of SUZ12 occupancy (12). Most importantly, the deposition of H3K27me3 seemed to be confined to unmethylated CpG islands, whereas its spread outside of these regions was prevented by the H3-K27M mutation (12). Consequently, a shift in H3K27me3 enrichment from intergenic to promoter sites was noted in H3-K27M HGGs (12). Both these observations were replicated in HEK293T, an unrelated and differentiated cell line, where H3.3K27M was overexpressed, thus providing support for the role of H3-K27M in restricting the spread of H3K27me3 (12). Of importance, H3-K27M mutation was found not to sequester PRC2 complexes around CGIs as HGGs harboring this mutation still showed spread of H3K27me2 outside of these regions (12). Overall, it was argued that H3-K27M did not prevent the spread of PRC2 beyond its binding sites, but rather restricted its ability to catalyze H3K27me3 into widespread domains (12).

Most notably, the change of repressive H3K27me3 spread was not associated with extensive transcriptomic changes (12). Relative to H3K27me3 global reduction, only a few genes were found

to be differentially expressed, with an enrichment for upregulation of lowly-expressed genes (12). De-repression of promoters by the H3K27me3 loss of spread led to the aberrant activation of only a subset of genes with neurodevelopmental signatures (12). Nonetheless, H3K27me3 de-repression is suspected to increase transcriptional background, which might sensitize cells to oncogenic events (10, 12). Of relevance to H3-K27M HGGs, *ID1-ID4* genes were found to be upregulated upon loss of H3K27me3 spread (12). These inhibitors of DNA binding/differentiation genes (*ID*) are believed to be implicated in developmental events, maintenance of self-renewal, multipotency and, as their name suggests, inhibition of differentiation (12).

In addition, H3-K27M mutation has been reported to be associated with a global increase in an active histone mark: acetylation of H3K27 (H3K27ac) (13). To further confirm this observation, our team used mass spectrometry on H3-K27M, isogenic H3-K27M-KO and wild-type HGG cell lines and observed the significant increase of H3K27ac levels on both canonical (H3.1, H3.2) and non-canonical (H3.3) histone 3 proteins (13). Despite the global increase in H3K27ac levels, both H3-K27M and wild-type HGGs still showed a comparable number of active enhancers (regions beyond ± 2.5Kb of transcription start sites) and promoters (regions within ± 2.5Kb of transcription start sites) (13). Direct comparison between H3-K27M pHGG and isogenic H3-K27M KO of two cell lines shows that the increase in H3K27ac, as is the case for the decrease in H3K27me3 mentioned above, is largely reversible upon removal of the mutation (13). Surprisingly, very little amount of H3K27ac sites (less than 0.25%) were consistently lost in both H3-K27M KO cell lines, while the overwhelming majority remained unvarying (13). This observation was further recapitulated at the individual cell line level which hints at the possibility that H3K27ac deposition might be better associated with different cell states (13). Using Assay for Transposase-Accessible Chromatin using sequencing (ATAC-seq) on H3-K27M and wild-type HGGs and cell lines, it was

observed that H3K27ac deposition and open chromatin showed reduced correlation in H3-K27M contexts when compared with histone wild-type lines (13). This suggests open chromatin access outside of H3K27ac regions in H3-K27M HGGs and further supports the possibility that H3-K27M mutations do not significantly alter the enhancer landscape (13). Therefore, H3K27ac patterns may be more indicative of the state of the cell of origin rather than the H3-K27M mutation (13).

Most importantly, the increase in H3K27ac levels in intergenic spaces was found to increase the transcription of repeat elements (LINEs, SINEs, LTRs, transposons and others) whose repression is normally needed to maintain genomic integrity (13). Specifically, H3-K27M HGGs cell lines showed increased expression of unique families of repeat sequences, endogenous retroviruses (ERVs), known to be involved in cancer (13). Therefore, the increased H3K27ac deposition throughout the genome was associated with aberrant transcription of normally silenced regions (13). These transcriptomic events then provided a therapeutic platform that gave H3-K27M HGGs cell lines more sensitivity to histone deacetylase inhibitors and DNA demethylating agents (13). ERVs, usually silenced through DNA methylation, were then observed to be further transcribed in H3-K27M pHGG cell lines treated with panobinostat (HDACi) and 5-azacytidine (DNA demethylating agent) (13). Increased repeat element transcription is known to activate innate immune (13). Through the formation of double-stranded RNA, repeat elements induce the interferon type 1 signaling which could provide an avenue for the immune infiltrate usually present in HGGs to recognize (13). In confirmation, HGG xenograft mice showed extended survival when H3-K27M injected cell lines were treated with the mentioned drug cocktail as compared with wild-type lines and DMSO controls (13).

Overall, H3-K27M pHGGs were found to be associated with characteristic epigenetic changes that affect the repressive H3K27me3 deposition spread beyond CGIs and the increased abundance of active H3K27ac histone marks (12, 13). These two epigenetic alterations drove changes in gene expression and elevated transcription of repeat elements which then contributes to tumorigenesis (12, 13).

Chapter 2: Rationale and Hypothesis

2.1 Rationale and Hypothesis

While several recruiting mechanisms have been suggested as highlighted above, the general consensus remains that a subset of PRC1, known as canonical PRC1, recognizes the H3K27me3 mark deposited by PRC2 through CBX proteins (**Figure 1**). PRC1 has been shown to be mediate its gene regulatory role through the deposition of a single ubiquitin molecule on lysine residue 119 of the histone protein H2A (H2AK119ub) as well as formation of long-range chromatin contacts (38). While several groups have debated the importance of H2AK119ub on gene repression, recent studies demonstrate its contribution to repression and to recruitment of PRC2 ("non-canonical recruitment") (28, 38). Given the global reduction of the H3K27me3 observed in pediatric HGGs harboring the H3-K27M mutation, it is compelling to characterize its implications on PRC1 recruitment, catalytic activity and interplay with PRC2.

We hypothesize that PRC1 is redistributed in H3-K27M HGGs and is contributing to tumorigenesis.

H3K27me3 reduced spread may lead to changes in PRC1 recruitment, which then drive de-regulation of gene expression patterns through differential H2AK119ub deposition and/or chromatin reconfiguration. In order to study the role of PRC1, we subdivided our approach into 3 sequential objectives that fall under a single general aim:

Aim: Profile and characterize the role of the Polycomb Repressive Complex 1 in the context of H3-K27M pediatric high-grade gliomas.

- **Objective 1:** Characterize the distribution of core component RING1B and Histone 2A Lysine 119 monoubiquitinylation mark deposited by PRC1 in H3-K27M, H3-K27M KO and histone 3 wild type pHGG cell lines
- **Objective 2:** Compare and assess the overlap between PRC1, PRC2 and their corresponding histone modifications in H3-K27M and isogenic H3-K27M KO pHGG cell lines.
- **Objective 3:** Characterize PRC1 redistribution and its association with changes in transcriptional and/or chromatin conformation profiles in contribution to tumorigenesis.

While the overarching aim is broad and predominantly exploratory, preliminary results will help us guide research focus towards answer arising questions that fit the current lines of understanding in the field.

2.2 Limitations

Characterizing the epigenetic alterations occurring in H3-K27M pHGGs is greatly limited by the large heterogeneity (variations in age, brain location of origin, differentiation state….) that exists among different primary tumors. While using pHGGs cell lines (of different spatiotemporal origins) grouped by the presence or absence of the H3-K27M mutation strengthens the mutation association of replicated findings, it still prevents a more precise understanding of tumorigenesis throughout different neurodevelopmental windows. Certainly, the use of 2D cell cultures is intrinsically associated with its own limitations; yet, it still provides us with enough biological material to perform diverse epigenetic studies.

Table 2.Table of cell line models

Cell Line	System	Histone 3 status	Location
pcGBM2	Pediatric high-grade glioma	Wild-type	Cortex
G477	Pediatric high-grade glioma	Wild-type	Cortex
DIPGXIII	Diffuse intrinsic pontine glioma	H3.3-K27M	Pons
BT245	Pediatric high-grade glioma	H3.3-K27M	Thalamus
HSJ-019	Pediatric high-grade glioma	H3.3-K27M	Thalamus
HSJ-051	Pediatric high-grade glioma	H3.3-K27M	check
DIPGXIII isogenic knock-out	Diffuse intrinsic pontine glioma	Wild-type	Pons
BT245 isogenic knock-out	Pediatric high-grade glioma	Wild-type	Thalamus
HSJ19 isogenic knock-out	Pediatric high-grade glioma	Wild-type	Pons
G477 OE H3.3K27M	Pediatric high-grade glioma	H3.3-K27M	Cortex
G477 OE H3.3K27R	Pediatric high-grade glioma	H3.3-K27R	Cortex
HEK293T	Human embryonic kidney cells	Wild-type	Kidney
HEK293T H3.1K27M	Human embryonic kidney cells	H3.1-K27M	Kidney

Chapter 3: Materials and Methods

3.1 Cell culture

Patient-derived tumor cell lines were grown and maintained in Human Neurocult NS-A proliferation kit (StemCell Technologies) which was supplemented with bEGF (20ng/mL, StemCell Technologies), bFGF (10ng/mL, StemCell Technologies) and Heparin (0.0002%, StemCell Technologies). Culture plates were coated with poly-L-ornithine (0.01%, Sigma) and laminin (0.01mg/mL, Sigma).

HEK293T (ATCC) cells were cultured in Dulbecco's Modified Eagle's Medium high glucose (DMEM, Wisent) supplemented with heat-inactivated Fetal Bovine Serum (10%, Wisent).

All cell lines tested negative for bacteria and/or mycoplasma and were routinely tested using LB agar plates and MycoAlert Mycoplasma detection kit (Lonza). Similarly, tumor-derived cell lines matched their original samples by Short Tandem Repeat (STR) fingerprinting.

Cell cultures were maintained by the MSc candidate, Elias Jabbour.

3.2 Western Blotting

Cells were lysed for 1 hour using RIPA buffer (homemade) supplemented with cOmplete, mini, EDTA-free proteinase inhibitor cocktail tablets (Roche). Histone lysates were extracted using Histone Extraction kit (Abcam, ab113476). Protein amounts were quantified using Pierce^{TM} BCA Assay Kit (ThermoFisher Scientific). Thirty micrograms of whole cell lysates (1 microgram for histone lysates) were separated on 10% Mini-PROTEAN TGX Stain-Free Precast Gels (Bio-Rad) and transferred onto PVDF membranes (GE Healthcare) within one

hour. Blocking was then performed using 5% skim milk or 5% Bovine Serum Albumin (BSA, Wisent) in Tris-buffered saline (50mM Tris, 150mM NaCl, pH 7.4, 0.1% Tween 20) (TBST) for one hour at room temperature. Membranes were incubated in the presence of the relevant antibody overnight at 4 degrees in 5% milk or 5% BSA in 0.2% TBST: Anti-H2AK119ub (1:2000, Cell Signaling Technology D27C4), anti-total H3 (1:5000, Abcam 1791), anti-RING1B (1:1000, Active Motif 39663), anti-beta-tubulin (1:5000, CST 2146S). Membranes were washed three times with 0.2% TBST prior to incubation with Horse Radish Peroxidase-linked secondary antibodies in 3% milk/BSA for one hour at room temperature: anti-mouse (1:10000, Novus NB7539) or anti-rabbit (1:10000, Bethyl A120-100P). Membranes underwent a final three-rounds of washes with 0.2% TBST before the signal was developed with Amersham ECL Prime Western Blotting Detection Reagent (GE Healthcare). Finally, signals were visualized using ChemiDoc MP Imaging System (Bio-Rad).

Western blots were performed by the MSc candidate, Elias Jabbour.

3.3 CRISPR/Cas9 genome editing and knock-out

CRISPR-Cas9 editing was performed as suggested in Ran et al. (55). Constructed were home-designed and transfected using lipofectamine 2000 (ThermoFisher Scientific) as per the manufacturer's protocol (12, 13). Clones were expanded after flow-cytometry sorting of GFP-positive cells into 96-well plates, 3 days after transfection. Target loci were genotyped on agarose gels and screened by Sanger sequencing. Clones showing initial genomic alterations were then sequenced by Illumina MiSeq to further confirm target mutations. Protein validations were also carried out by western blotting, mass spectrometry and/or immunofluorescent staining as in Harutyunyan et al. (12).

In HEK293T cells with H3.1K27M mutations, clones heterozygous for the HIST1H3B-K27M mutation were generated through the use of pSpCas9(BB)-2A-GFP (PX458) guide sequence and repair templates (gift from Feng Zhang, Addgene plasmid #48138) (12, 13).

CRISPR/cas9-edited cell lines were generated by Harutyunyan et al. (12). Cell lines were grown and maintained by the MSc Candidate, Elias Jabbour for RING1B, CBX2 and H2AK119ub experiments.

3.4 Chromatin Immunoprecipitation followed by high-throughput sequencing (ChIP-seq)

As in Harutyunyan et al. (12), tumor-derived cell lines were fixed with formaldehyde (1%, Sigma) for 10 minutes. Cross-linking was stopped by the addition of glycine (125mM). Fixed cells were then washed, pelleted and preserved at -80 °C. Chromatin was then lysed using BioRupter UCD-300 using a 1%SDS-containing buffer. A total of 60 cycles of sonication (10s ON, 20s OFF at 4°C) was performed, including resuspension every 15 cycles. Chromatin quality of samples was then assessed by gel electrophoresis and checked for the 150-500bp bands. Upon adequate sonication, SDS was diluted to 0.1% in samples for optimal ChIP reactions. For internal calibration, 2% of sonicated drosophila S2 chromatin was added to each sample that allowed for histone level quantification after sequencing.

Chromatin IP reactions for all histone marks were performed using the Diagenode SX-8G IP-Star compact Diagenode automated iDeal ChIP-seq machine and kit. Protein A beads (25uL/IP, Invitrogen) were washed with RIPA lysis buffer and incubated with antibodies at the corresponding concentrations: anti-H3K27me3 (1:100, Active Motif 61017), anti-H3K27me2 (1:50, CST 9728), anti-H3K36me2 (1:50, CST 2901), anti-H3K27ac (1:80, Diagenode

C15410196), anti-H3K4me3 (1:66, CST 9751), anti-H3K4me1 (1:100 ,CST 5326), anti-H2AK119ub (1:50, CST D27C4). An equivalent of chromatin from 2 million sonicated cell lysate were used for each IP along with protease inhibitors. The total reaction time was of 10h, followed by 20 min wash cycles and elution using iDeal ChIP-seq kit for histones.

Chromatin IP reactions for CBX2, RING1B and SUZ12 were performed manually as described below:

An equivalent of chromatin from 5 million sonicated cell lysate were incubated in the presence of 40uL of antibody-conjugated protein A or G beads at 4°C overnight. Conjugation of the antibodies took place on rotating platform for a minimum of 6 hours at 4°C by the addition of the following antibody amounts: anti-CBX2 (1:200 ,Bethyl A302-524A), anti-RING1B (1:200, Active Motif 39663), anti-SUZ12 (1:150, CST 3737). After IP reaction, beads were washed using buffers from the iDeal ChIP-seq kit (RIPA, RIPA + 500mM NaCl, LiCl, TE) and eluted for 30 min at room temperature.

Reverse cross-linking of chromatin was performed at 65°C for 4 hours prior to treatment with RNase Cocktail (1:60, Invitrogen) for 30 min followed by Proteinase K (1:60, Invitrogen) for 30 min. DNA was purified using the QIAGEN MiniElute PCR purification kit using the manufacturer's protocol. Input samples (50,000 cells) were reverse crosslinked in parallel and were followed by the same purification steps.

DNA libraries were prepared using KAPA HyperPrep Illumina library preparation reagents (Roche). 50uL of dilute ChIP samples were incubated with 10uL of End Repair and A-tailing mix for 30 min at 20°C then for 30 min at 65°C. Adaptor ligation was performed using IDT for Illumina Truseq UD Indexes (Illumina) in the presence of ligation buffer and enzymes at 20°C

for 15 min. Ligated samples then underwent an Ampure XP Beads purification step prior to library amplification by 10-12 cycles of PCR. Enriched libraries finally underwent size selection using a 0.625x/0.825x ratio of Ampure XP beads for optimal collection of 250-500bp fragments.

Libraries generated in this study were sequenced using Illumina NovaSeq 6000 System at 100 bp paired-end reads. ChIP-seq quality comparison can be found in the appendix.

ChIP-seq experiments for SUZ12, H3K27me1, H3K27me2, H3K27me3, H3K4me1, H3K4me3, H3K27ac, H3K36me2 were performed by members of the Dr. Nada Jabado Lab as in Harutyunyan et al. (12) and Krug et al. (13).

ChIP-seq optimization and experiments for RING1B, CBX2 and H2AK119ub were performed by the MSc candidate, Elias Jabbour.

3.5 RNA sequencing

RNA was extracted from cell pellets using QIAGEN RNA extraction kit following the manufacturer's protocol. Libraries were prepared with ribosomal RNA (rRNA) depletion following Epicentre instructions to enrich for mRNA and long non-coding transcripts. Paired-end sequencing of 100 bp reads was performed using the Illumina HiSeq 2500 or 4000 platforms.

RNA-seq experiments for H3-K27M and isogenic H3-K27M KO pHGG cell lines were performed by members of the Dr. Nada Jabado Lab as in Harutyunyan et al. (12) and Krug et al. (13).

3.6 Analysis of Chromatin immunoprecipitation sequencing (ChIP-seq) data

Raw sequencing reads were aligned to human (UCSC hg19) and drosophila (UCSC dm6) genome builds using BWA (56) V0.7.17 with default parameters. RNA-seq differential

expression analysis was performed using “DESeq2” in SeqMonk (https://www.bioinformatics.babraham.ac.uk/projects/seqmonk/) v1.4.54.

We divided the human genome into either 5Kb or 10Kb bins and counted the number of reads from both ChIP-seq and input samples at those bins. Reads were counted at CpG islands (CGIs) and other defined regions using R (112). Promoters were defined as ±2.5 Kb region centered on TSS. ChIP-seq enrichment for correlation heatmaps was generated using ChIP reads normalized to sequencing depth (RPKM) and input.

The annotation of CGIs, TSS and RefSeq transcripts for hg19 were obtained from the UCSC Table Browser.

Analyses of all ChIP-seq data used in this study were performed by the MSc candidate, Elias Jabbour.

3.7 Peak Calling

To call peaks, we used MACS2 (59) peakcaller in SeqMonk with parameters set to default. We then optimized MACS2 peaks by preserving peaks that passed empirical parameters of enrichment over input and enrichment over sequencing depth. A comparable fold of peaks was obtained per cell line.

Optimized peak-calling was performed by the MSc Candidate, Elias Jabbour.

3.8 Clustering and Heatmap

PRC1 RING1B peak coordinates were extracted from the hg19 version of the human genome. Average ChIP-seq enrichments of H2AK119ub, SUZ12, H3K27me3, H3K27me2,

H3K27me1, H3K27ac, H3K36me2, H3K4me3 and H3K4me1 signals were plotted and calculated using ChAsE v1.1.12 (57) over clusters stratified using k-means (k=6) function in R.

Clustering and heatmap plotting were performed by the MSc Candidate, Elias Jabbour.

3.9 R coding and pipelines

All custom-made R codes and pipelines used in generated figures and analyzing data were uploaded on the following repository: https://github.com/egj1997/Correlation-Plots-.git

R codes and pipelines were designed by the MSc Candidate, Elias Jabbour.

Chapter 4: Results

To characterize and map the distribution of PRC1 and its role in the context of pediatric high-grade gliomas, we used patient-derived pediatric tumor high-grade glioma cell lines harboring the H3-K27M somatic mutation. Two cell lines: BT245 and DIPGXIII were selected due to the abundant availability of sequencing data from previous studies performed by our research group (ChIP-seq, RNA-seq and Hi-C) (12, 13). Moreover, the aforementioned cell lines were previously used to generate isogenic histone wild-type conditions whereby the allele coding for the K27M mutant histone 3.3 variant was knocked-out by CRISPR/Cas9 editing. It is important to mention that these knock-out cell lines, referred to as isogenic H3-K27M KO from this point onward, maintained comparable levels of total H3 proteins including non-canonical H3.3 as their parental counterparts, thus providing a suitable isogenic match to investigate the role of the H3-K27M mutation in pediatric high-grade gliomas (12, 13).

To map PRC1 distribution in H3-K27M pHGG cell lines, we performed chromatin-immunoprecipitation followed by high throughput sequencing (111) on components of PRC1. We chose the catalytic factor and core component, RING1B, due to its well-documented incorporation in all PRC1 complexes (10). Similarly, we performed ChIP-seq on the histone modification catalyzed by PRC1: H2AK119ub. To distinguish canonical PRC1 complexes, we also performed ChIP-seq on CBX2, one of the CBX proteins known to recruit PRC1 to H3K27me3 sites (10). Our choice of CBX2 was based predominantly on the reported efficacy of the antibody for sensitive ChIP-seq experiments (87). Nonetheless, it should be noted that other CBX proteins can be incorporated to PRC1 complexes and define these canonical subsets (28). A full panel of PRC1 components and their expression levels in our cell line models is found in the appendix (**Figure 33**).

4.1 H3-K27M pHGGs shows no significant changes in global H2AK119ub levels

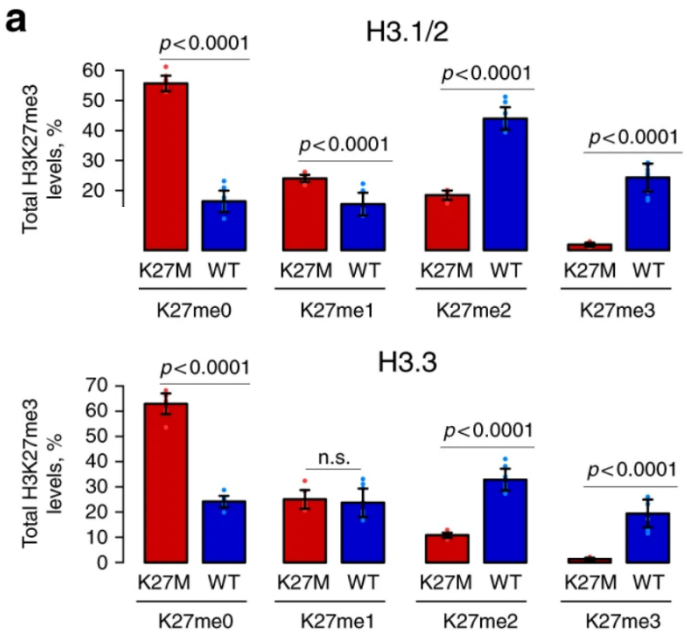

Figure 3. Mass Spectrometry quantification of H3K27me0/1/2/3 levels in H3-K27M and WT pHGG cell lines. *Mean and standard deviation of three replicates for each cell lines are reported. Student's t-test was performed.

Mass spectrometry quantification of H3K27 methylation states in 3 H3-K27M (red) and 3 histone wild-type pHGG (blue) cell lines. Results a significant decrease of H3K27me2 and 3K27me3 on histone variants H3.1/2 and H3.3 in H3-K27M conditions. No significant changes were seen for H3K27me1 at H3.3 histones, but a significant elevation of this modification was seen in H3.1/2 variants in H3-K27M pHGG cell lines. We also observe a significant increase in H3K27me0 abundance on histone variants H3.1/2 and H3.3 in H3-K27M conditions.

As mentioned above, pHGGs show consistent global reduction of the repressive H3K27me2/3 marks (**Figure 3**). These marks are known to recruit at least a subset of PRC1

complexes, known as canonical PRC1, through the binding of chromodomain proteins (CBXs) (87).

As a result, it was compelling to assess the levels of H2AK119ub deposited by PRC1 and compare its abundance in H3-K27M and isogenic H3-K27M KO pHGG cell lines. To do so, we performed western blot analysis on H2AK119ub levels in BT245 (H3-K27M, red), DIPGXII (H3-K27M, red) as well as isogenic H3-K27M KO clones (blue) for each of these pHGG cell lines (**Figure 4**).

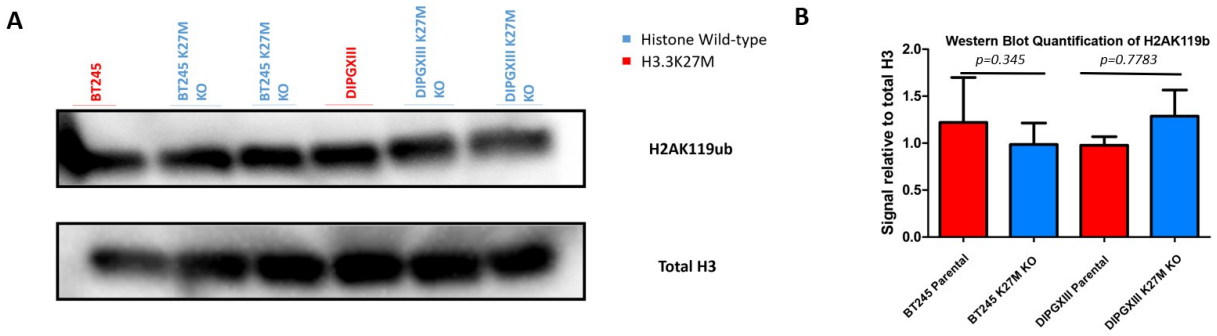

Figure 4. H2AK119ub protein level comparison between H3-K27M and isogenic H3-K27M KO pHGG cell lines

(A) Western Blot comparing the levels of H2AK119ub in H3-K27M and isogenic H3-K27M KO pHGG cell lines. (B) Western Blot Quantification of H2AK119ub of three replicates for each cell line. Mean and standard deviations are plotted and Student's t-test was performed. Protein comparison of H2AK119ub in H3-K27M and H3-K27M KO pHGG cell lines show no significant changes in levels across conditions. Three biological replicates for each condition and cell line were used and showed, consistently, no significant changes in H2AK119ub across histone conditions (p-values=0.345 in BT245, p-value=0.7783 in DIPGXIII).

Quantification of western blots showed no significant changes in overall H2AK119ub levels between H3-K27M and H3-K27M KO pHGG conditions (**Figure 4**). This is in contrast with the large reduction of H3K27me3 levels observed in H3-K27M conditions (**Figure 3**) (12). These results were further confirmed by ChIP-seq Rx quantifications where equal amounts of Drosophila S2 chromatin present in each ChIP-seq reaction allowed for internal calibration and

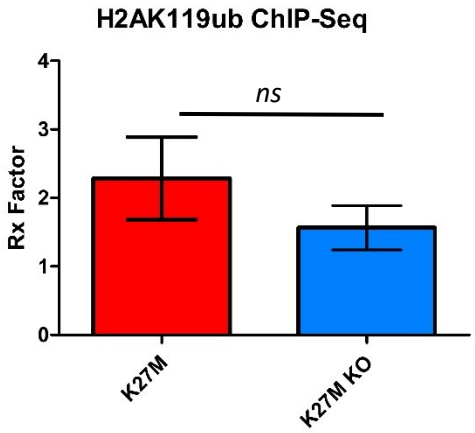

Figure 5. ChIP-Rx scores comparision of H2AK119ub ChIP-seq experiments in H3-K27M and isogenic H3-K27M KO pHGG cell lines.

*Mean and standard deviations are plotted, and Student's t-test was performed.

ChIP-seq Rx scores were used to compare H2AK119ub abundance in H3-K27M (n=3) and H3-K27M KO (n=3) pHGG cell lines. Rx scores are generated using an internal calibration system of equal amounts of Drosophila S2 chromatin spike in. Normalizing to Rx scores show no significant changes of H2AK119ub abundance across histone conditions (p-value=0.6893).

rendered histone mark quantification more precise (12). By normalizing ChIP-seq enrichment to the exogenous reference system, we similarly show that H2AK119ub deposition levels display no significant differences across pHGG conditions (p-value=0.6893) (**Figure 5**).

4.2 H3-K27M mutation does not significantly perturb H2AK119ub deposition

We next investigated the deposition of H2AK119ub across the genome. Consistent with previous reports (28, 62), H2AK119ub occupied extensive regions of the genome forming a cushion layer that showed higher enrichment only at specific sites. These were mostly PcG sites that showed recruitment of PRC1 (RING1B) and/or PRC2 (SUZ12). Surprisingly, despite the drastic reduction in spread of the H3K27me3 mark seen in H3-K27M pHGGs, H2AK119ub spreading seemed to be unaffected by the mutation (**Figure 6**, right box). At these sites, H2AK119ub showed slightly higher enrichment in the form of peaks in H3-K27M conditions. This pattern will be highlighted further in subsequent sections. Meanwhile, sites showing complete loss of H3K27me3 deposition in H3-K27M condition were still marked with unaltered H2AK119ub deposition (**Figure 6**, left box).

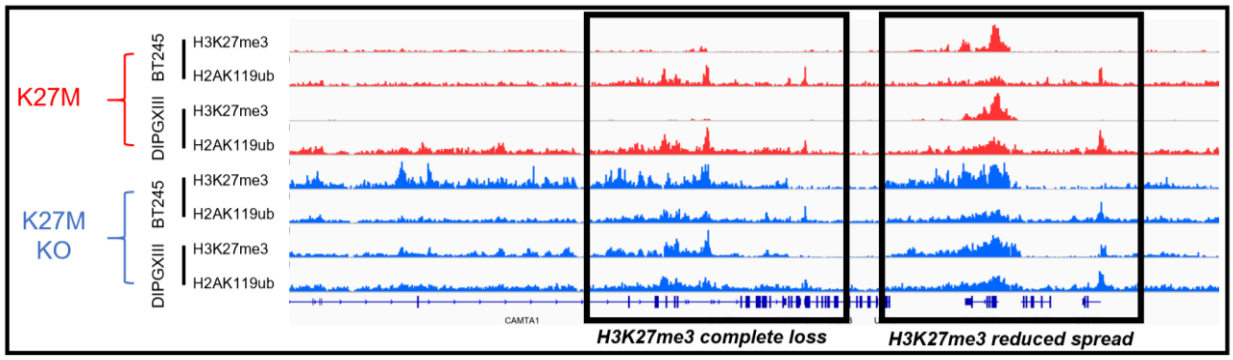

Figure 6. ChIP-seq tracks of H3K27me3 and H2AK119ub in BT245, DIPGXIII and their isogenic H3-K27M KO conditions. ChIP-seq track comparisons of H3K27me3 and H2AK119ub in BT245 and DIPGXIII parental vs H3-K27M KO conditions show maintenance of H2AK119ub deposition. The left box portrays a site where H3K27me3 deposition was completely lost in H3-K27M conditions and where H2AK119ub deposition was maintained as in H3-K27M KO conditions. The right box portrays a site where H3K27me3 was still deposited, but with a reduced spread, in H3-K27M conditions and where H2AK119ub deposition was maintained as in H3-K27M KO conditions.

Overall, it was clear that neither H2AK119ub global levels nor its deposition patterns were changing in H3-K27M pHGGs when compared with their isogenic H3-K27M KO counterparts. Stacked heatmap of H3K27me3 and H2AK119ub (Rx-normalized) ChIP-seq signals centered over CpG islands (CGIs) further confirm the drastic effects that H3-K27M has on H3K27me3 while leaving H2AK119ub largely unperturbed (**Figure 7**).

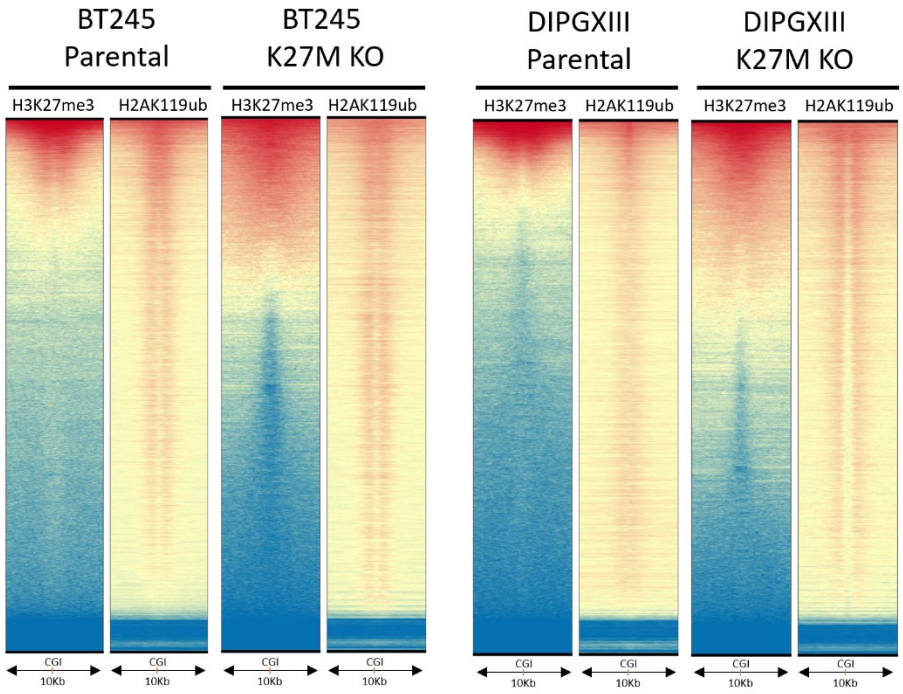

Figure 7. Stacked heatmap plots of H3K27me3 and H2AK119ub ChIP-seq signals on CGIs in BT245, DIPGXIII and their isogenic H3-K27M KO conditions.

ChIP-seq enrichment comparison shows that H3K27me3 is reduced in levels and spread around CGIs (extended to 10Kb windows) in H3-K27M conditions when compared with isogenic H3-K27M KO conditions. H2AK119ub maintains comparable spread and levels at CGIs across conditions. Levels of both H3K27me3 and H2AK119ub ChIP-seq enrichment were internally normalized to endogenous Drosophila input for better quantification.

As seen in figure 7, H3K27me3 shows reduced enrichment at CGIs in H3-K27M conditions and gains its wider spread in H3-K27M KO cell lines (**Figure 7**). This is in contrast with H2AK119ub which shows no significantly discernable changes in spread and levels at CGIs (**Figure 7**).

4.3 Overview of PRC1 loci

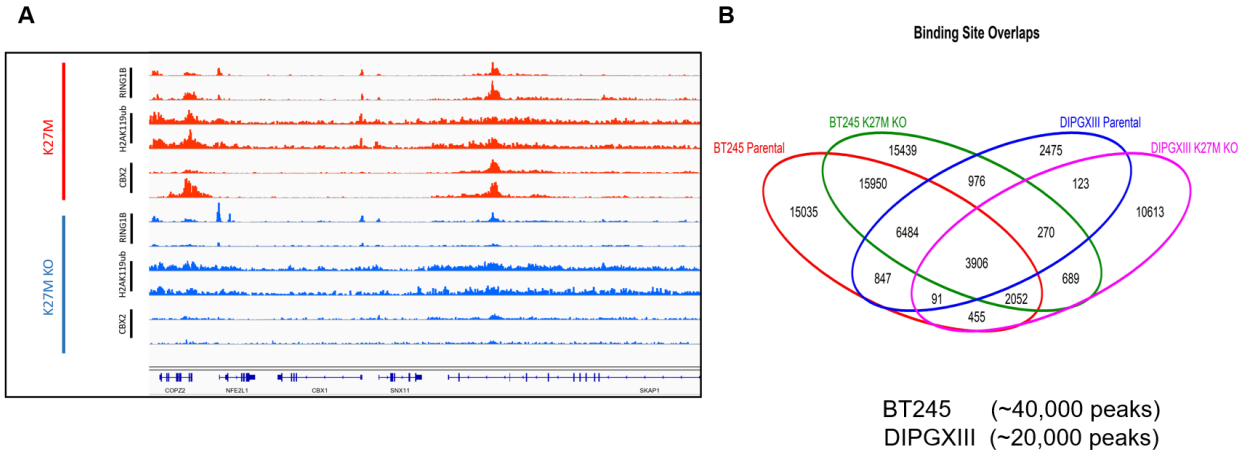

Figure 8. Overview of RING1B, CBX2 and H2AK119ub ChIP-seq patterns.

(A) ChIP-seq tracks illustrating the enrichment patterns of RING1B, CBX2 and H2AK119ub in two H3-K27M (red) and two isogenic H3-K27M KO (blue) pHGG cell lines. (B) Venn diagram showing the numbers of unique and overlapping RING1B optimized peaks called using MACS2 in BT245, DIPGXIII and their isogenic H3-K27M KO clones. RING1B and CBX2 ChIP-seq enrichments showed more localized and localized patterns of deposition when compared with the wide-spread H2AK119ub patterns. ChIP-seq RING1B peak calling yielded a comparable fold of RING1B peaks was called per cell lines, whereby BT245 parental and H3-K27M KO presented ~40,000 peaks whereas DIPGXIII parental and H3-K27M KO presented ~20,000 peaks.

ChIP-seq experiments of RING1B, CBX2 and H2AK119ub yielded different enrichment patterns, which were in line with the different biological nature of these entities (PRC complex vs histone marks). ChIP-seq of RING1B and CBX2 yielded localized foci of enrichment as seen in the peaks pattern of **Figure 8**. This is contrast with histone mark ChIP-seq tracks of H2AK119ub which demonstrate a wider and more expansive enrichment patterns. H2AK119ub, seen in **Figure 8**, blankets the genome and shows increased enrichment in regions showing PRC1 recruitment (RING1B peaks).

To map the localization of PRC1 within the genome, we used optimized peak calling of RING1B ChIP-seq signals in BT245 (H3-K27M), DIPGXIII (H3-K27M) and their isogenic H3-K27M KO conditions (**Figure 8**). A comparable fold of RING1B peaks was called for each H3-K27M pHGGs cell line when compared with its isogenic H3-K27M KO condition (BT245, ~40,000 peaks, DIPGXIII, ~20,000 peaks) (**Figure 8**). Half of these peaks were present in both the parental and H3-K27M KO condition for each cell line; however, unique peaks were also identified that were exclusive to either the H3-K27M or to the wild-type conditions. (**Figure 8**). This highlights a potential PRC1 redistribution pattern which will be described later.

4.4 Overview of RING1B and its association with other epigenetic marks

To obtain an overview of PRC1 distribution and its association with other epigenetic complexes and histone marks in our cell lines, we performed k-mean clustering on the union of the identified RING1B peaks present in BT245 parental and its isogenic H3-K27M KO condition (~60,000 peaks). This allowed us to gain global insight into PRC1-occupied regions across the genome, characterize its association with other histone marks and identify changes of pattern. We next plotted the enrichment of different histone mark and PcG component ChIP signals on 10Kb

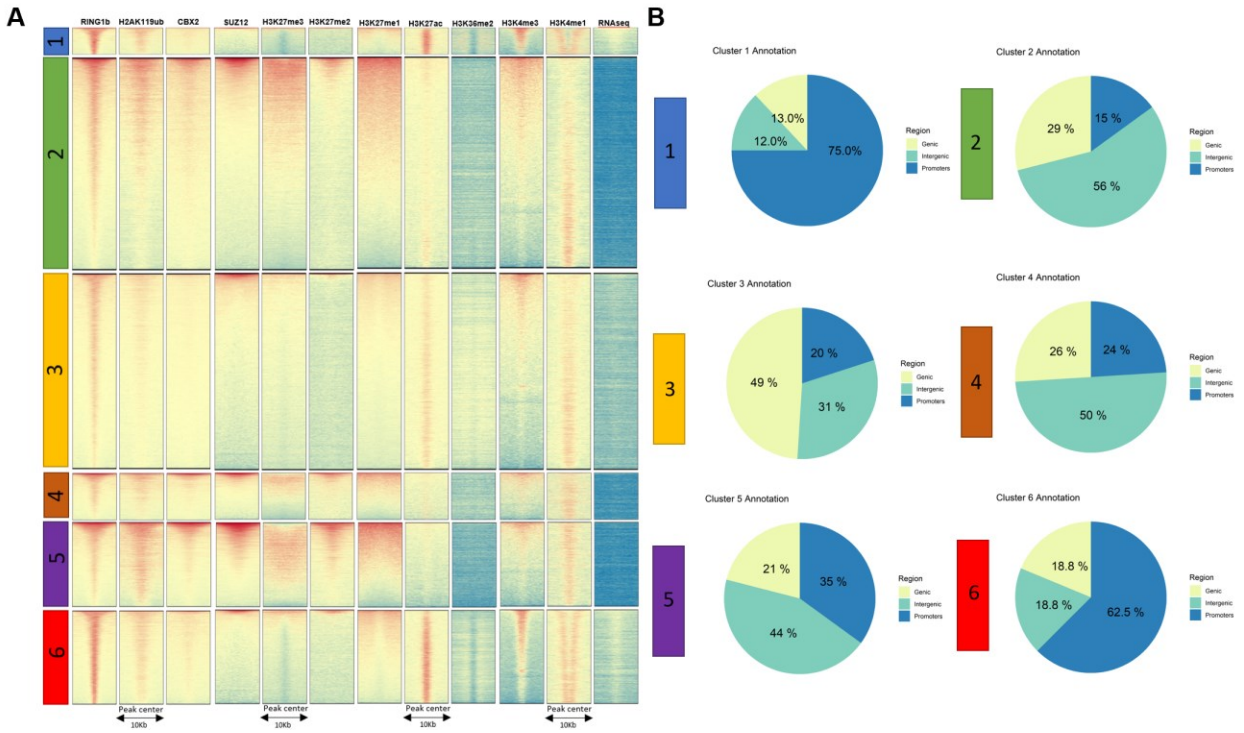

Figure 9. Stacked heatmap of 6 RING1B clusters in BT245 parental pHGG cell line.

(A) Total RING1B kmeans clustering yielded 6 clusters enriched for either H3K27me1/2/3 or H3K27ac with a combinatorial enrichment of H3K4me1/3 in BT245 parental pHGG cell line. Specifically, clusters 1, 3 and 6 are enriched for H3K27ac while clusters 2, 4 and 5 are enriched for H3K27me1/2/3.

(B) Pie chart showing the genomic annotation of each of the 6 clusters from figure 9A. Genomic annotation of RING1B clusters show different region specificities. “Promoters” are defined as regions within ±2.5Kb from TSS, “Genic” as gene bodies and “Intergenic” as regions outside of ±2.5Kb from TSS and outside of gene bodies.

windows centered around total RING1B peaks in BT245 parental cell lines (H3-K27M) (**Figure 9**). The clusters predominantly separated based on association with either H3K27ac (clusters 2, 4 and 5) or H3K27me1/2/3 (clusters 1, 3 and 6). As expected, CBX2 was enriched in clusters 1, 3 and 6 dominantly marked by H3K27me1/2/3. This latter observation is in confirmation with studies showing that CBX proteins can recognize H3K27me2, albeit with reduced affinity when compared with H3K27me3 (41). Of importance to our H3-K27M pHGGs contexts, cluster 5 shows the strongest enrichment for H3K27me3 in H3-K27M conditions (**Figure 9**).

A comparison of clusters across H3-K27M and H3-K27M KO conditions shows that cluster 5 gains enrichment of PRC1 and PRC2 components/histone marks in H3-K27M pHGG cell lines (**Figure 10**). RING1B peaks in cluster 5 show increased CBX2, H2AK119ub, SUZ12 and

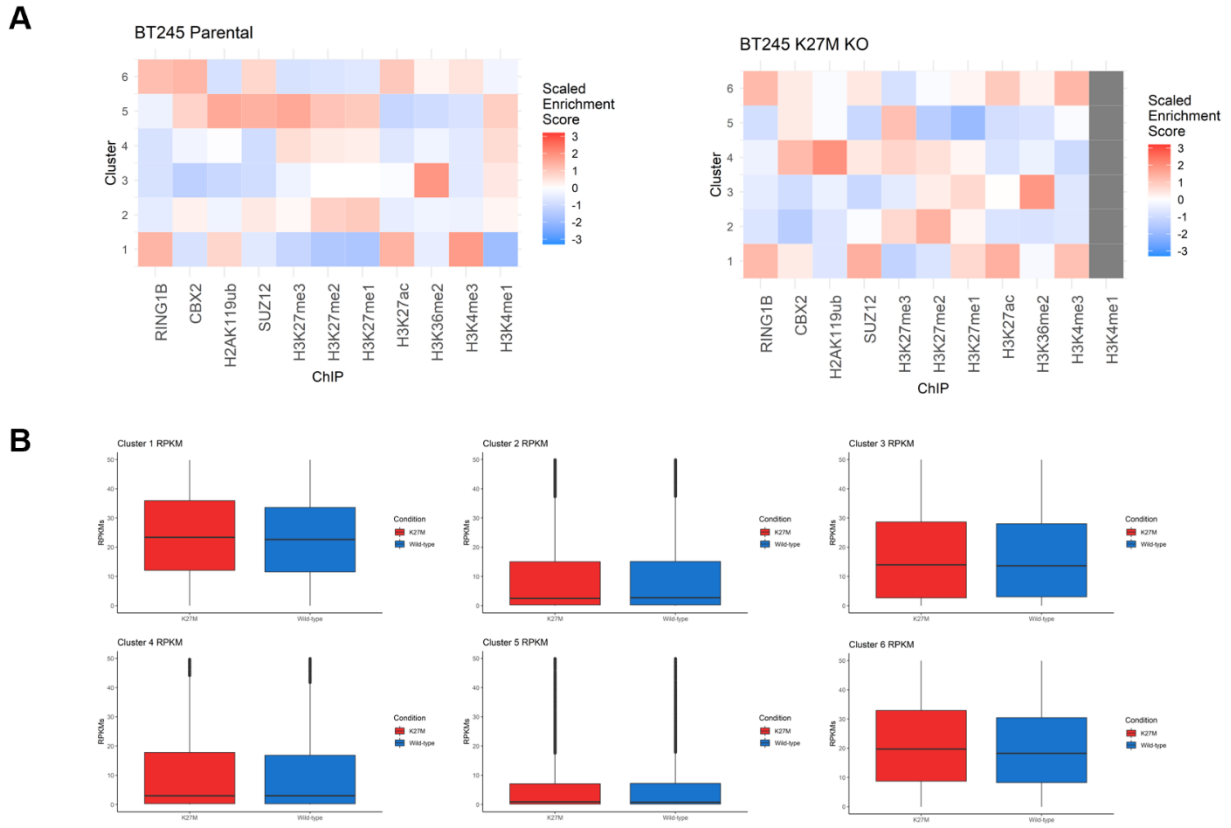

Figure 10. RING1B cluster comparison between BT245 parental and isogenic H3-K27M KO pHGG cell line.

(A) Heatmap of ChIP signal scaled enrichment scores for each of the 6 RING1B clusters in BT245 Parental cell lines and BT245 H3-K27M KO cell lines. Cluster 5 enrichment comparisons show increased enrichment for PRC1 and PRC2-related ChIP-seq signals in H3-K27M when compared with H3-K27M KO conditions. Specifically, RING1B, CBX2 and H2AK119ub gain enrichment at this site with SUZ12 and H3K27me1/2/3. (B) Boxplots comparing RPKM levels of all 6 clusters in H3-K27KM (red) and H3-K27M KO (blue) BT245 cell lines. RPKM level comparisons show different expression patterns across clusters with cluster 5 being the most repressed.

*H3K4me1 ChIP-seq data was not available for BT245 H3-K27M KO samples.

H3K27me1/2/3 enrichment in BT245 parental cell lines (H3-K27M) when compared with H3-

K27M KO conditions. This cluster corresponded to genes that were repressed or lowly expressed as seen in **Figure 10**. It should be highlighted that all clusters were centered on RING1B peaks and showed PRC1 presence, albeit to different relative extents as seen by the range of colors seen in figure 10A.

4.5 PRC1 and PRC2 show increased overlap in H3-K27M pHGGs

To unravel the potential change in association highlighted above, we narrowed down our analysis to PRC1 regions associated with H3K27me3 in BT245 and DIPGXIII (cluster 5). As shown in previous studies, H3K27me3 enrichment at CGIs was affected by the H3-K27M mutation (12), so we plotted H3K27me3, RING1B and H2AK119ub on CGIs extended to 50Kb windows. We then delved deeper on the cluster enriched for H3K27me3 and sorted the bins by H3K27me3 enrichment location. As observed in **Figure 11**, RING1B and H2AK119ub were deposited both at- (following the diagonal line) and beyond- (following the vertical line) H3K27me3 sites. It was specifically the diagonal pattern that showed an increase in enrichment for RING1B and H2AK119ub in the H3-K27M condition of both BT245 and DIPGXIII parental cell lines (**Figure 11**). When the H3-K27M mutation was removed, we show that RING1B and H2AK119ub were less deposited along the diagonal but maintained a comparable enrichment along the vertical line (**Figure 11**). We then surmised that H3K27me3 reduction in spread created strong recruitment sites for PRC1 in H3-K27M contexts. When the mutation was removed, H3K27me3 gained its spread and PRC1 was less strongly recruited to H3K27me3 regions as observed in **Figure 11**.

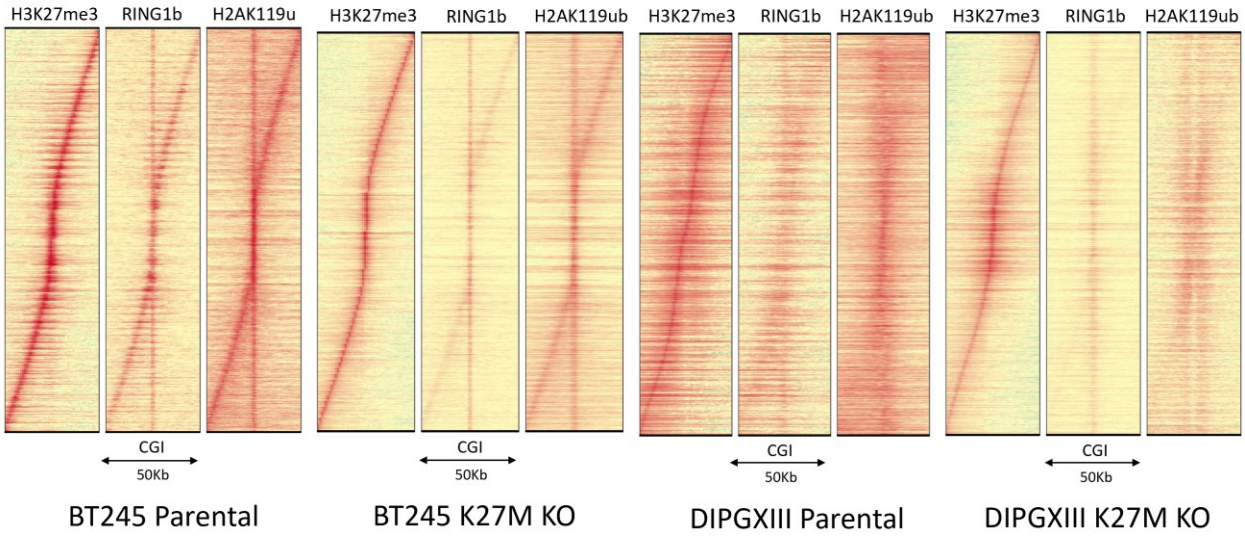

Figure 11. Heatmap of H3K27me3, RING1B and H2AK119ub ChIP-seq signal on CGIs sorted by H3K27me3 peak location.

Stacked heatmap enrichment of H3K27me3, RING1B and H2AK119ub on CGIs show that RING1B and H2AK119ub are deposited both along (diagonal) and outside (vertical) of H3K27me3. Specifically, RING1B and H2AK119ub enrichments along H3K27me3 (diagonal) are increased in H3-K27M when compared with H3-K27M KO conditions.

We also extracted one of those plotted regions, CDKN2A, and observed more concretely the increased overlap between RING1B, H3K27me3 and H2AK119ub highlighted above (**Figure 12**).

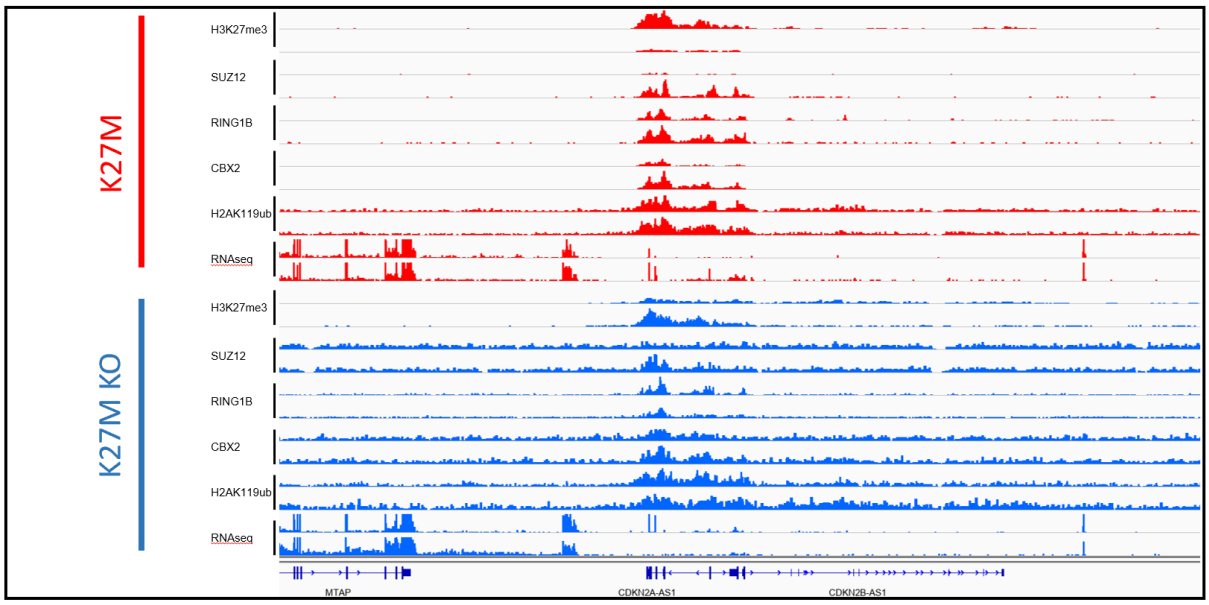

Figure 12. CDKN2A ChIP-seq and RNA-seq tracks of BT245, DIPGXIII and their isogenic H3-K27M KO conditions. ChIP-seq track comparison of CDKN2A tagged with H3K27me3 across conditions show increased overlap of PRC1 and PRC2-related enrichments in H3-K27M when compared with isogenic H3-K27M KO conditions. Specifically, it is observable that RING1B and CBX2 enrichments are elevated in H3-K27M conditions while all PRC1 and PRC2-related ChIP-seq signals are more overlapping in H3-K27M than in isogenic H3-K27M KO conditions.

As shown in the ChIP tracks (**Figure 12**), H3K27me3, SUZ12, RING1B, CBX2 and H2AK119ub showed great overlap in the H3-K27M conditions. This overlap was reduced in H3-K27M KO conditions, whereby PRC1 and PRC2 was less strongly coupled and where H3K27me3 more spread around the CDKN2A promoter. Despite the pattern observed, CDKN2A maintained similar expression levels across conditions.

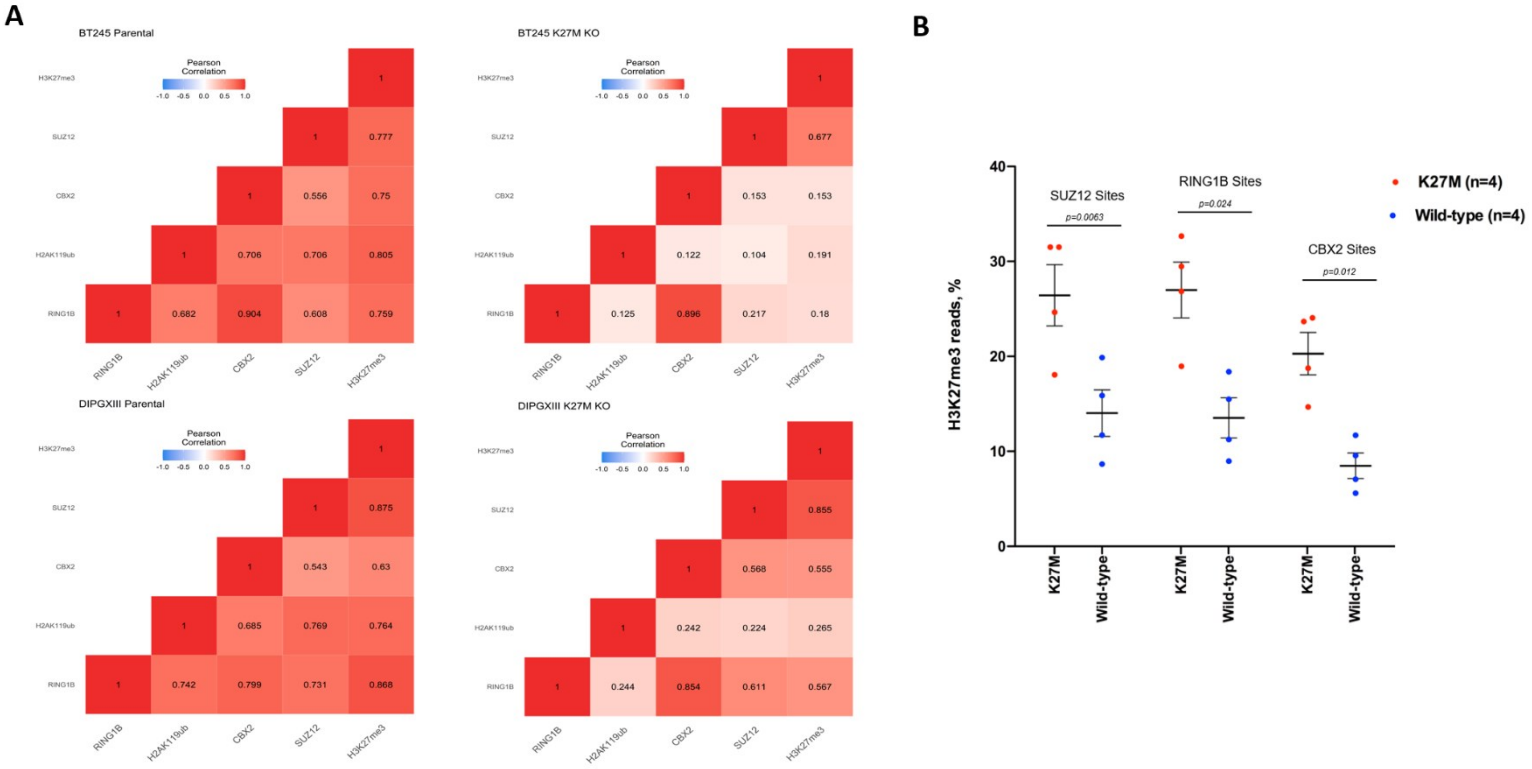

Figure 13. PRC1 and PRC2 correlation comparison between H3-K27M and isogenic H3-K27M KO pHGG cell lines at H3K27me3 regions.

(A) Correlation plot of PRC1/2-related ChIP-seq input-normalized RPKMs in BT245, DIPGXIII and their isogenic H3-K27M KO at H3K27me3 regions. Quantification of correlation scores from PRC1 and PRC2 ChIP-seq input-normalized RPKMs show increased coupling of these two complexes at H3K27me3 in H3-K27M conditions. (B) Quantification of H3K27me3 read percentage at SUZ12, RING1B and CBX2 peaks in H3-K27M (n=4) and isogenic H3-K27M KO (n=4) pHGG cell lines. Mean and standard deviations are plotted, and student's t-test was performed for each factor. H3K27me3 RPKM quantification show significant and consistent increased proportion of reads overlapping SUZ12, RING1B and CBX2 peaks in H3-K27M (n=4) when compared with H3-K27M KO (n=4) conditions.

We next attempted to quantify this increased overlap between PRC1 and PRC2, termed "increased coupling" from this point onward, in H3-K27M conditions. To do so, we computed the correlation values of RING1B, CBX2, H2AK119ub, SUZ12 and H3K27me3 ChIP-seq RPKMs normalized to input. Input-normalized RPKMs provided a more standardized method of

comparison across samples since our pHGG cell lines originated from different tumors that exhibit variant genomic aberrations, abnormalities and amplifications.

We then investigated PRC1 and PRC2 reads correlation at regions marked by H3K27me3 in both parental and H3-K27M KO conditions (**Figure 13**). We observed that PRC1, PRC2 as well as the modifications that they each catalyze where increasingly correlated in H3-K27M (left panel) conditions when compared with their H3-K27M KO counterparts (right panel). These observations were replicated in both BT245 and DIPGXIII and were strong enough (p-value<7.956e-06) to still be noticeable when we expanded our analysis to the whole genome (**Figure 14**).

In parallel, we used the approach delineated in Harutyunyan et al. (12) and quantified the proportion of H3K27me3 reads that overlapped with SUZ12, RING1B and CBX2 peaks in H3-K27M and wild-type (H3-K27M KO) conditions (**Figure 13**). We observed a consistent, and statistically significant, increase in the percentage of H3K27me3 reads that overlapped with these peaks in H3-K27M condition when compared with H3-K27M KO conditions (**Figure 13**). This further confirmed the increased coupling of PRC1 and PRC2 in H3-K27M conditions

initially observed in our cluster analysis (**Figure 10**) and then highlighted by our heatmap (**Figure 11**).

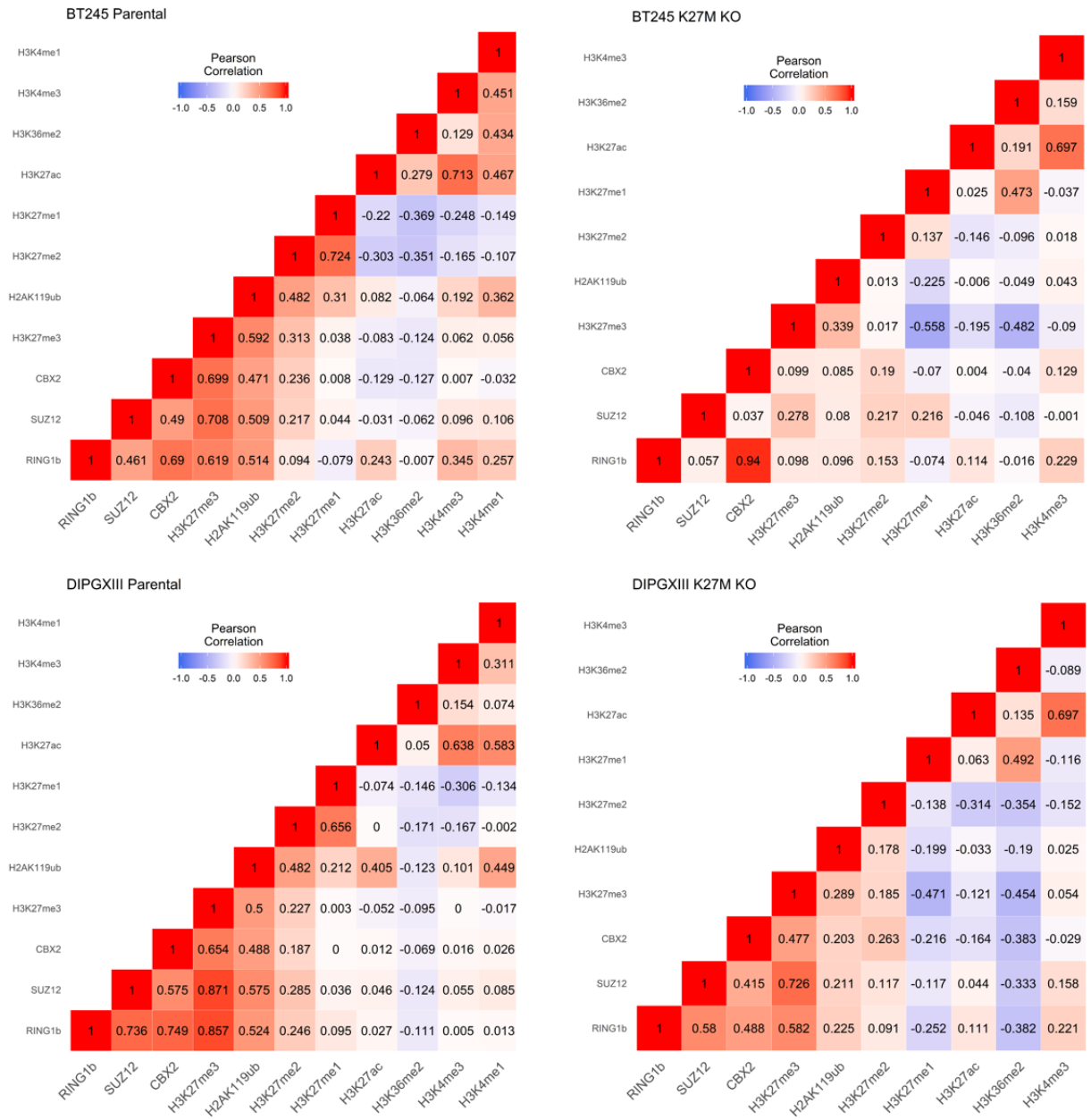

Figure 14. Correlation plots of genome-wide ChIP-seq input-normalized RPKMs in BT245, DIPGXIII and their isogenic H3-K27M KO.

Correlation comparison of input-normalized ChIP-seq RPKMs still showed increased PRC1 and PRC2 coupling in H3-K27M even at the genome level whereby RING1B, CBX2, H2AK119ub, SUZ12 and H3K27me3 showed higher correlation values together when compared with isogenic H3-K27M KO.

4.6 RING1B is enriched at promoters

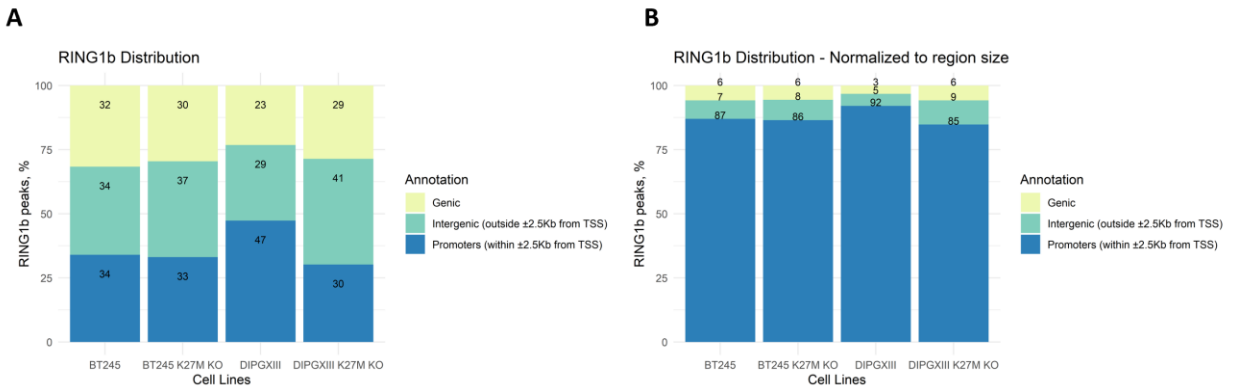

Figure 15. RING1B genomic annotation in H3-K27M and isogenic H3-K27M KO pHGG cell lines.

(A) Stacked barplot showing RING1B peak distribution within the genome without normalization. (B) Stacked barplot showing RING1B peak distribution within the genome after normalization to relative region size. In both figures, promoters are defined as regions within ±2.5Kb from TSS, genic as regions within the genome body and intergenic as non-genic regions beyond ±2.5Kb from TSS. Normalization to relative region size shows high percentage of RING1B falling within promoters across conditions.

To guide our analysis of PRC1, we first investigated the deposition specificity of RING1B across the genome. To do so, we divided the genome into three distinct regions: promoters (defined as regions within ± 2.5Kb from transcription start sites), genic (gene bodies) and intergenic (defined as non-genic regions beyond ± 2.5Kb from transcriptional start sites). Using this annotation, we noticed a comprehensive distribution of RING1B peaks within the genome that evenly encompasses promoters (~36%), genic (~29%) and intergenic regions (~35%) (**Figure 15**). It should be noted, however, that while promoters (here defined as 5,000bp regions) cover a relatively insignificant amount of the genome (<0.1%), they still overlapped with almost one-third of RING1B peaks, thus implying a potential enrichment of PRC1 at promoters.

We then normalized RING1B peak annotations from **Figure 15**A to the relative size of each region (promoter, genic, intergenic). By doing so, we identified that promoter regions showed a

significantly higher enrichment (p-value<1.4e-7) of RING1B deposition than other regions across all cell lines and conditions (**Figure 15**B). We were then able to conclude that PRC1 is preferentially bound to promoters (**Figure 15**B).

4.7 PRC1 is preferentially recruited to promoters with CGIs

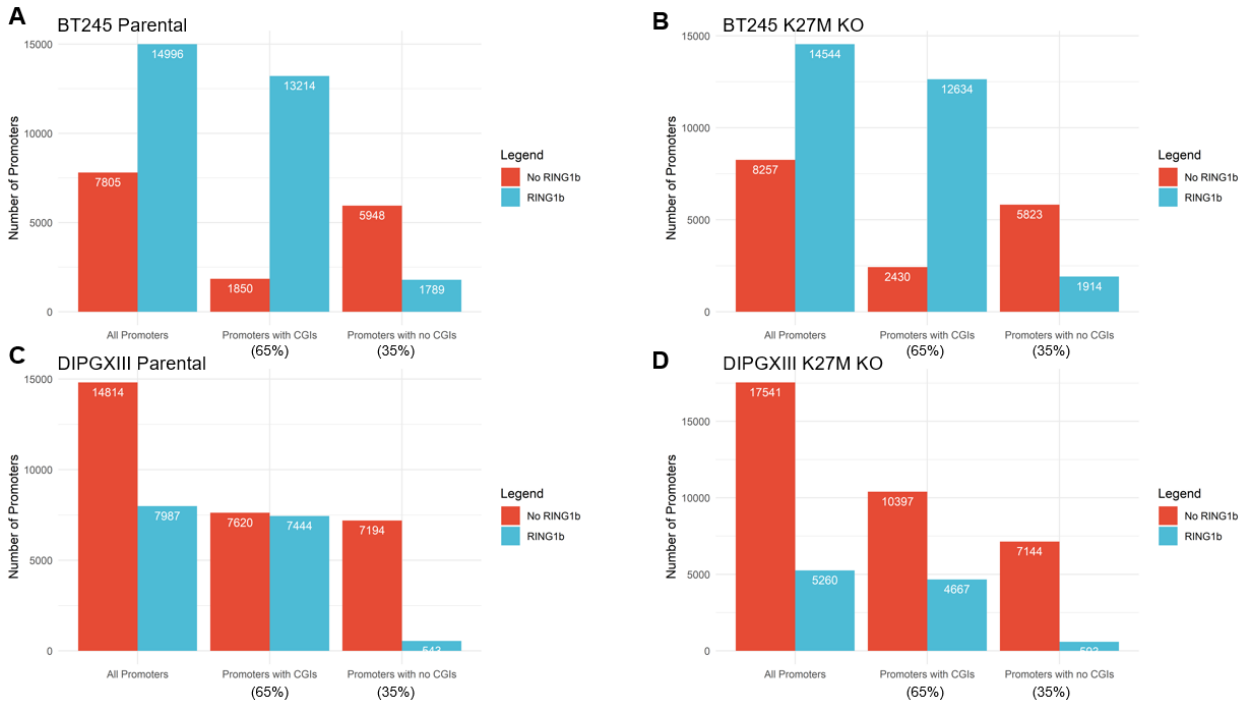

Figure 16. RING1B distribution to promoters in BT245, DIPGXIII and their isogenic H3-K27M KO pHGG cell lines. Barplots showing RING1B occupancy distribution at all promoters, promoters with CGIs and promoters without CGIs in BT245 (A), BT245 isogenic H3-K27M KO (B), DIPGXIII (C) and DIPGXIII isogenic H3-K27M KO (D). RING1B enrichment comparison at promoters with or without CGIs showed a consistent preference for promoters with CGIs. It is observable that most RING1B peaks that overlapped with promoters corresponded to promoters with CGIs across cell lines and conditions.

Unmethylated CGIs are suspected to be equivalent of drosophila PREs in mammalian systems and show documented PRC2 enrichment (21, 28). Given the known PcG interplay (28), we sought to investigate the differential enrichment of RING1B at promoters with or without CGIs.

To do so, we identified that 65% of promoters overlapped with at least one CGI. We referred to these promoters as “promoters with CGIs” or “CGI promoters”. The rest of the promoters contained no CGIs and were labeled as “promoters with no CGIs”. We then mapped the overlap of RING1B peaks in BT245 (H3-K27M), DIPGXIII (H3-K27M) and their isogenic H3-K27M KO conditions to each of the two CGI categories of promoters (**Figure 16**). We observed that the majority of RING1B peaks occupying promoters were recruited specifically to promoters having CGIs. For instance, out of the 14996 promoters occupied by RING1B in BT245 parental cell lines, 13214 (88%) of them were promoters with CGIs whereas only 1789 (12%) were devoid of CGIs.

This significant preference for CGI promoters was replicated in BT245 (H3-K27M), DIPGXIII (H3-K27M) and their isogenic H3-K27M KO conditions (p1=0.89, p2=0.11, p-value<2.2e-16).

While we noticed a difference in the number of PRC1-occupied promoters across cell lines (~13,000 in BT245 parental vs ~7,000 in DIPGXIII parental), these numbers are more perhaps suggestive of the different spatiotemporal origins of the tumors from which they were derived. This was highlighted by the comparable number of identified PRC1-occupied CGI promoters in

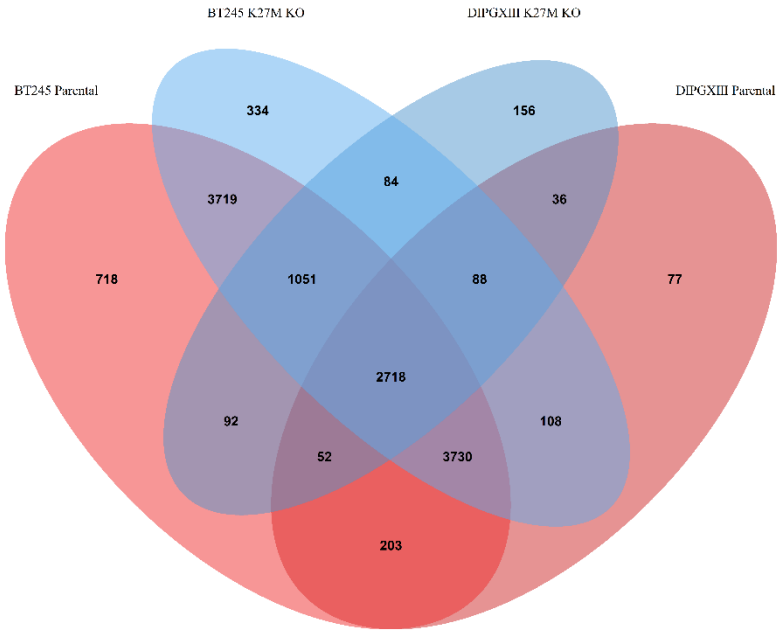

Figure 17. Venn Diagram of PRC1-occupied promoters in Parental (BT245, DIPGXIII) and H3-K27M KO pHGG cell lines.

Identification of RING1B peaks overlapping promoters and comparison across cell lines and conditions show different PRC1 enrichments. A higher overlap is observed between cell lines (11218 in BT245 and 2894 in DIPGXIII) than in histone conditions (203 in H3-K27M and 84 in H3-K27M KO).

BT245 parental (13214) and its isogenic H3-K27M KO (12634) condition, as well as DIPGXIII

(7444) and its isogenic H3-K27M KO condition (4667) (**Figure 16**). Similarly, a larger overlap was seen in each cell line (11218 promoters in BT245 and 2894 promoters in DIPGXIII) when compared with the mutation-specific overlap (203 promoters in H3-K27M and 84 in H3-K27M KO) (**Figure 17**).

4.8 Most PRC1-enriched CGI promoters are H3K27me3-depleted

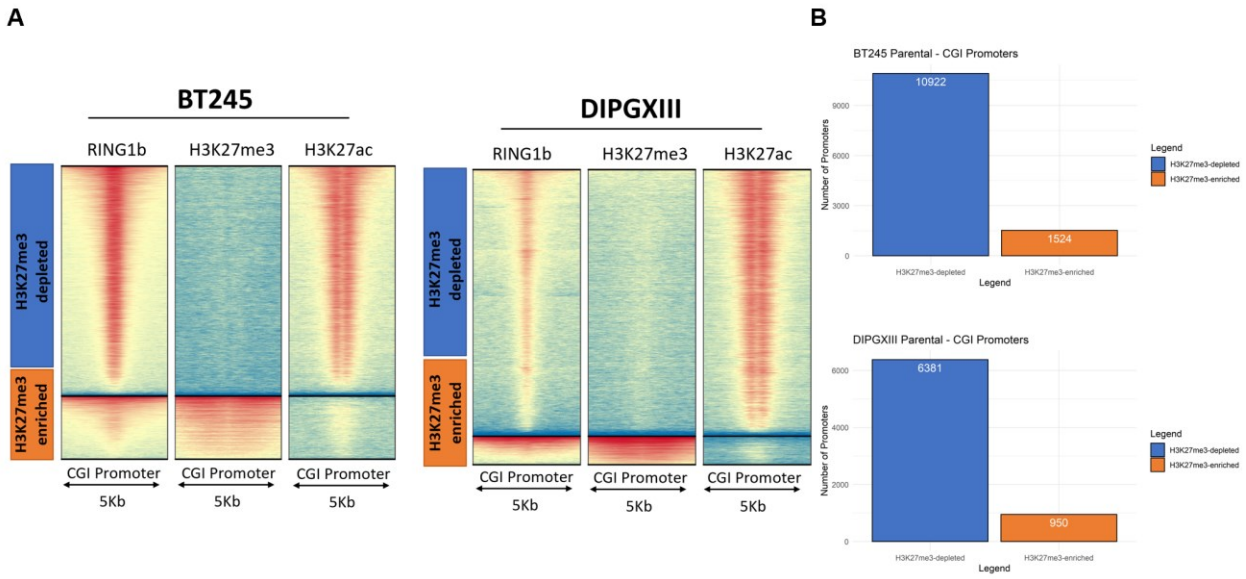

Figure 18. PRC1-occupied CGI promoters separate into H3K27me3-enriched and H3K27me3-depleted clusters.

(A) Stacked heatmap of RING1B, H3K27me3 and H3K27ac ChIP-seq signal on 5Kb CGI promoter windows in BT245 and DIPGXIII parental pHGG cell lines. ChIP-seq signal comparisons of RING1B, H3K27me3 and H3K27ac showed two distinct patterns of enrichment. The orange cluster showing simultaneous enrichment of RING1B and H3K27me3 at promoters was labeled as H3K27me3-enriched promoters. The blue cluster showing RING1B enrichment and H3K27me3 depletion on CGI promoters was labeled as H3K27me3-depleted promoters. Using this approach, we were able to annotate all PRC1-occupied CGI promoters in our H3-K27M pHGG cell lines. (B) Barplots comparing the number of identified H3K7me3-enriched/depleted CGI promoters in BT245 and DIPGXIII parental pHGG cell lines.

For our future analyses, we focused on the previously highlighted promoters with CGIs which showed preferential recruitment of PRC1 (**Figure 16**). By plotting RING1B, H3K27me3

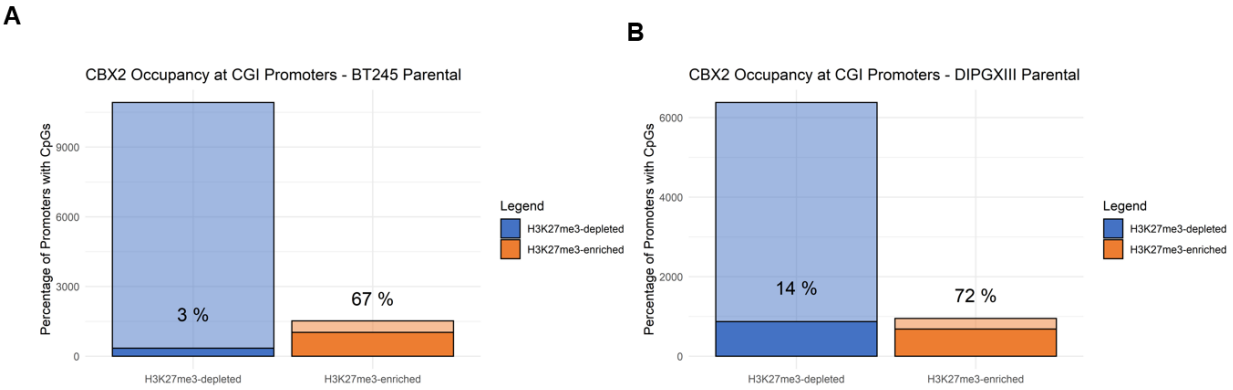

Figure 19. Comparison of CBX2 occupancy at H3K27me3-enriched and H3K27me3-depleted CGI promoters

Barplots comparing CBX2 occupancy at H3K27me3-enriched/depleted CGI promoters in BT245 (A) and DIPGXIII (B) parental (H3-K27M) pHGG cell lines. Comparison of CBX2 peak overlap at H3K27me3-enriched and H3K27me3-depleted CGI promoters (occupied by PRC1) show higher enrichment at H3K27me3-enriched sites as compared with their depleted counterparts.

and H3K27ac ChIP-seq signal enrichment on CGI promoters (**Figure 18**A), we noted that PRC1-occupied promoters largely separate into two clusters. These clusters were defined by the presence or absence of H3K27me3. While the majority of CGI promoters were enriched for RING1B and not H3K27me3 (hereby denoted by "H3K27me3-depleted"), some still showed simultaneous occupancy of PRC1 and H3K27me3. These CGI promoters were labeled as "H3K27me3-enriched". Following this approach, we were able to categorize all CGI promoters into either "H3K27me3-enriched" or "H3K27me3-depleted" in BT245 (H3-K27M) and DIPGXIII (H3-K27M) (**Figure 18**B). By doing so, we were able to identify, consistently, that almost 5/6th of PRC1-occupied CGI promoters are H3K27me3-depleted, whereas only a few of these promoters (1/6) are H3K27me3-enriched (Z-test, p-value=0.03671). Given the H3K27me3-dependent cPRC1 recruitment mechanism, we were compelled to assess the enrichment of cPRC1 at

H3K27me3-enriched CGI promoters. Peak overlap of CBX2, a reader of H3K27me3, shows a higher occupancy at H3K27me3-enriched CGI promoters when compared with their depleted counterparts (**Figure 19**).

4.9 H3K27me3-enriched CGI promoters are more repressed than their depleted counterparts

To further characterize the different categories of PRC1-occupied CGI promoters, we next compared the difference in gene expression between H3K27me3-enriched and H3K27me3-depleted promoters. By contrasting gene transcription reads per kilobase of transcript per million (RPKM) levels, we observed, consistently across cell lines, that H3K27me3-enriched promoters corresponded to genes that were significantly more repressed than genes with H3K27me3-depleted promoters (**Figure 20**). Unpaired student's t-test comparing global RPKM levels show a consistent lower level of expression in H3K27me3-enriched promoters than in their depleted counterparts (p-value<2.2e-16).

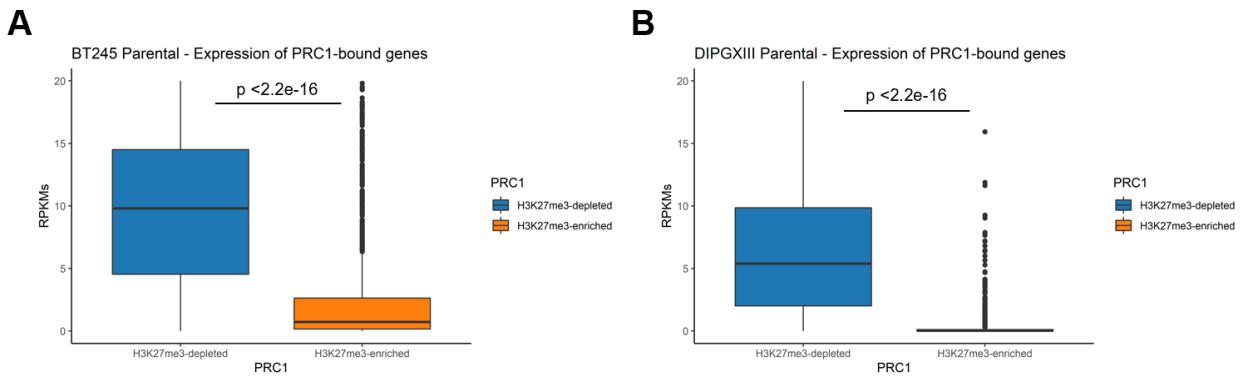

Figure 20. Gene expression comparison between H3K27me3-enriched and H3K27me3-depleted promoters

Boxplot comparing gene expression RPKMs of H3K27me3-enriched and H3K27me3-depleted CGI promoters in BT245 (A) and DIPGXIII (B) parental (H3-K27M) pHGG cell lines. Unpaired Student's t-test comparing overall gene expression levels show significant differences in expression pattern between H3K27me3-enriched and H3K27me3-

depleted promoters. Specifically, H3K27me3-enriched CGI promoters corresponded to genes that were significantly more repressed than their H3K27me3-depleted counterparts.

4.10 PRC1 show increased recruitment to H3K27me3-enriched CGI promoters in H3-K27M conditions

Given our previous observation showing increased coupling of PRC1 and PRC2 at H3K27me3 sites in H3-K27M conditions (**Figure 13**), we were interested in investigating this trend specifically at CGI promoters (previously shown to be PRC1 preferential binding sites in **Figure 16**). Therefore, we first identified H3K27me3-enriched/depleted CGI promoters common to BT245 and DIPGXIII parental as well as isogenic H3-K27M KO pHGG cell lines (**Figure 21**). These would allow us to better identify patterns that are more directly associated with the H3-K27M mutation. We report 430 common H3K27me3-enriched and 1431 common H3K27me3-depleted CGI promoters across all conditions and cell lines of interest as highlighted in **Figure 21**B. We next proceeded to assess PRC1 recruitment at these common sites by plotting and quantifying the proportion of RING1B and H2AK119ub ChIP-seq reads that aligned to these common CGI promoters (**Figure 22**B). In confirmation with our previous observation, we noticed increased PRC1 read percentages at H3K27me3-enriched CGI promoters in H3-K27M conditions (**Figure 22**B**).** Both RING1B and H2AK119ub showed higher enrichment at H3K27me3-enriched promoters as seen by the increased intensity of signal in **Figure 22**A (blue panel).

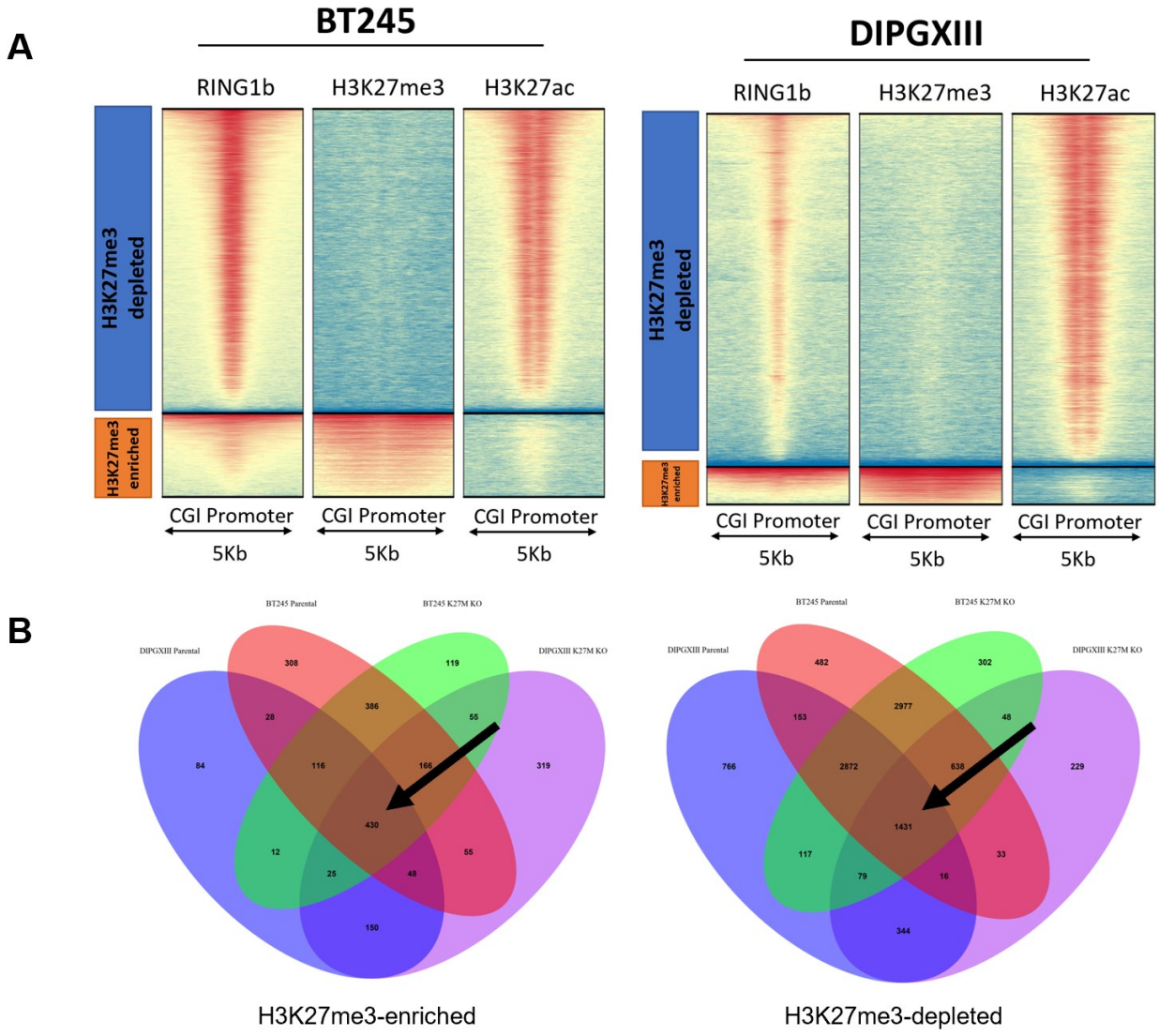

Figure 21. Identification of H3K27me3-enriched and H3K27me3-depleted in BT245, DIPGXIII and isogenic H3-K27M KO pHGG cell lines.

(A) Stacked heatmap of RING1B, H3K27me3 and H3K27ac ChIP-seq signals on CGI promoters. (B) Venn diagram comparing the overlap of H3K27me3-enriched and H3K27me3-depleted CGI promoters in BT245 and DIPGXIII parental as well as isogenic H3-K27M KO conditions. Using H3K27me3-enriched vs H3K27me3-depleted annotation of CGI promoters across cell lines and conditions, we were able to identify 430 H3K27me3-enriched and 1431 H3K27me3-depleted CGI promoters occupied by PRC1 that were common to all our cell line models and conditions.

We next investigated whether this increased PRC1 overlap at H3K27me3-enriched CGI promoters had titrating effects on PRC1 occupancy at H3K27me3-depleted counterparts. Following the same approach as before, both ChIP-seq enrichment and read percentage quantifications showed non-significant changes in PRC1 at H3K27me3-depleted CGI promoters across conditions for RING1B (p-value=0.862) and H2AK119ub (p-value=0.871).

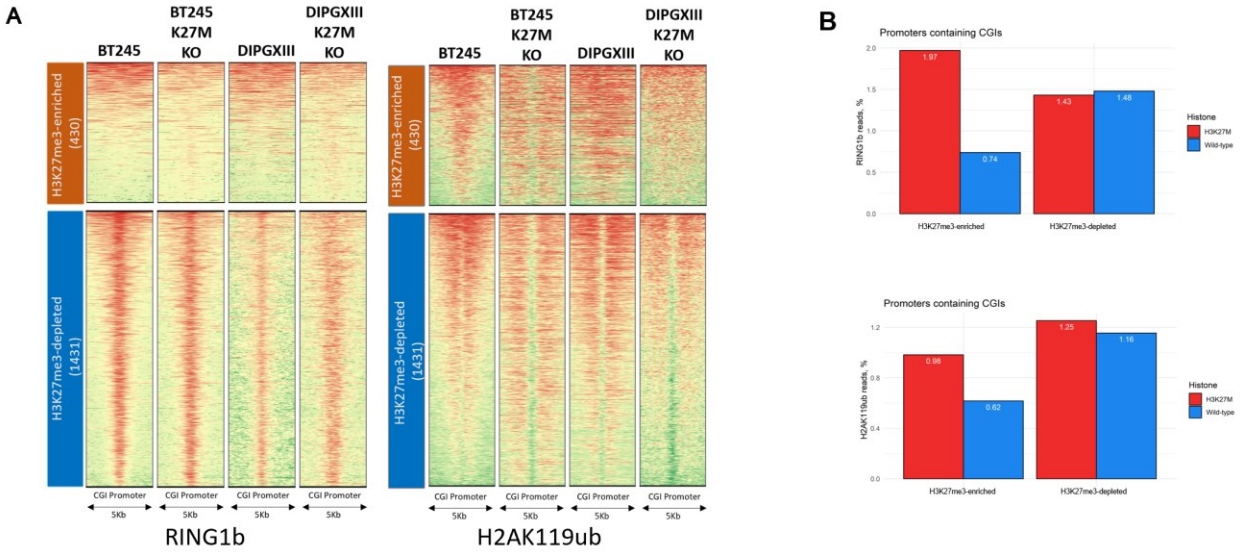

Figure 22. RING1B and H2AK119ub enrichment comparison at H3K27me3-enriched and H3K27me3-depleted CGI promoters in H3-K27M and isogenic H3-K27M KO pHGG cell lines.

(A) Stacked heatmap showing RING1B and H2AK119ub enrichment at common H3K27me3-enriched and -depleted CGI promoters in parental and H3-K27M KO pHGG cell lines. (B) Barplot quantification of RING1B and H2AK119ub ChIP-seq read percentage at common H3K27me3-enriched and -depleted CGI promoters in parental and H3-K27M KO conditions. ChIP-seq enrichment and input-normalized RPKM quantifications of RING1B and H2AK119ub show an increase at H3K27me3-enriched CGI promoters in H3-K27M conditions. Enrichment of RING1B and H2AK119ub at H3K27me3-depleted CGI promoters show comparable levels across conditions.

These combined results confirm the increased enrichment of PRC1 at CGI promoters tagged with H3K27me3. Such increased overlap and recruitment, however, did not titrate PRC1 away

from other CGI promoters as they still maintained comparable enrichment of RING1B and H2AK119ub across conditions.

4.11 PRC1 increased recruitment and overlap H3K27me3-enriched CGI promoters was not associated with global changes in RPKM levels

We were next interested in understanding whether the increased recruitment of PRC1 to H3K27me3-enriched promoters in H3-K27M conditions was associated with changes in global levels of expression. To do so, we compared global gene expression levels of the 430 common H3K27me3-enriched CGI promoters in both parental (BT245 and DIPGXIII) and isogenic H3-K27M KO conditions (**Figure 23**).

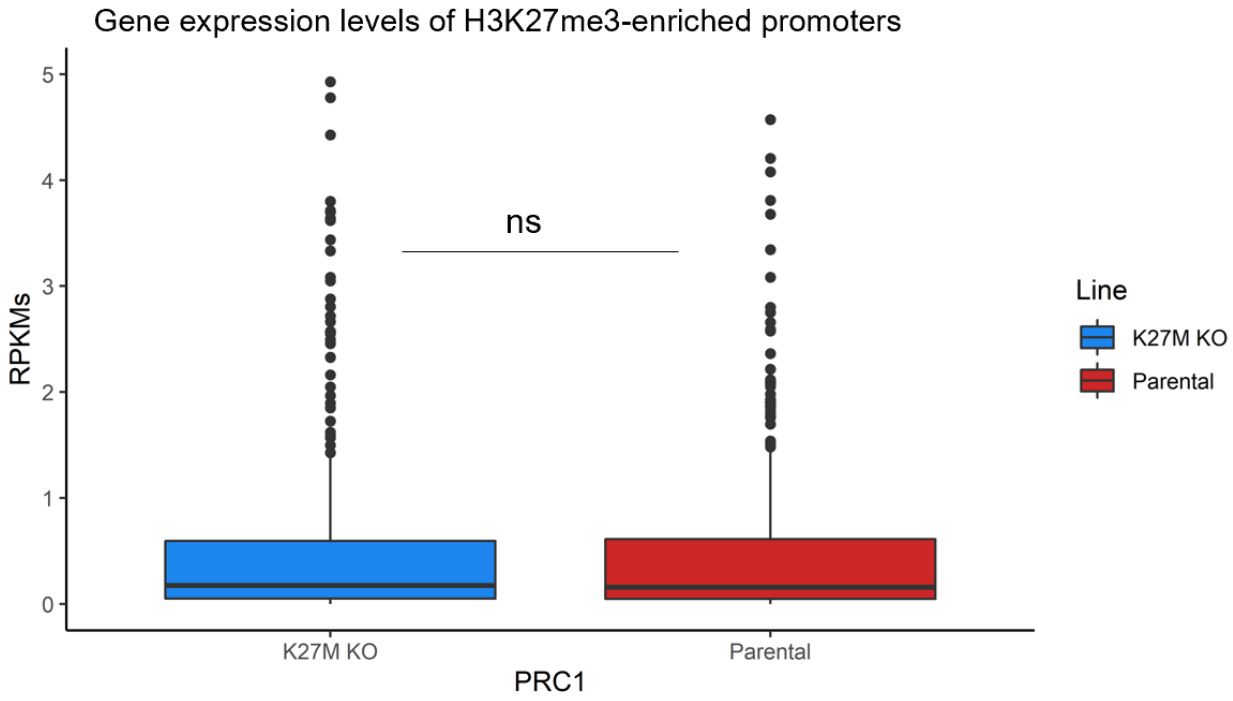

Figure 23. Gene expression comparison of H3K27me3-enriched CGI promoters in H3-K27M and isogenic H3-K27M KO pHGG cell lines.

Boxplot comparing gene expression RPKM levels of common H3K27me3-enriched CGI promoters in parental (red) and H3-K27M KO conditions (blue). Comparison of gene expression RPKM levels of H3K27me3-enriched CGI promoters

show no significant changes across pHGG histone conditions. Unpaired student's t-test comparing global RPKM levels yielded a p-value of 0.384 for n=430.

We show that H3K27me3-enriched CGI promoters globally maintained similar RPKM levels (p-value=0.384) across conditions. These observations demonstrate that the increased overlap and recruitment of PRC1 at H3K27me3-enriched CGI promoters in H3-K27M conditions was not associated with a significant impact on global gene expression.

4.12 PRC1 differential recruitment to promoters was associated with little changes in expression

To better delineate the impact of PRC1 redistribution on gene expression changes in H3-K27M conditions, we then looked at promoters showing differential recruitments (gain/loss) of RING1B and compared them with RNA-seq patterns. For a more comprehensive overview, we combined CGI promoters with non-CGI promoters showing differential recruitments and obtained a total of 238 promoters that gain PRC1 and 171 promoters that lose PRC1 in H3-K27M conditions (**Figure 24**).

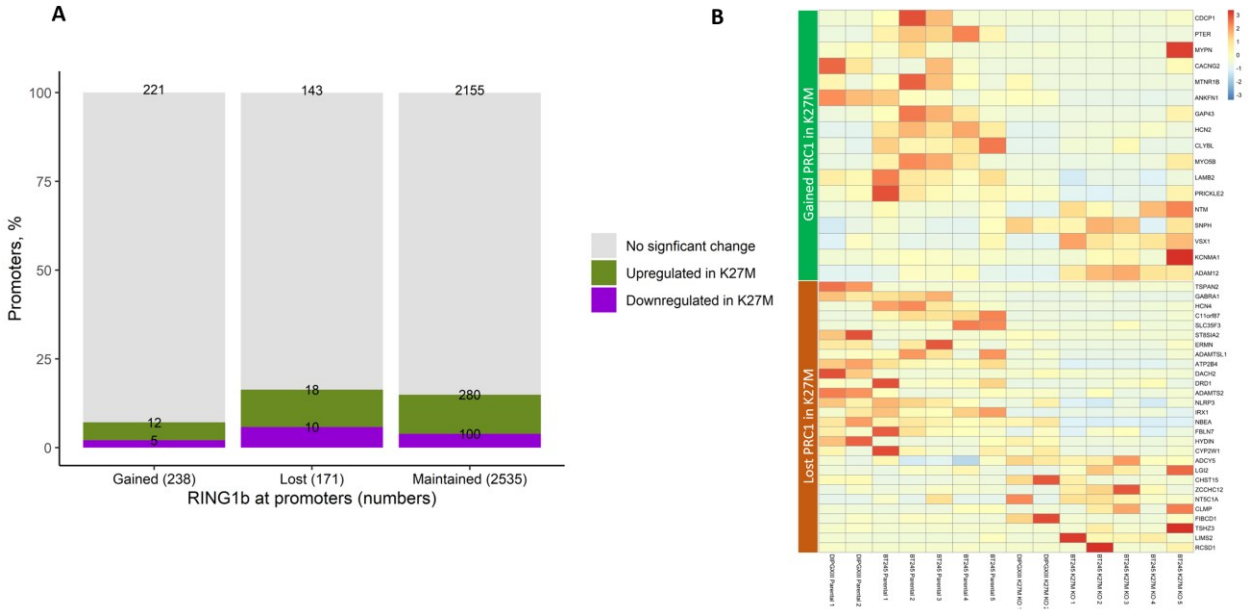

Figure 24. Association of differential PRC1 recruitment with changes in expression in H3-K27M vs isogenic H3-K27M KO pHGG cell lines.

(A) Barplot showing the percentage and number of significantly differentially expressed genes at differential PRC1 promoters (gained, lost and maintained). (B) Heatmap showing all differential expressed genes associated with promoters that gain (green) or lose PRC1 (orange) recruitment in H3-K27M conditions. Comparison of differential PRC1 recruitments with transcriptional levels in H3-K27M conditions show limited association between PRC1 gain/loss and changes in gene expression. Most differentially expressed genes were at promoters that maintained PRC1 occupancy across conditions. Similarly, gain/loss of PRC1 recruitment to promoters was not associated with a clear pattern of changes in expression as genes still showed both up- and down-regulation trends.

Surprisingly, the proportion of genes that showed differential expression upon PRC1 recruitment/ loss of recruitment in H3-K27M was very minimal when compared with maintained sites (Chi-square test, p-value=0.033). This was further complicated by the observation that these genes showed comparable up- and down-regulatory effects (Chi-square test, p-value=0.66) upon differential PRC1 recruitment to promoters (**Figure 24**A). For instance, PRC1 was gained at promoters of both *CYLBL* and *ADAM12* in H3-K27M conditions, yet these genes showed up-regulation and down-regulation, respectively, in H3-K27M pHGG cell lines.

Of further importance, PRC1 at these promoters was found to be equally associated with repressive H3K27me3 or activating H3K7ac marks yet could still demonstrate both and up- and down-regulation trends. For illustration, we have included 4 sites that showed the combination of possible associations and gene expression changes (**Figure 25).**

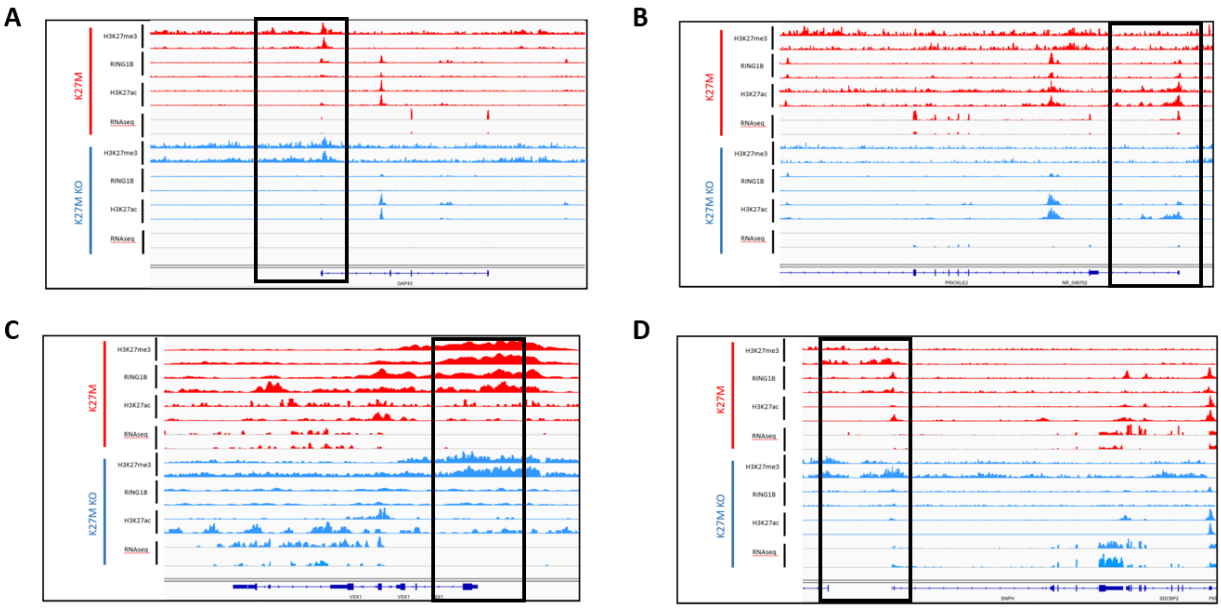

Figure 25. ChIP-seq and RNA-seq tracks of promoters showing a gain of RING1B recruitment

ChIP-seq tracks comparison of promoters with gained PRC1 recruitment show different associations with either H3K27me3 or H3K27ac modifications. Note that these genes were either upregulated (A and B) or downregulated (C and D) in H3-K27M conditions.

GAP43, a gene involved in neuronal development, showed a gain of PRC1 recruitment at its promoter in H3-K27M condition (**Figure 25**A). While this promoter maintained H3K27me3 deposition, albeit with reduced spread, it was significantly upregulated when compared with isogenic K27M KO contexts. Similarly, *VSX1* gains RING1B at its promoter, is associated with H3K27me3 but is down-regulated in H3-K27M conditions (**Figure 25**B). In contrast, *PRICKLE2* shows a gain of RING1B at its promoter, is associated with H3K27ac and is upregulated in H3-

K27M conditions (**Figure 25**C). Meanwhile, *SPNH* shows the same gain of RING1B recruitment and H3K27ac association but is downregulated in K27M conditions (**Figure 25**D).

Chapter 5: Discussion

A large proportion of pHGGs are characterized by the presence of somatic mutations of the histone H3 genes (32, 63). Almost 50% of these pHGGs harbor point mutations on either the K27 or the G34 residue of histone H3 N-tail and show distinct spatio-temporal specificities (32, 63). H3-K27M is now known to be a driver of tumorigenesis and exerts its dominant negative effects through H3K27me2/3 reduced deposition, changes in DNA methylation pattern and increased H3K27ac pervasiveness (12, 32). These events have been shown to lead to gene expression signatures implicated in tumor formation and progression (32). In mammals, H3K27me3 is largely deposited by the EZH2 catalytic component of the Polycomb Repressive Complex 2 (PRC2) (32). H3-K27M inhibits EZH1/2 histone-methyltransferase activity (32), and our group has further shown that the spread into repressive domains of H3K27me3 mark and to lesser extent that of H3K27me2 is affected in the context of H3-K27M (12). This reduced spread creates confined H3K27me3 deposition patterns similar to that seen in embryonic stem cells and is suspected to be associated with gene de-repression events implicated in tumorigenesis (12). PRC1, another multi-subunit member of the PcG family, is known to recognize the H3K27me3 mark deposited by PRC2 (21, 28, 38). Given that PRC1 is also involved in gene regulation through deposition of H2AK119ub repressive marks, chromatin compaction and chromatin looping, it was compelling to analyze the role of PRC1 in H3-K27M pHGGs (21, 38). To characterize the role and distribution of PRC1 in a tumorigenic context, we performed ChIP-seq on the catalytic core component of PRC1 (RING1B), a chromodomain reader of H3K27me3 that characterizes cPRC1 complexes (CBX2) as well as the H2AK119ub modification catalyzed by all PRC1 complexes.

While H3K27me2/3 levels are globally reduced in H3-K27M contexts (**Figure 3**), we show that H2AK119ub deposited by PRC1 maintains similar abundance as with isogenic H3-K27M KO conditions (**Figure 4**). Western blot quantification in two H3-K27M cell lines (BT245 and DIPGXIII) as well as two isogenic H3-K27M KO clones do not show significant changes in H2AK119ub levels (**Figure 4**). Similarly, ChIP-Rx, an optimized method that uses an internal calibration system to make signal quantifications more precise, also shows comparable levels of H2AK119ub (**Figure 5**).

H3K27me3 maintains its deposition, albeit in a reduced fashion, at CpG islands known to recruit PRC2 in mammalian systems (10, 12). Given the recruitment interplay between PRC1 and PRC2 at specific sites (28), we investigated H2AK119ub deposition patterns around CGIs in comparison with H3K27me3. We observed a highly comparable enrichment of H2AK119ub in H3-K27M and H3-K27M KO conditions (figures 4 and 5). While H3K27me3 was susceptible to confined enrichment around CGIs, H2AK119ub spread remained globally unperturbed by the presence of the H3-K27M mutation and greatly resembled histone wild-type conditions (figure 5). H2AK119ub showed a wide distribution across gene bodies and intergenic regions – a pattern that is similar to the widespread H3K27me2 in H3-K27M conditions (12, 44). This pattern of spread was widely conserved across histone conditions (**Figure 6**).

These observations can be explained by the limited contribution of cPRC1-mediated H2AK119ub deposition to overall H2AK119ub levels (21). In fact, studies have reported that non-canonical components of PRC1 amplify RING1B E3 ubiquitin ligase activity and that ncPRC1 are responsible for at least 70% of H2AK119ub deposition (21, 46). RYBP in specific, a non-canonical component of PRC1, was found to stabilize RING1B by decreasing its proteasomal degradation and to enhance its catalytic activity (46). This further supports the

increased catalytic activity of ncPRC1 when compared to cPRC1 (21, 46). Additionally, studies report a reduced catalytic activity of RING1A/B upon binding to canonical components such as Ph homologs (PHC1-3) (28, 39). Given the restricted catalytic activity of cPRC1 and the small percentage of sites that follow an H3K27me3-dependent cPRC1 recruitment, it is of no surprise that H3K27me3 reduced levels were not associated with a large drop in H2AK119ub deposition levels (28, 39). We expect for H3-K27M to demonstrate its most immediate effects on cPRC1 rather than ncPRC1 which is corroborated by the large maintenance of H2AK119ub spread and levels in H3-K27M pHGG cell lines. Of further support to our context, it has been reported that H2AK119ub levels and deposition are maintained in ESCs that lack either PRC2 activity or canonical PRC1 components (39). These studies also suggest that cPRC1 complexes are enriched at chromatin compacted sites already having H3K27me3 and H2AK119ub and that cPRC1 mediates its gene regulatory role mainly through chromatin restructuring rather than H2AK119ub deposition (39).

We next sought to map the distribution of PRC1 through RING1B and CBX2 ChIP-seq analyses. We find that, unlike PRC2 which is recruited to only 15% of all CGIs, PRC1 is bound to most CGIs (~60%) (**Figure 27**). This observation was in line with the observation that KDM2B, a non-canonical component of variant PRC1.1, can initiate de-novo polycomb domains at CGIs through its nonmethylated DNA binding ability (39). Nevertheless, studies show that PRC1 regular recruitment or induced loss from CGIs were not associated with significant changes in expression (39). This suggests that PRC1 transient binding at CGIs has more of a conservative role by limiting stochastic gene re-activation rather than actively repressing transcription (39).

To obtain a better understanding of PRC1 and its association with PRC2 and other histone modifications, we used k-means clustering (112, 114) on all RING1B peaks called in BT245

pHGG cell line (H3-K27M) and its isogenic H3-K27M KO conditions. We used ChIP-seq maps from active (H3K4me3, H3K36me2) and enhancer-associated (H3K4me1, H3K27ac) post-translational modifications as well as PRC1-related (RING1B, CBX2, H2AK119ub) and PRC2-related (SUZ12, H3K27me1/2/3) factors to gain an overview of the epigenetic landscape of our pHGG models. At k=6, we obtained an optimal separation of the 60,000 peaks into 6 clusters enriched for either H3K27me1/2/3 (repressive) or H3K27ac (active) with a combinatorial enrichment for H3K4me1/3 (**Figure 9**).We then compared these different associations across histone conditions and reported a significantly increased association between PRC1 and PRC2 in H3-K27M in the cluster enriched for H3K27me3 (**Figure 10**). Cluster 5, which was mostly composed of intergenic regions and promoters, maintained enrichment of H3K27me3 in H3-K27M conditions and was directly relevant to addressing our hypothesis (**Figure 10**).

We next sought to assess this increased overlap between PRC1 and PRC2 at H3K27me3 sites in H3-K27M pHGGs. As previously reported, H3K27me3 show a reduced spread around CGIs in H3-K27M conditions (12). Removal of the H3-K27M mutation in pediatric high-grade glioma contexts show a gain of spread of H3K27me3 into widespread repressive domain and a subsequent increase in the global levels of this histone modification (12). Using the same models, we noticed that RING1B, CBX2 and H2AK119ub show an increased enrichment and overlap at H3K27me3 sites in H3-K27M when compared with isogenic H3-K27M KO conditions (figure 9). In these contexts, knock out of H3-K27M allowed H3K27me3 to gain its spread as well as lose its strong overlap with cPRC1 components (figure 10). Quantification of input-normalized RPKMs correlation of ChIP-seq reads from SUZ12, H3K27me1/2/3, RING1B, H2AK119ub and CBX2 in BT245 and DIPXIII pHGG cell lines show a significant increased coupling of PRC1 and PRC2 in H3-K27M conditions (**Figure 13** and **Figure 14**). These

observations are highly reminiscent of PcG interplay in embryonic stem cells where H3K27me3 is similarly confined in its deposition pattern and where most PRC1 recruitment is restricted to H3K27me3 sites (40). In these contexts, only EZH1/2 disruption largely destabilized RING1B occupancy at shared PcG sites and little deposition of H3K27me3 was enough to maintain RING1B binding in EZH1 KO ESCs (40). These observations provide compelling proof to surmise that H3K27me3 focal deposition is a strong recruiter of cPRC1 (40). While no studies have compared the differential PRC1 recruitment patterns of confined versus spread H3K27me3, we note an elevated PRC1 occupancy at shared PcG sites in H3-K27M contexts where H3K27me3 shows reduced spread (**Figure 11**). CBX2, which is the only CBX protein to have a predominant affinity for H3K27me3 over H3K9me3 (41), shows a similar increased enrichment at H3K27me3 foci in H3-K27M conditions (**Figure 27**). This suggests that CBX2 may be driving cPRC1 localized occupancy at H3K27me3 sites in H3-K27M pHGGs. Quantification of H3K27me3 read percentage shows that a consistent elevation in its deposition at PcG sites (**Figure 13**). H3K27me3 spread beyond PRC2 nucleation sites is restricted by H3-K27M (12) which may be then acting as a localized recruitment site of cPRC1 as seen in CBX2 and RING1B overlaps.

To better investigate the contribution of this increased coupling of PRC1 and PRC2 to tumorigenesis, we first sought to characterize PRC1 recruitment sites. Annotation of RING1B peaks in H3-K27M and isogenic H3-K27M KO pHGG cell lines shows a consistent enrichment for promoter regions (**Figure 15**). As mentioned earlier, mammalians do not rely on PREs to recruit PcG machinery but rather show enrichment of polycomb domains at unmethylated GC-rich regions (CGIs) (10, 42). While 65% of promoters overlap with at least one CGI and the rest are devoid of any, RING1B was mostly deposited at promoters with CGIs (**Figure 16**). This led

us to conclude that PRC1 is preferentially recruited to promoters with CGIs (**Figure 16**). This observation parallels PRC2's enrichment at CGIs of promoters of repressed PcG targets (43). In our pHGG contexts, CGI promoters clustered into two categories: H3K27me3-enriched and H3K27me3-depleted (figure 16A). While few PRC1-occupied CGI promoters were enriched for H3K27me3, the large majority were instead tagged with active H3K27ac marks. This different proportion in association may be linked to the lineage and differentiation stage of the cell of origin of these tumors (13). In fact, our reported associations greatly differ from embryonic stem cell contexts where PRC1 shows limited deposition outside of repressed regions (45, 51).

Moreover, H3K27me3-enriched CGI promoters corresponded to genes that were significantly more repressed than their H3K27me3-depleted counterparts (**Figure 20**). These observations are in support of studies that characterize H3K27me3 enrichment at transcriptionally silenced sites (44). Given the documented mutual exclusivity of H3K27ac and H3K27me3 and the required PRC2 displacement for H3K27ac deposition at promoters (45), we used H3K27ac and RING1B overlap at CGI promoters to identify H3K27me3-depleted sites. Undoubtedly, these active sites corresponded to genes with higher transcriptional activity than their H3K27me3-enriched counterparts (**Figure 20**). It should be noted that despite the impact of H3-K27M on H3K27me3 deposition, no PRC1-occupied CGI promoters showed a switch from H3K27me3-enriched to H3K27me3-depleted, or vice versa, across pHGG conditions. This is in line with our previous studies that no report new H3K27ac sites were created in association with H3-K27M and that the few sites that gain H3K27me3 in H3-K27M were mostly intergenic (12, 13).

Furthermore, H3K27me3-enriched and H3K27me3-depleted CGI promoters were occupied by different subtypes of PRC1 complexes. CBX2 is found to be highly enriched at H3K27me3-enriched CGI promoters which suggests strong recruitment of cPRC1 to these sites (**Figure 19**).

Similarly, H3K27me3-depleted CGI promoters relied on H3K27me3-independent PRC1 recruitment mechanisms as CBX2 was found to be also depleted at these sites. This last observation provided compelling reason to suspect that ncPRC1 complexes, which harbor direct DNA-binding abilities, are recruited to these sites. Comparison of these sites with online ChIP-seq databases show a strong enrichment of KDM2B in multiple cell types (**Figure 28** and **Figure 29**). This provides substantial evidence to suspect that these sites may be occupied by ncPRC1 complexes, involve diverse recruitment mechanisms and demonstrate different catalytic activities.

To further characterize PRC1 recruitment across H3K27me3-enriched/depleted CGI promoters, we identified 430 common H3K27me3-enriched and 1431 H3K27me3-depleted CGI promoters across our different cell models and histone conditions (**Figure 21**). Using these common promoters, we show an increased PRC1 recruitment and H2AK119ub deposition to H3K27me3-enriched CGI promoters in H3-K27M pHGGs when compared with isogenic H3-K27M KO conditions (**Figure 22**). These findings support our previously discussed increased PcG coupling and overlap at H3K27me3 sites in H3-K27M conditions. While this increased occupancy of cPRC1 to these promoters was associated with the H3K27me3 reduced spread, it had no significantly discernable impact on global gene expression levels (**Figure 23**). Therefore, it may be likely that increased cPRC1 occupancy at these promoters was a more of a passive consequence to the H3K27me3 focal deposition. In fact, RING1B and H2AK119ub were found to be increased in deposition at promoters of genes that were up-regulated, down-regulated or maintained expression across histone conditions (**Figure 30**). Interestingly, cPRC1 increased recruitment drove stronger chromatin contacts (Hi-C) at these sites as seen in BT245 (**Figure 31**). Specifically, we observe increased chromatin interaction overlapping RING1B sites at some

H3K27me3 sites. For instance, FOXP1, a gene upregulated in BT245, shows a strong chromatin contact with an active enhancer region that is mediated by increased cPRC1 occupancy at an H3K27me3-enriched CGI in H3-K27M conditions. This is in confirmation with recent studies showing increased chromatin contact frequencies at sites showing high PRC1 levels (35, 47). While PRC1 has been shown to be heavily implicated in mediating long-range chromatin looping throughout development (35, 36, 47, 52), a detailed understanding to of contributions in cancer is still lacking. Nonetheless, such increased association between cPRC1 occupancy and stronger chromatin contacts warrants further future investigation of its role in tumorigenesis.

Unlike many cancers where PRC1 components act as oncogenes or tumor suppressors (26, 27, 48, 49), pediatric high-grade gliomas demonstrate virtually no significant changes in expression of PRC1 components (**Figure 33** and **Figure 38**). Specifically, RING1B and H2AK119ub western blot analyses show similar protein levels across different histone conditions of pHGGs (**Figure 32**). Since PRC1 show increased enrichment and H2AK119ub deposition at H3K27me3-enriched promoters, we were compelled to assess whether H3K27me3 reduced spread titrated PRC1 recruitment away from H3K27me3-depleted sites. Using the identified 1431 H3K27me3-depleted CGI promoters, we report no significant changes in RING1B and H2AK119ub enrichments across histone conditions (**Figure 22**). This provided initial proof that PRC1 may not be losing its binding frequency at other CGI promoters in H3-K27M contexts. Nevertheless, this approach needs to be complemented by further characterization of non-promoter PRC1 targets.

To obtain a clearer depiction of PRC1 redistribution, we then shifted our focus towards promoters with differential PRC1 binding (gain/loss) in H3-K27M pHGGs. For this analysis, we looked at all promoters (CGIs and non-CGIs) and identified 238 promoters that gain PRC1 and

171 promoters that lose PRC1 binding in H3-K27M condition (**Figure 24**). Most promoters (2535) maintained PRC1 recruitment across conditions. By comparing PRC1 differential binding and gene expression changes, we observe insignificant association between PRC1 changes in recruitment and gene de-regulation. Specifically, it was promoters where PRC1 binding was maintained across conditions that showed the most changes in expression. Furthermore, promoters showing differential PRC1 binding in H3-K27M conditions were not associated with a clear trend of up-or down-regulation of expression (**Figure 24**). Additionally, while PRC1 at all of these promoters was associated with either H3K27me3 or H3K27ac, they could still show both up-and down-regulation in H3-K27M conditions (**Figure 25**). Overall, these observations hint at the little contribution that PRC1 redistribution has on direct changes in expression. These observations are in line with the current understanding of PRC1's role in modulating chromatin accessibility (50). Studies show that while PcG-occupied promoters were characterized with reduced chromatin accessibility, PRC1-null models were not enough to create global accessibility changes (50). These observations suggest that PRC1 requires the involvement of other chromatin remodeling complexes, such as BAF, to demonstrate chromatin accessibility changes (50). Similarly, gain of H2AK119ub at promoters due to ectopic PRC1 recruitment in H3-K27M conditions showed no clear patterns of repression. In ESCs, H2AK119ub tethers PcG machinery to repressed loci by linking PRC1 to PRC2 (51). This suggests a model where H2AK119ub has a repressive function only in collaboration with PRC2 (51). Such models might explain the little association between PRC1 gain of recruitment and changes in expression in our models. In fact, H3-K27M largely restricts H3K27me3 deposition and spreading which might explain the insignificant impact of H2AK119ub gain at some promoters in absence of functional PRC2 catalysis. Overall, PRC1 differential binding to promoters may not be enough to lead to

direct changes in gene expression. To better characterize PRC1 redistribution and its association with tumorigenic transcriptional changes, it would be interesting to map RING1B in more differentiated contexts where PcG and TxcG machinery can be induced to interplay.

Furthermore, while H3-K27M mutations unanimously exerts its effects on H3K27me3 spread, H3K27me3 deposition may differ based on cell type and differentiation state. Given that H3-K27M pHGGs can arise from different midline brain locations and may exhibit different H3K27me3 enrichments, it would be also interesting to characterize PRC1 redistribution in association to tumorigenesis based on the cell context. Such a focused approach may better highlight the impact of PRC1 increased recruitment to H3K27me3 sites and potentially unravel its context-specific contributions to oncogenic events. Similarly, it would be compelling to distinguish the different roles of PRC1 by preventing its catalytic deposition of H2AK119ub. Mutations affecting the I53 residue of RING1B (I53A/S) have been shown to interfere with PRC1's E3-ubiquitin ligase activity and to largely reduce H2AK119ub levels in embryonic stem cells without affecting PRC1 assembly and formation of PcG chromatin bodies (28, 51). By incorporating similar systems into our H3-K27M pHGG models, we could obtain a better characterization of PRC1 catalytic role in association to tumorigenesis and separate it from its chromatin looping activity. Alternatively, knockdown models of RING1A/B and CBX2 could provide a clearer insight as to the roles of PRC1 and canonical PRC1 complexes, respectively, in H3-K27M pHGGs. Specifically, knocking out CBX2 could help uncouple cPRC1 from PRC2 and potentially have different effects based on H3-K27M mutation status. In fact, CBX2 overexpression in cancers is suspected to confer survival advantage by maintaining CDKN2A and INK4A/ARF repression (42). As shown in **Figure 12**, CDKN2A is a site showing increased PRC1 overlap with H3K27me3 in H3-K27M. This provides compelling reasons to hypothesize

that increased cPRC1 overlap with H3K27me3 (mediated by CBX2) can mimic CBX2 oncogenic effects. Therefore, knocking-out CBX2 can provide better characterization of the increased PRC1/2 coupling seen in H3-K27M conditions and shed light on potential therapeutic strategies. CBX chemical probes have been developed that compete with H3K27me3 by binding to chromodomains of CBX4/7 and are suspected to exert synergistic effects with EZH2 pharmacological inhibitions (53). While CBX4 and CBX7 are not highly expressed in our models (**Figure 33**), it would still be interesting to chemically uncouple PRC1 from PRC2 in conjunction to EZH2 inhibition, specially that this latter treatment has already proven effective in decreasing cellular survival of H3-K27M pHGGs by our group (12).

Chapter 6: Conclusion

In brief, we show an increased recruitment and overlap of PRC1 at H3K27me3 sites in H3-K27M pHGGs. H3K27me3 reduced spread strongly couples PRC1 and PRC2 as seen in their increased overlap (**Figure 13**). Specifically, CGI promoters enriched for H3K27me3 showed increased PRC1 binding and H2AK119ub deposition. This increased enrichment for cPRC1 was not associated with changes to the global transcriptional levels of these sites and did not decrease PRC1 occupancy at H3K27me3-depleted CGI promoters. Additionally, PRC1 redistribution at promoters in H3-K27M pHGGs was not associated with a significant pattern of changes in gene expression. Gain or loss of PRC1 at promoters tagged with different histone modifications showed no clear trends with changes in transcriptional profiles. While we identify patterns of PRC1 redistribution in H3-K27M HGGs, a better characterization of its contribution to tumorigenesis is still missing and requires the need for H3-K27M HGG contexts where either PRC1 assembly or catalytic activity are disrupted.

Chapter 7: Future Directions

7.1 RING1B, CBX2 and H2AK119ub chromatin immune-precipitation followed by high-throughput sequencing on more pediatric high-grade glioma models

Further replicates of pHGG ChIP-seq samples will be performed to robustly support our observations. The addition of more pHGGs samples will strengthen the validity of our increased PcG coupling observation and allow for a better understanding of its association with transcriptional profiles. Specifically, the addition of HSJ-19, an H3-K27M patient-derived tumor cell line with a matched isogenic H3-K27M KO clone, will potentially further corroborate PRC1's increased recruitment and overlap at H3K27me3 sites (figure 9). Furthermore, given the availability of Hi-C sequencing data in HSJ-19 and its isogenic H3-K27M KO clone, the addition of this sample will provide another platform to study the association of cPRC1 increased occupancy with stronger chromatin contacts in contribution to tumorigenesis (**Figure 31**). Similarly, we will perform ChIP-seq on a pHGG histone wild-type cell line, G477, where we over-expressed H3.3-K27M or H3.3-K27R (control).

7.2 RING1B, CBX2 and H2AK119ub chromatin immune-precipitation followed by high-throughput sequencing in non-glioma cell lines

To better endorse the association of our observations with the presence of the H3-K27M mutation, we will perform ChIP-seq of RING1B, CBX2 and H2AK119ub in non-glioma cell lines. Specifically, we will use HEK293T, a human embryonic kidney cell line from ATCC, where we introduced the lysine-to-methionine substitution in *HIST1H3B.* The introduction of the H3.1-K27M mutation in a more differentiated and non-glioma context will help better highlight the effects of the mutation on PRC1 recruitment.

7.3 RING1A/B knock-out validations

In an attempt to better characterize PRC1's contribution to tumorigenesis, we sought to knock-out RING1B by CRISPR/Cas9 editing (https://www.synthego.com/) in BT245 parental cell lines. While we generated 178 viable clones, only 10 showed homozygous exon 3 editing of *RNF2* when screened by Illumina MiSeq systems. These clones are still pending functional validation of RING1B absence by western blot and immunofluorescent staining. Upon validation, RING1B KO clones will undergo numerous cellular characterizations in comparison with unedited controls. These include proliferation, clonogenicity and senescence assays. These cells will be grown in stem cell media as well as in differentiation media for comparison. Since RING1A is expressed in our models (**Figure 33**) and RING1B KO can still maintain PRC1 assembly and H2AK119ub deposition through RING1A (51), we plan on also knocking down *RING1* in RING1B KO BT245 cell lines. Conditional knock-down of RING1A by small-hairpin RNA interference (shRNA) in BT245 RING1B KO clones will provide models where PRC1 assembly and activity is completely obliterated. Since H3-K27M pHGGs exhibit large epigenetic changes, depleting PRC1 will drive further drastic epigenetic losses and should be approached with inducible constructs. These models will allow us to better characterize the role of PRC1 in H3-K27M pHGG tumorigenesis. If stable, it would also be interesting to perform ChIP-seq on PRC2 components in these models and obtain an understanding of PRC2-unique associations in relation to tumorigenesis.

7.4 Generation of I53A/S catalytically ineffective PRC1 models

Upon the generation of PRC1-null H3-K27M pHGG models, we plan on introducing I53A/S catalytic RING1B mutants. Lentiviruses with I53A/S RING1B plasmid constructs are currently being generated and are pending the validation of PRC1-null models. Introducing I53A/S RING1B, previously reported to form catalytically deficient PRC1 assemblies (51), will help delineate the contribution of H2AK119ub in H3-K27M pHGG tumorigenesis. As shown before, H2AK119ub remains largely unperturbed in H3-K27M pHGG (figures 2 and 3). Given the PRC1/2-interplay recruitment mechanism that relies of H2AK119ub, it would be compelling to generate models where PRC1 and PRC2 are unlinked by removal of H2AK119ub and study their epigenetic profiles. Doing so will also help address whether H2AK119ub deposition is playing an active role in maintain gene silencing events despite H3K27me3 loss. Similarly, this approach can help unravel which sites rely on PRC1/2-interplay and potentially unravel therapeutic vulnerabilities in H3-K27M pHGGs.

7.5 Uncoupling PRC1 from PRC2 in H3-K27M pHGGs

Upon the observation of increased PRC1/2 coupling in H3-K27M pHGGs, it would be compelling to define its role and contribution to oncogenesis. As shown in figures 10, 11 and 17, we hypothesize that H3K27me3 reduced spread is driving cPRC1 increased occupancy at least through CBX2. Pharmacological inhibition of CBX proteins (UNC3866) can help uncouple cPRC1 from PRC2 in H3-K27M pHGG contexts and address parts of the aforementioned hypothesis (53). It would also be compelling to describe the impact of CBX inhibition on cellular survival and proliferation, both alone and in conjunction with other epigenetic probes (EZH2i and HDACi). Alternatively, CBX2 depletion in H3-K27M and WT pHGG cell lines could also be an uncoupling approach to explore as highlighted above.

7.6 KDM2B ChIP-seq

As shown in **Figure 16**, RING1B shows significant enrichment at promoters with CGIs. Given the documented recruitment of ncPRC1.1 to unmethylated CGIs through KDM2B binding (16, 21, 28), it would be compelling to map KDM2B in H3-K27M HGGs. Similarly, it would be interesting to analyze the overlap of KDM2B with PRC1-occupied H3K27me3-depleted CGI promoters and compare it across histone conditions. KDM2B ChIP-seq would provide a clear insight into a subset of ncPRC1 whose distribution we would then compare with cPRC1 (CBX2) in H3-K27M and isogenic H3-K27M KO pHGG cell lines. Combined KDM2B and RING1B enrichments could help justify H2AK119ub unperturbed deposition across the genome of H3-K27M pHGGs and highlight sites where PRC1 is recruited independently of H3K27me3.

Reference

1. Coleman, C., Stoller, S., Grotzer, M. et al. Pediatric hemispheric high-grade glioma: targeting the future. Cancer Metastasis Rev 39, 245–260 (2020). https://doi-org.proxy3.library.mcgill.ca/10.1007/s10555-020-09850-5

2. Lombardi, M. Y. and M. Assem (2017). Glioblastoma Genomics: A Very Complicated Story. Glioblastoma. S. De Vleeschouwer. Brisbane (AU).

3. Thakkar, J. P., et al. (2014). "Epidemiologic and molecular prognostic review of glioblastoma." Cancer Epidemiol Biomarkers Prev 23(10): 1985-1996.

4. Wesseling, P., Capper, D.. (2018) Neuropathology and Applied Neurobiology 44, 139– 150 WHO 2016 Classification of gliomas

5. Schwartzentruber, J., Korshunov, A., Liu, X. et al. Driver mutations in histone H3.3 and chromatin remodelling genes in paediatric glioblastoma. Nature 482, 226–231 (2012). https://doi-org.proxy3.library.mcgill.ca/10.1038/nature10833 6. Glioma epigenetics: From subclassification to novel treatment options.

7. Solomon, D. A., et al. (2016). "Diffuse Midline Gliomas with Histone H3-K27M Mutation: A Series of 47 Cases Assessing the Spectrum of Morphologic Variation and Associated Genetic Alterations." Brain Pathol 26(5): 569-580.

8. Kallappagoudar, S., et al. (2015). "Histone H3 mutations--a special role for H3.3 in tumorigenesis?" Chromosoma 124(2): 177-189

9. Khuong-Quang, D. A., et al. (2012). "K27M mutation in histone H3.3 defines clinically and biologically distinct subgroups of pediatric diffuse intrinsic pontine gliomas." Acta Neuropathol 124(3): 439-447

10. Schuettengruber B, Bourbon HM, Di Croce L, Cavalli G. Genome Regulation by Polycomb and Trithorax: 70 Years and Counting. Cell. 2017;171(1):34-57.

11. Yelton CJ, Ray SK. Histone deacetylase enzymes and selective histone deacetylase inhibitors for antitumor effects and enhancement of antitumor immunity in glioblastoma. Neuroimmunol Neuroinflamm. 2018;5.

12. Harutyunyan AS, Krug B, Chen H, Papillon-Cavanagh S, Zeinieh M, De Jay N, et al. H3K27M induces defective chromatin spread of PRC2-mediated repressive H3K27me2/me3 and is essential for glioma tumorigenesis. Nat Commun. 2019;10(1):1262.

13. Krug B, De Jay N, Harutyunyan AS, Deshmukh S, Marchione DM, Guilhamon P, et al. Pervasive H3K27 Acetylation Leads to ERV Expression and a Therapeutic Vulnerability in H3K27M Gliomas. Cancer Cell. 2019;35(5):782-97 e8.

14. Gulati N, Beguelin W, Giulino-Roth L. Enhancer of zeste homolog 2 (EZH2) inhibitors. Leuk Lymphoma. 2018;59(7):1574-85.

15. Bajusz, I.; Kovács, G.; Pirity, M.K. From Flies to Mice: The Emerging Role of Non-Canonical PRC1 Members in Mammalian Development. Epigenomes 2018, 2, 4.

16. Farcas AM, Blackledge NP, Sudbery I, Long HK, McGouran JF, Rose NR, et al. KDM2B links the Polycomb Repressive Complex 1 (PRC1) to recognition of CpG islands. Elife. 2012;1:e00205.

17. Silveira AB, Kasper LH, Fan Y, Jin H, Wu G, Shaw TI, et al. H3.3 K27M depletion increases differentiation and extends latency of diffuse intrinsic pontine glioma growth in vivo. Acta Neuropathol. 2019;137(4):637-55.

18. He J, Shen L, Wan M, Taranova O, Wu H, Zhang Y. Kdm2b maintains murine embryonic stem cell status by recruiting PRC1 complex to CpG islands of developmental genes. Nat Cell Biol. 2013;15(4):373-84.

19. Deng H, Guan X, Gong L, Zeng J, Zhang H, Chen MY, et al. CBX6 is negatively regulated by EZH2 and plays a potential tumor suppressor role in breast cancer. Sci Rep. 2019;9(1):197.

20. Santanach A, Blanco E, Jiang H, Molloy KR, Sanso M, LaCava J, et al. The Polycomb group protein CBX6 is an essential regulator of embryonic stem cell identity. Nat Commun. 2017;8(1):1235.

21. Cohen I, Bar C, Ezhkova E. Activity of PRC1 and Histone H2AK119 Monoubiquitination: Revising Popular Misconceptions. Bioessays. 2020;42(5):e1900192.

22. Cohen I, Zhao D, Bar C, Valdes VJ, Dauber-Decker KL, Nguyen MB, et al. PRC1 Fine-tunes Gene Repression and Activation to Safeguard Skin Development and Stem Cell Specification. Cell Stem Cell. 2018;22(5):726-39 e7.

23. Desai D, Pethe P. Polycomb repressive complex 1: Regulators of neurogenesis from embryonic to adult stage. J Cell Physiol. 2020;235(5):4031-45.

24. Illingworth RS. Chromatin folding and nuclear architecture: PRC1 function in 3D. Curr Opin Genet Dev. 2019;55:82-90.

25. Cruz-Molina S, Respuela P, Tebartz C, Kolovos P, Nikolic M, Fueyo R, et al. PRC2 Facilitates the Regulatory Topology Required for Poised Enhancer Function during Pluripotent Stem Cell Differentiation. Cell Stem Cell. 2017;20(5):689-705 e9.

26. Chan HL, Morey L. Emerging Roles for Polycomb-Group Proteins in Stem Cells and Cancer. Trends Biochem Sci. 2019;44(8):688-700.

27. Koppens M, van Lohuizen M. Context-dependent actions of Polycomb repressors in cancer. Oncogene. 2016;35(11):1341-52.

28. Zepeda-Martinez JA, Pribitzer C, Wang J, Bsteh D, Golumbeanu S, Zhao Q, et al. Parallel PRC2/cPRC1 and vPRC1 pathways silence lineage-specific genes and maintain self-renewal in mouse embryonic stem cells. Sci Adv. 2020;6(14):eaax5692.

29. Brockdorff N. Polycomb complexes in X chromosome inactivation. Philos Trans R Soc Lond B Biol Sci. 2017;372(1733).

30. Moussa HF, Bsteh D, Yelagandula R, Pribitzer C, Stecher K, Bartalska K, et al. Canonical PRC1 controls sequence-independent propagation of Polycomb-mediated gene silencing. Nat Commun. 2019;10(1):1931.

31. Marsh DJ, Dickson KA. Writing Histone Monoubiquitination in Human Malignancy-The Role of RING Finger E3 Ubiquitin Ligases. Genes (Basel). 2019;10(1).

32. Bender S, Tang Y, Lindroth AM, Hovestadt V, Jones DT, Kool M, et al. Reduced H3K27me3 and DNA hypomethylation are major drivers of gene expression in K27M mutant pediatric high-grade gliomas. Cancer Cell. 2013;24(5):660-72.

33. Wang Z, Gearhart MD, Lee YW, Kumar I, Ramazanov B, Zhang Y, et al. A Non-canonical BCOR-PRC1.1 Complex Represses Differentiation Programs in Human ESCs. Cell Stem Cell. 2018;22(2):235-51 e9.

34. Williams MJ, Singleton WG, Lowis SP, Malik K, Kurian KM. Therapeutic Targeting of Histone Modifications in Adult and Pediatric High-Grade Glioma. Front Oncol. 2017;7:45.

35. Huseyin MK, Klose RJ. Live-cell single particle tracking of PRC1 reveals a highly dynamic system with low target site occupancy. bioRxiv. 2020:2020.04.25.061358. (***in press***).

36. Tsuboi M, Kishi Y, Yokozeki W, Koseki H, Hirabayashi Y, Gotoh Y. Ubiquitination-Independent Repression of PRC1 Targets during Neuronal Fate Restriction in the Developing Mouse Neocortex. Dev Cell. 2018;47(6):758-72 e5.

37. Larouche V, Toupin AK, Lalonde B, Simonyan D, Jabado N, Perreault S. Incidence trends in pediatric central nervous system tumors in Canada: a 15 years report from Cancer and Young People in Canada (CYP-C) registry. Neurooncol Adv. 2020;2(1):vdaa012.

38. Braunstein S, Raleigh D, Bindra R, Mueller S, Haas-Kogan D. Pediatric high-grade glioma: current molecular landscape and therapeutic approaches. J Neurooncol. 2017;134(3):541-9.

39. I. Cohen, D. Zhao, C. Bar, V. J. Valdes, K. L. Dauber-Decker, M. B. Nguyen, M. Nakayama, M. Rendl, W. A. Bickmore, H. Koseki, D. Zheng, E. Ezhkova, Cell Stem Cell 2018, 22, 726.

40. Lavarone E, Barbieri CM, Pasini D. Dissecting the role of H3K27 acetylation and methylation in PRC2 mediated control of cellular identity. Nat Commun. 2019;10(1):1679.

41. Kaustov L, Ouyang H, Amaya M, Lemak A, Nady N, Duan S, et al. Recognition and specificity determinants of the human cbx chromodomains. J Biol Chem. 2011;286(1):521-9.

42. Jangal M, Lebeau B, Witcher M. Beyond EZH2: is the polycomb protein CBX2 an emerging target for anti-cancer therapy? Expert Opin Ther Targets. 2019;23(7):565-78.

43. Healy E, Mucha M, Glancy E, Fitzpatrick DJ, Conway E, Neikes HK, et al. PRC2.1 and PRC2.2 Synergize to Coordinate H3K27 Trimethylation. Mol Cell. 2019;76(3):437-52 e6.

44. Lee HG, Kahn TG, Simcox A, Schwartz YB, Pirrotta V. Genome-wide activities of Polycomb complexes control pervasive transcription. Genome Res. 2015;25(8):1170-81.

45. Pasini D, Malatesta M, Jung HR, Walfridsson J, Willer A, Olsson L, et al. Characterization of an antagonistic switch between histone H3 lysine 27 methylation and acetylation in the transcriptional regulation of Polycomb group target genes. Nucleic Acids Res. 2010;38(15):4958-69.

46. Li M, Zhang S, Zhao W, Hou C, Ma X, Li X, et al. RYBP modulates stability and function of Ring1B through targeting UBE3A. FASEB J. 2019;33(1):683-95.

47. Loubiere V, Papadopoulos GL, Szabo Q, Martinez AM, Cavalli G. Widespread activation of developmental gene expression characterized by PRC1-dependent chromatin looping. Sci Adv. 2020;6(2):eaax4001.

48. Koppens M, van Lohuizen M. Context-dependent actions of Polycomb repressors in cancer. Oncogene. 2016;35(11):1341-52.

49. Chan HL, Beckedorff F, Zhang Y, Garcia-Huidobro J, Jiang H, Colaprico A, et al. Polycomb complexes associate with enhancers and promote oncogenic transcriptional programs in cancer through multiple mechanisms. Nature Communications. 2018;9(1):3377.

50. King HW, Fursova NA, Blackledge NP, Klose RJ. Polycomb repressive complex 1 shapes the nucleosome landscape but not accessibility at target genes. Genome Res. 2018;28(10):1494-507.

51. Tamburri S, Lavarone E, Fernández-Pérez D, Conway E, Zanotti M, Manganaro D, et al. Histone H2AK119 Mono-Ubiquitination Is Essential for Polycomb-Mediated Transcriptional Repression. Mol Cell. 2020;77(4):840-56.e5.

52. Kundu S, Ji F, Sunwoo H, Jain G, Lee JT, Sadreyev RI, et al. Polycomb Repressive Complex 1 Generates Discrete Compacted Domains that Change during Differentiation. Mol Cell. 2017;65(3):432-46.e5.

53. Stuckey JI, Dickson BM, Cheng N, Liu Y, Norris JL, Cholensky SH, et al. A cellular chemical probe targeting the chromodomains of Polycomb repressive complex 1. Nat Chem Biol. 2016;12(3):180-7.

54. Chen EY, Tan CM, Kou Y, Duan Q, Wang Z, Meirelles GV, Clark NR, Ma'ayan A. Enrichr: interactive and collaborative HTML5 gene list enrichment analysis tool. BMC Bioinformatics. 2013;128(14). (enrichr)

55. F.A. Ran, P.D. Hsu, J. Wright, V. Agarwala, D.A. Scott, F. Zhang. Genome engineering using the CRISPR-Cas9 system. Nat. Protoc., 8 (2013), pp. 2281-2308

56. Li H, Durbin R. Fast and accurate short read alignment with Burrows-Wheeler transform. Bioinformatics. 2009;25(14):1754-60.

57. Younesy H, Nielsen CB, Lorincz MC, Jones SJ, Karimi MM, Moller T. ChAsE: chromatin analysis and exploration tool. Bioinformatics. 2016;32(21):3324-6.

58. Thorvaldsdottir H, Robinson JT, Mesirov JP. Integrative Genomics Viewer (IGV): high-performance genomics data visualization and exploration. Brief Bioinform. 2013;14(2):178-92.

59. Feng, J., Liu, T., Qin, B., Zhang, Y. & Liu, X. S. Identifying ChIP-seq enrichment using MACS. Nat. Protoc. 7, 1728–1740 (2012).

60. Chen EY, Tan CM, Kou Y, Duan Q, Wang Z, Meirelles GV, et al. Enrichr: interactive and collaborative HTML5 gene list enrichment analysis tool. BMC Bioinformatics. 2013;14:128.

61. Kuleshov MV, Jones MR, Rouillard AD, Fernandez NF, Duan Q, Wang Z, Koplev S, Jenkins SL, Jagodnik KM, Lachmann A, McDermott MG, Monteiro CD, Gundersen GW, Ma'ayan A. Enrichr: a comprehensive gene set enrichment analysis web server 2016 update. Nucleic Acids Research. 2016; gkw377.

62. Fursova NA, Blackledge NP, Nakayama M, Ito S, Koseki Y, Farcas AM, et al. Synergy between Variant PRC1 Complexes Defines Polycomb-Mediated Gene Repression. Mol Cell. 2019;74(5):1020-36.e8.

63. Karsy M, Guan J, Cohen AL, Jensen RL, Colman H. New Molecular Considerations for Glioma: IDH, ATRX, BRAF, TERT, H3 K27M. Curr Neurol Neurosci Rep. 2017;17(2):19.

64. Buttarelli FR, Massimino M, Antonelli M, Lauriola L, Nozza P, Donofrio V, et al. Evaluation status and prognostic significance of O6-methylguanine-DNA methyltransferase

(MGMT) promoter methylation in pediatric high grade gliomas. Childs Nerv Syst. 2010;26(8):1051-6.

65. Chan KM, Han J, Fang D, Gan H, Zhang Z. A lesson learned from the H3.3K27M mutation found in pediatric glioma: a new approach to the study of the function of histone modifications in vivo? Cell Cycle. 2013;12(16):2546-52.

66. Wang Z, Gearhart MD, Lee YW, Kumar I, Ramazanov B, Zhang Y, et al. A Non-canonical BCOR-PRC1.1 Complex Represses Differentiation Programs in Human ESCs. Cell Stem Cell. 2018;22(2):235-51 e9.

67. Hojfeldt JW, Laugesen A, Willumsen BM, Damhofer H, Hedehus L, Tvardovskiy A, et al. Accurate H3K27 methylation can be established de novo by SUZ12-directed PRC2. Nat Struct Mol Biol. 2018;25(3):225-32.

68. Li G, Warden C, Zou Z, Neman J, Krueger JS, Jain A, et al. Altered expression of polycomb group genes in glioblastoma multiforme. PLoS One. 2013;8(11):e80970.

69. Pathak P, Jha P, Purkait S, Sharma V, Suri V, Sharma MC, et al. Altered global histone-trimethylation code and H3F3A-ATRX mutation in pediatric GBM. J Neurooncol. 2015;121(3):489-97.

70. Cai L, Rothbart SB, Lu R, Xu B, Chen WY, Tripathy A, et al. An H3K36 methylation-engaging Tudor motif of polycomb-like proteins mediates PRC2 complex targeting. Mol Cell. 2013;49(3):571-82.

71. Hetey S, Boros-Olah B, Kuik-Rozsa T, Li Q, Karanyi Z, Szabo Z, et al. Biophysical characterization of histone H3.3 K27M point mutation. Biochem Biophys Res Commun. 2017;490(3):868-75.

72. Fang J, Huang Y, Mao G, Yang S, Rennert G, Gu L, et al. Cancer-driving H3G34V/R/D mutations block H3K36 methylation and H3K36me3-MutSalpha interaction. Proc Natl Acad Sci U S A. 2018;115(38):9598-603.

73. Moussa HF, Bsteh D, Yelagandula R, Pribitzer C, Stecher K, Bartalska K, et al. Canonical PRC1 controls sequence-independent propagation of Polycomb-mediated gene silencing. Nat Commun. 2019;10(1):1931.

74. Landt SG, Marinov GK, Kundaje A, Kheradpour P, Pauli F, Batzoglou S, et al. ChIP-seq guidelines and practices of the ENCODE and modENCODE consortia. Genome Res. 2012;22(9):1813-31.

75. Connelly KE, Dykhuizen EC. Compositional and functional diversity of canonical PRC1 complexes in mammals. Biochim Biophys Acta Gene Regul Mech. 2017;1860(2):233-45.

76. Solomon DA, Wood MD, Tihan T, Bollen AW, Gupta N, Phillips JJ, et al. Diffuse Midline Gliomas with Histone H3-K27M Mutation: A Series of 47 Cases Assessing the Spectrum of Morphologic Variation and Associated Genetic Alterations. Brain Pathol. 2016;26(5):569-80.

77. Sein H, Varv S, Kristjuhan A. Distribution and maintenance of histone H3 lysine 36 trimethylation in transcribed locus. PLoS One. 2015;10(3):e0120200.

78. Tian B, Yang J, Brasier AR. Two-step cross-linking for analysis of protein-chromatin interactions. Methods Mol Biol. 2012;809:105-20.

79. Thakkar JP, Dolecek TA, Horbinski C, Ostrom QT, Lightner DD, Barnholtz-Sloan JS, et al. Epidemiologic and molecular prognostic review of glioblastoma. Cancer Epidemiol Biomarkers Prev. 2014;23(10):1985-96

80. Zhao W, Tong H, Huang Y, Yan Y, Teng H, Xia Y, et al. Essential Role for Polycomb Group Protein Pcgf6 in Embryonic Stem Cell Maintenance and a Noncanonical Polycomb Repressive Complex 1 (PRC1) Integrity. J Biol Chem. 2017;292(7):2773-84.

81. Shechter D, Dormann HL, Allis CD, Hake SB. Extraction, purification and analysis of histones. Nat Protoc. 2007;2(6):1445-57.

82. Scelfo A, Fernandez-Perez D, Tamburri S, Zanotti M, Lavarone E, Soldi M, et al. Functional Landscape of PCGF Proteins Reveals Both RING1A/B-Dependent-and RING1A/B-Independent-Specific Activities. Mol Cell. 2019;74(5):1037-52 e7.

83. Buczkowicz P, Hoeman C, Rakopoulos P, Pajovic S, Letourneau L, Dzamba M, et al. Genomic analysis of diffuse intrinsic pontine gliomas identifies three molecular subgroups and recurrent activating ACVR1 mutations. Nat Genet. 2014;46(5):451-6.

84. Fang D, Gan H, Cheng L, Lee JH, Zhou H, Sarkaria JN, et al. H3.3K27M mutant proteins reprogram epigenome by sequestering the PRC2 complex to poised enhancers. Elife. 2018;7.

85. Kalb R, Latwiel S, Baymaz HI, Jansen PW, Muller CW, Vermeulen M, et al. Histone H2A monoubiquitination promotes histone H3 methylation in Polycomb repression. Nat Struct Mol Biol. 2014;21(6):569-71.

86. Shi L, Shi J, Shi X, Li W, Wen H. Histone H3.3 G34 Mutations Alter Histone H3K36 and H3K27 Methylation In Cis. J Mol Biol. 2018;430(11):1562-5.

87. Lu C, Jain SU, Hoelper D, Bechet D, Molden RC, Ran L, et al. Histone H3K36 mutations promote sarcomagenesis through altered histone methylation landscape. Science. 2016;352(6287):844-9.

88. Berlandi J, Chaouch A, De Jay N, Tegeder I, Thiel K, Shirinian M, et al. Identification of genes functionally involved in the detrimental effects of mutant histone H3.3-K27M in Drosophila melanogaster. Neuro Oncol. 2019;21(5):628-39.

89. Lu C, Ward PS, Kapoor GS, Rohle D, Turcan S, Abdel-Wahab O, et al. IDH mutation impairs histone demethylation and results in a block to cell differentiation. Nature. 2012;483(7390):474-8.

90. Voon HPJ, Udugama M, Lin W, Hii L, Law RHP, Steer DL, et al. Inhibition of a K9/K36 demethylase by an H3.3 point mutation found in paediatric glioblastoma. Nat Commun. 2018;9(1):3142.

91. Mackay A, Burford A, Carvalho D, Izquierdo E, Fazal-Salom J, Taylor KR, et al. Integrated Molecular Meta-Analysis of 1,000 Pediatric High-Grade and Diffuse Intrinsic Pontine Glioma. Cancer Cell. 2017;32(4):520-37 e5.

92. Kahn TG, Dorafshan E, Schultheis D, Zare A, Stenberg P, Reim I, et al. Interdependence of PRC1 and PRC2 for recruitment to Polycomb Response Elements. Nucleic Acids Res. 2016;44(21):10132-49.

93. Kurt IC, Sur I, Kaya E, Cingoz A, Kazancioglu S, Kahya Z, et al. KDM2B, an H3K36-specific demethylase, regulates apoptotic response of GBM cells to TRAIL. Cell Death Dis. 2017;8(6):e2897.

94. Yan Y, Zhao W, Huang Y, Tong H, Xia Y, Jiang Q, et al. Loss of Polycomb Group Protein Pcgf1 Severely Compromises Proper Differentiation of Embryonic Stem Cells. Sci Rep. 2017;7:46276.

95. Cheutin T, Cavalli G. Loss of PRC1 induces higher-order opening of Hox loci independently of transcription during Drosophila embryogenesis. Nat Commun. 2018;9(1):3898.

96. Fontebasso AM, Schwartzentruber J, Khuong-Quang DA, Liu XY, Sturm D, Korshunov A, et al. Mutations in SETD2 and genes affecting histone H3K36 methylation target hemispheric high-grade gliomas. Acta Neuropathol. 2013;125(5):659-69.

97. Coleman C, Stoller S, Grotzer M, Stucklin AG, Nazarian J, Mueller S. Pediatric hemispheric high-grade glioma: targeting the future. Cancer Metastasis Rev. 2020.

98. Chan HL, Beckedorff F, Zhang Y, Garcia-Huidobro J, Jiang H, Colaprico A, et al. Polycomb complexes associate with enhancers and promote oncogenic transcriptional programs in cancer through multiple mechanisms. Nat Commun. 2018;9(1):3377.

99. Zhao W, Huang Y, Zhang J, Liu M, Ji H, Wang C, et al. Polycomb group RING finger proteins 3/5 activate transcription via an interaction with the pluripotency factor Tex10 in embryonic stem cells. J Biol Chem. 2017;292(52):21527-37.

100. Li H, Liefke R, Jiang J, Kurland JV, Tian W, Deng P, et al. Polycomb-like proteins link the PRC2 complex to CpG islands. Nature. 2017;549(7671):287-91.

101. Nikfarjam L, Farzaneh P. Prevention and detection of Mycoplasma contamination in cell culture. Cell J. 2012;13(4):203-12.

102. Xu G, Jaffrey SR. Proteomic identification of protein ubiquitination events. Biotechnol Genet Eng Rev. 2013;29:73-109.

103. Taylor KR, Mackay A, Truffaux N, Butterfield Y, Morozova O, Philippe C, et al. Recurrent activating ACVR1 mutations in diffuse intrinsic pontine glioma. Nat Genet. 2014;46(5):457-61.

104. Bender S, Tang Y, Lindroth AM, Hovestadt V, Jones DT, Kool M, et al. Reduced H3K27me3 and DNA hypomethylation are major drivers of gene expression in K27M mutant pediatric high-grade gliomas. Cancer Cell. 2013;24(5):660-72.

105. Cao R, Tsukada Y, Zhang Y. Role of Bmi-1 and Ring1A in H2A ubiquitylation and Hox gene silencing. Mol Cell. 2005;20(6):845-54.

106. eng L, Wang L, Zhang Y, Dong A, Shen WH, Huang Y. Structural Analysis of the Arabidopsis AL2-PAL and PRC1 Complex Provides Mechanistic Insight into Active-to-Repressive Chromatin State Switch. J Mol Biol. 2018;430(21):4245-59.

107. Szenker E, Ray-Gallet D, Almouzni G. The double face of the histone variant H3.3. Cell Res. 2011;21(3):421-34.

108. Margueron R, Reinberg D. The Polycomb complex PRC2 and its mark in life. Nature. 2011;469(7330):343-9.

109. Lim J, Park JH, Baude A, Fellenberg J, Zustin J, Haller F, et al. Transcriptome and protein interaction profiling in cancer cells with mutations in histone H3.3. Sci Data. 2018;5:180283.

110. Wagner EJ, Carpenter PB. Understanding the language of Lys36 methylation at histone H3. Nat Rev Mol Cell Biol. 2012;13(2):115-26.

111. Furey TS. ChIP-seq and beyond: new and improved methodologies to detect and characterize protein-DNA interactions. Nat Rev Genet. 2012;13(12):840-52.

112. R Core Team (2014). R: A language and environment for statistical computing. R Foundation for Statistical Computing, Vienna, Austria. URL http://www.R-project.org/

113. Wickham, H. (2009) *ggplot2: elegant graphics for data analysis*. Springer New York.

114. Hartigan, J. A. and Wong, M. A. (1979). Algorithm AS 136: A K-means clustering algorithm. *Applied Statistics*, **28**, 100--108. 10.2307/2346830

115. Fontebasso AM, Schwartzentruber J, Khuong-Quang DA, Liu XY, Sturm D, Korshunov A, et al. Mutations in SETD2 and genes affecting histone H3K36 methylation target hemispheric high-grade gliomas. Acta Neuropathol. 2013;125(5):659-69.

116. Nayak L, Reardon DA. High-grade Gliomas. CONTINUUM: Lifelong Learning in Neurology. 2017;23(6):1548-63.

117. Stupp R, Mason WP, van den Bent MJ, Weller M, Fisher B, Taphoorn MJ, et al. Radiotherapy plus concomitant and adjuvant temozolomide for glioblastoma. N Engl J Med. 2005;352(10):987-96.

118. Vitanza NA, Monje M. Diffuse Intrinsic Pontine Glioma: From Diagnosis to Next-Generation Clinical Trials. Curr Treat Options Neurol. 2019;21(8):37.

Appendix

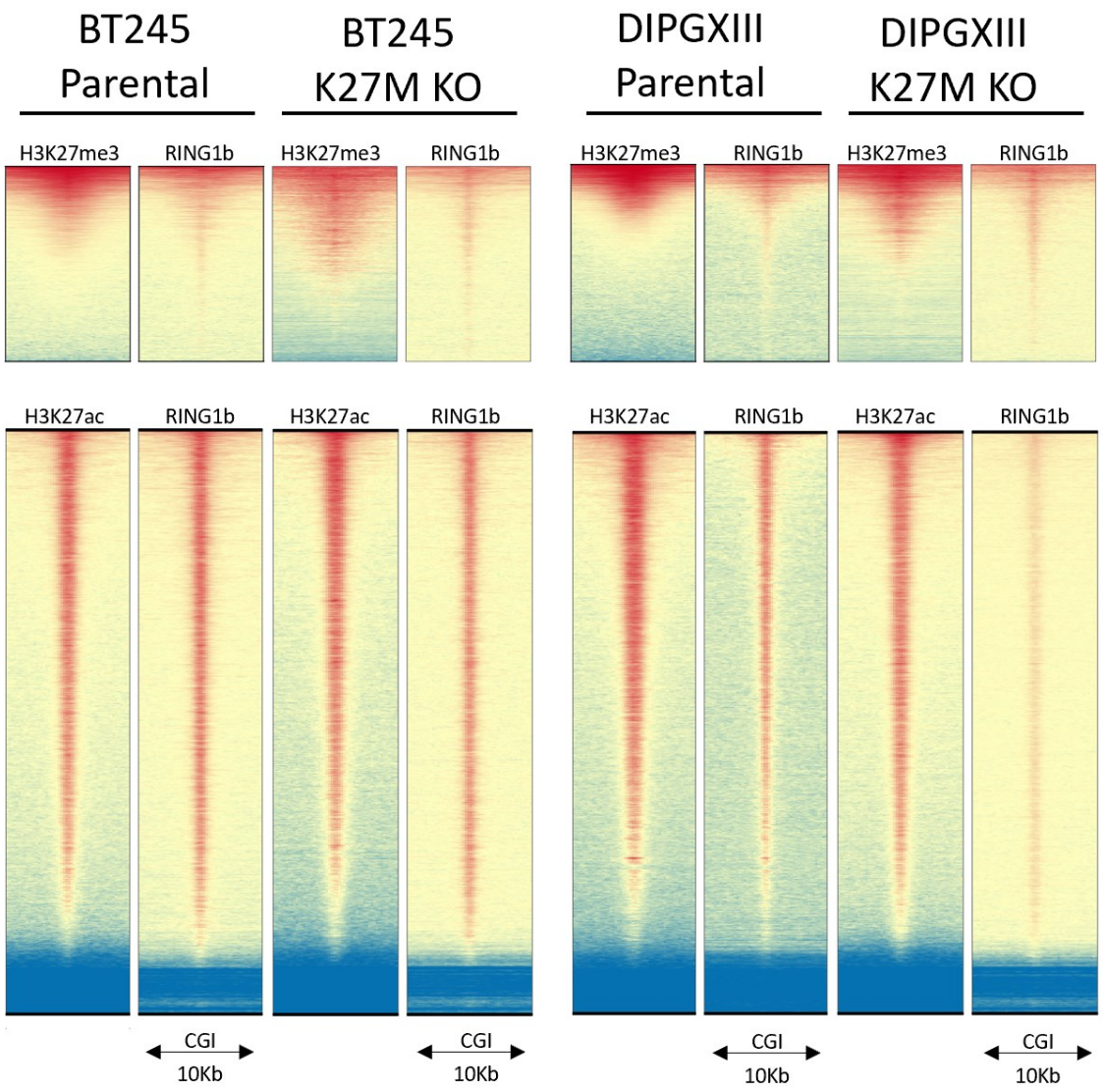

Figure 26. Stacked heatmap of RING1B, H3K27me3 and H3K27ac ChIP-seq signals on CGIs.

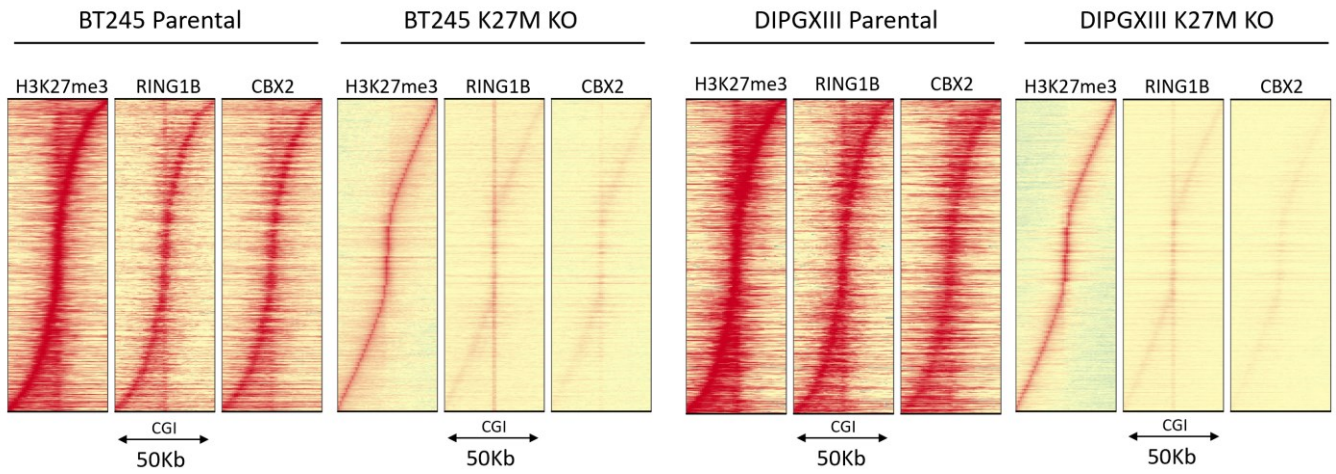

Figure 27.Stacked heatmap of H3K27me3, RING1B and CBX2 ChIP-seq signal on CGIs sorted by peak location.

Index	Name	P-value	Adjusted p-value	Odds Ratio	Combined score
1	KDM2B 26808549 Chip-Seq HPB-ALL Human	6.760e-15	4.360e-12	1.78	58.08
2	KDM2B 26808549 Chip-Seq SUP-B15 Human	1.147e-13	3.700e-11	1.74	51.85
3	KDM2B 26808549 Chip-Seq DND41 Human	1.147e-13	2.467e-11	1.74	51.85
4	MYC 22102868 ChIP-Seq BL Human	3.867e-10	6.236e-8	2.06	44.60
5	NUCKS1 24931609 ChIP-Seq HEPATOCYTES Mouse	4.031e-9	4.333e-7	2.18	42.08
6	DACH1 20351289 ChIP-Seq MDA-MB-231 Human	3.246e-9	4.187e-7	1.64	32.00
7	ELK3 25401928 ChIP-Seq HUVEC Human	5.032e-9	4.637e-7	1.57	30.00
8	KDM2B 26808549 Chip-Seq JURKAT Human	5.032e-9	4.057e-7	1.57	30.00
9	KDM2B 26808549 Chip-Seq SIL-ALL Human	2.629e-8	0.000001696	1.54	26.88
10	FOXP1 21924763 ChIP-Seq HESCs Human	8.637e-9	6.190e-7	1.38	25.63

Figure 28. ChEA enrichment results for H3K27me3-depleted promoters in BT245 parental pHGG cell lines.

Index	Name	P-value	Adjusted p-value	Odds Ratio	Combined score
1	KDM2B 26808549 Chip-Seq SUP-B15 Human	6.522e-20	4.207e-17	2.04	90.07
2	KDM2B 26808549 Chip-Seq JURKAT Human	1.587e-19	5.118e-17	2.03	87.73
3	NUCKS1 24931609 ChIP-Seq HEPATOCYTES Mouse	3.282e-11	3.528e-9	2.52	60.78
4	KDM2B 26808549 Chip-Seq DND41 Human	7.931e-15	1.705e-12	1.87	60.68
5	KDM2B 26808549 Chip-Seq HPB-ALL Human	6.194e-12	9.988e-10	1.76	45.41
6	KDM2B 26808549 Chip-Seq K562 Human	1.243e-11	1.604e-9	1.75	43.88
7	KDM2B 26808549 Chip-Seq SIL-ALL Human	2.379e-9	1.918e-7	1.65	32.77
8	WT1 20215353 ChIP-ChIP NEPHRON PROGENITOR Mouse	1.087e-8	7.790e-7	1.69	31.05
9	ELK3 25401928 ChIP-Seq HUVEC Human	1.470e-8	9.480e-7	1.61	29.11
10	MITF 21258399 ChIP-Seq MELANOMA Human	6.264e-10	5.772e-8	1.34	28.49

Figure 29. ChEA enrichment results for H3K27me3-depleted promoters in DIPGXIII parental pHGG cell lines.

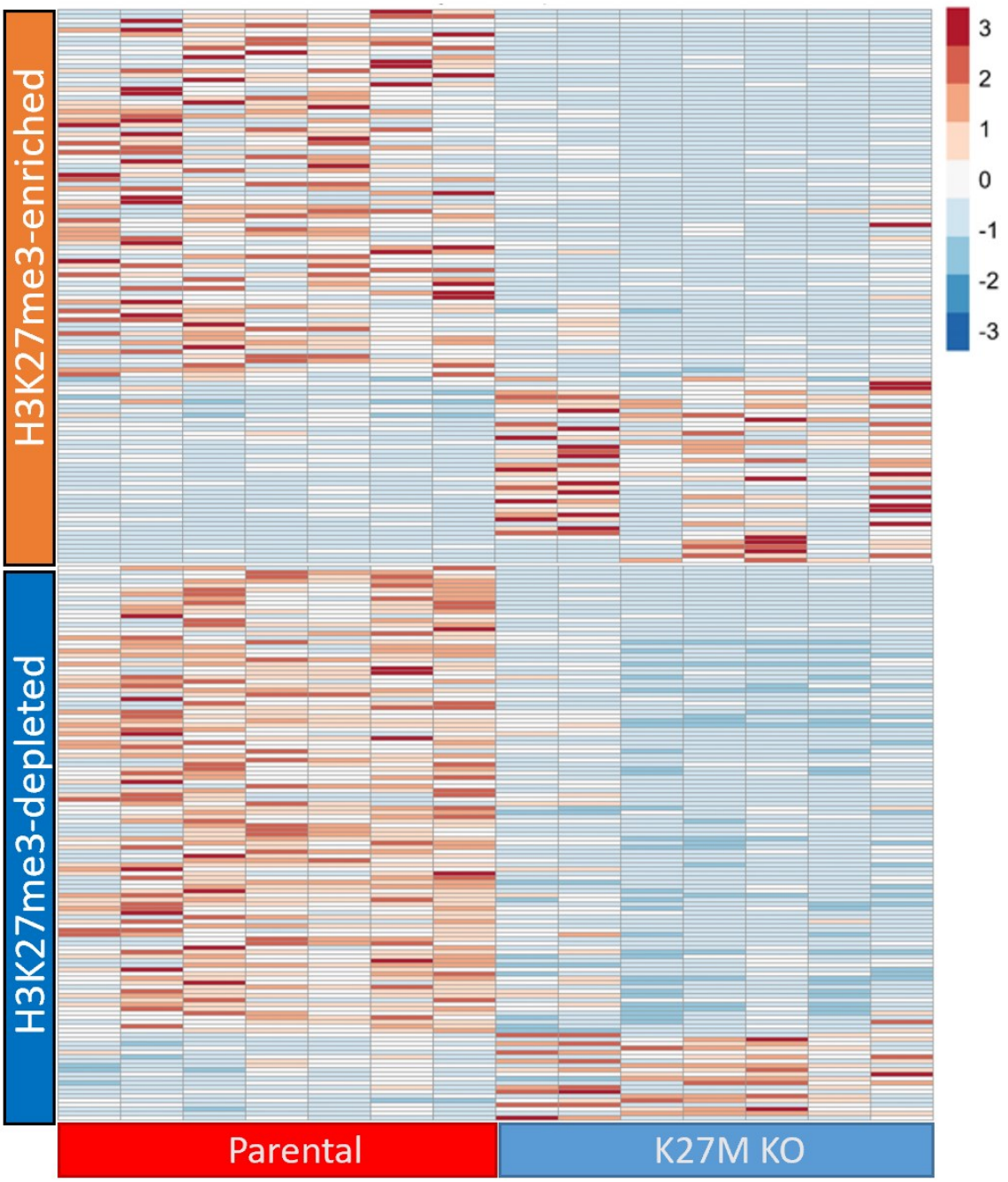

Figure 30. Heatmap of differentially expression genes at H3K27me3-enriched/depleted CGI promoters in parental (H3-K27M) when compared with isogenic K27M KO conditions.

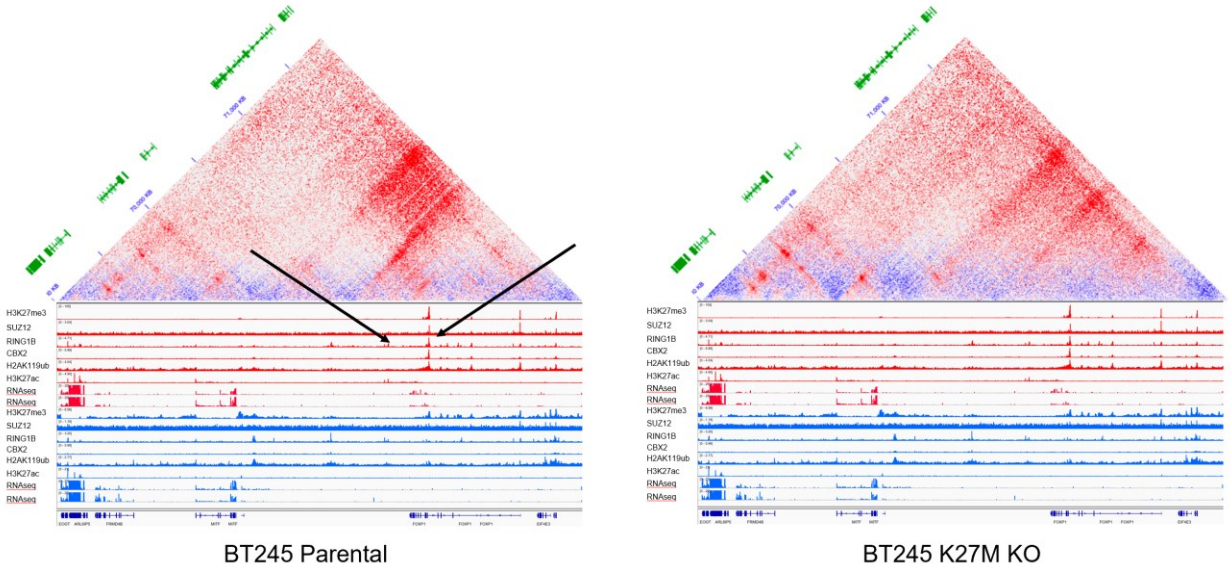

Figure 31. Comparison of HiC and ChIP-seq tracks of FOXP1 in BT245 parental (H3-K27M) and isogenic K27M KO conditions.

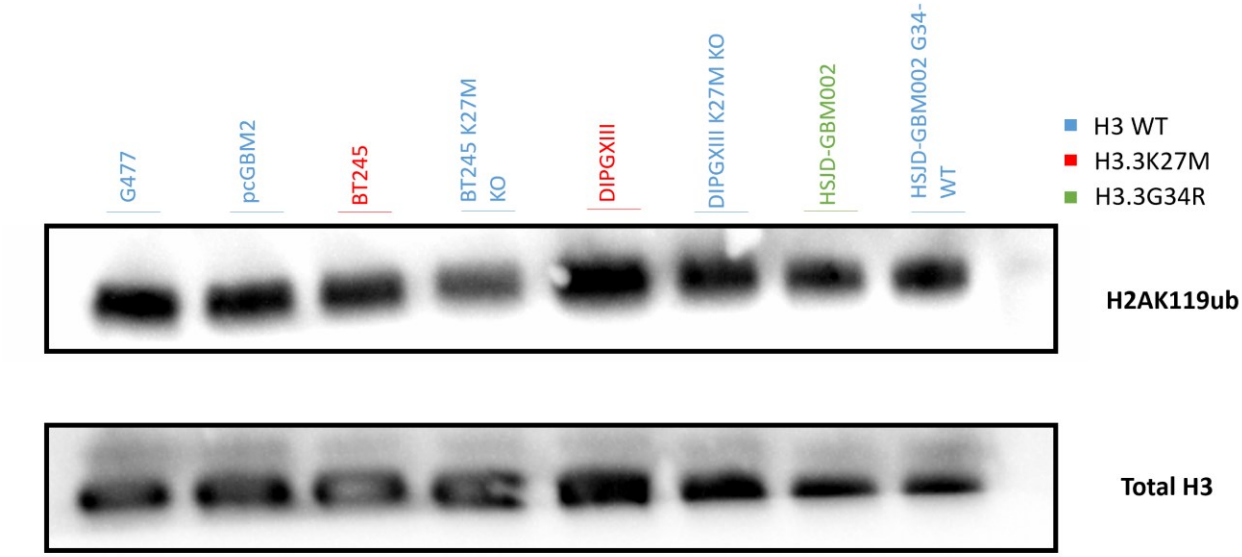

Figure 32. Western blot of H2AK119ub levels in H3-K27M, H3WT and H3G34R pHGG cell lines.

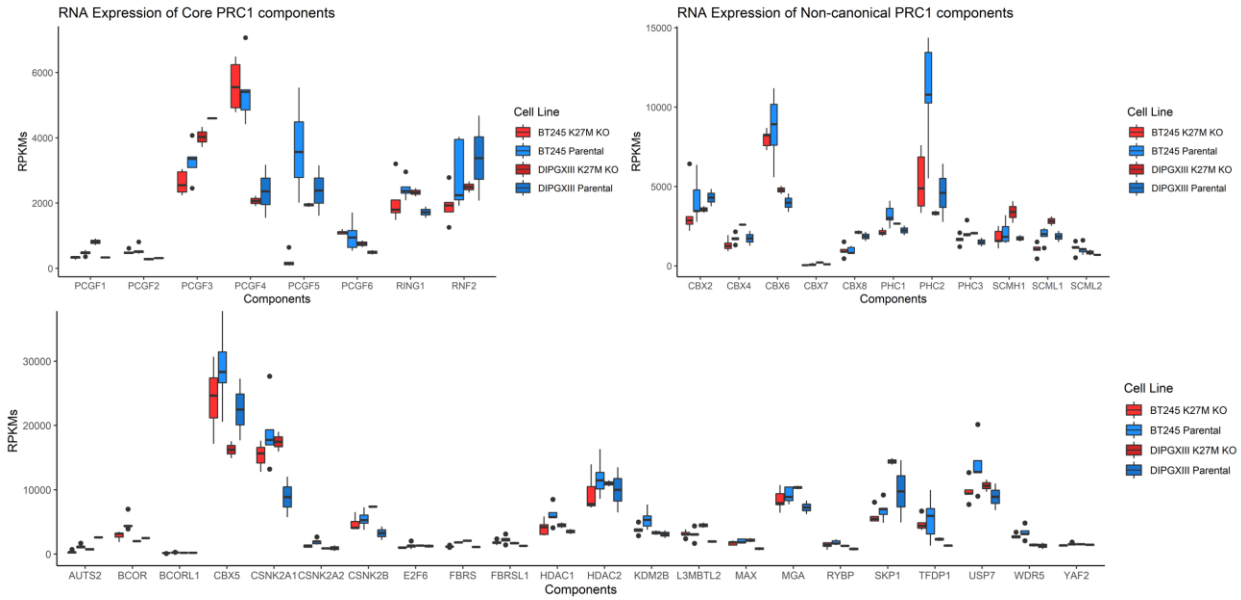

Figure 33. RPKM level comparison of all PRC1 components in BT245, DIPGXIII and their isogenic K27M KO conditions.

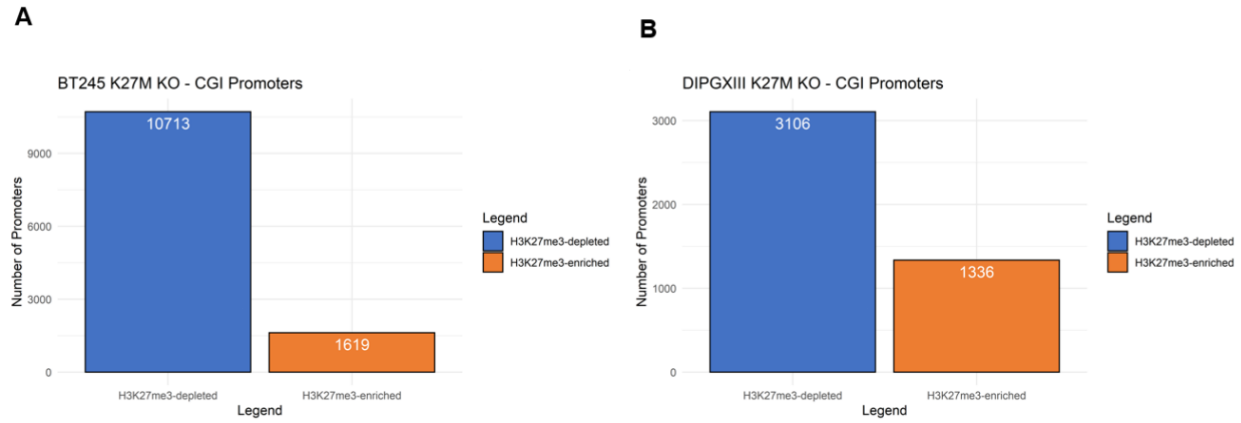

Figure 34. Barplots comparing the number of identified H3K7me3-enriched/depleted CGI promoters in BT245 and DIPGXIII K27M KO pHGG cell lines

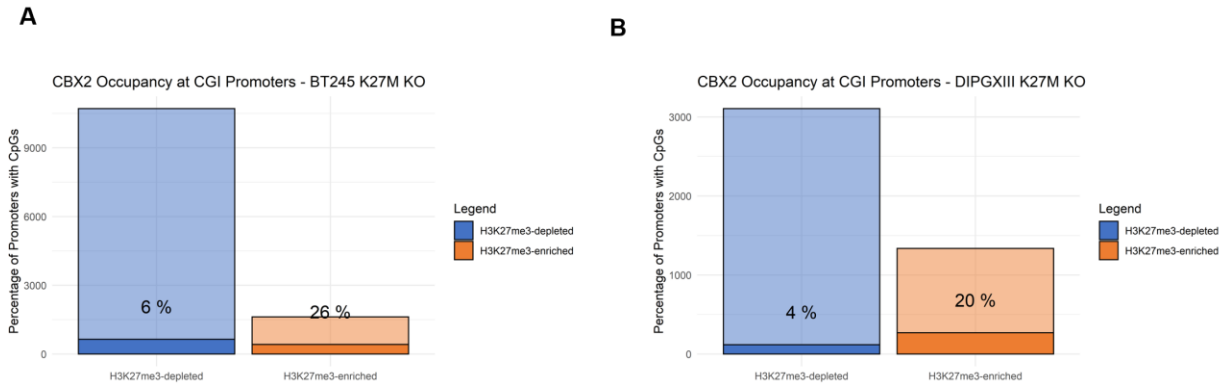

Figure 35.Comparison of CBX2 occupancy at H3K27me3-enriched and H3K27me3-depleted CGI promoters in isogenic K27M KO pHGG cell lines.

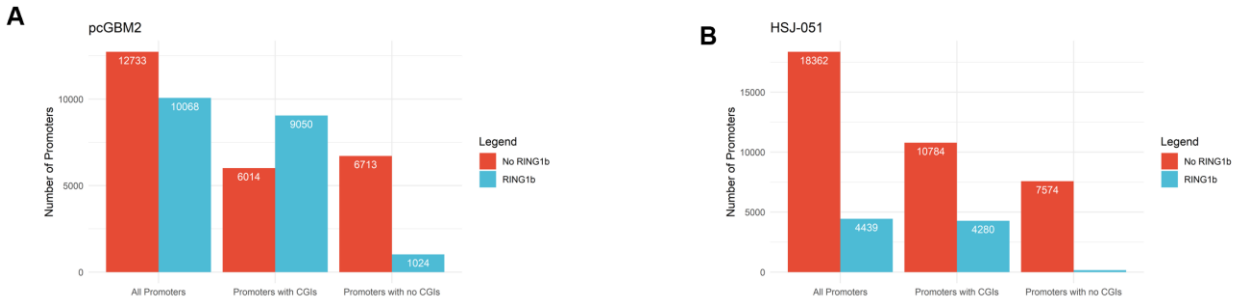

Figure 36. RING1B distribution at promoters in pcGBM2 (WT) and HSJ51 (H3-K27M) pHGG cell lines

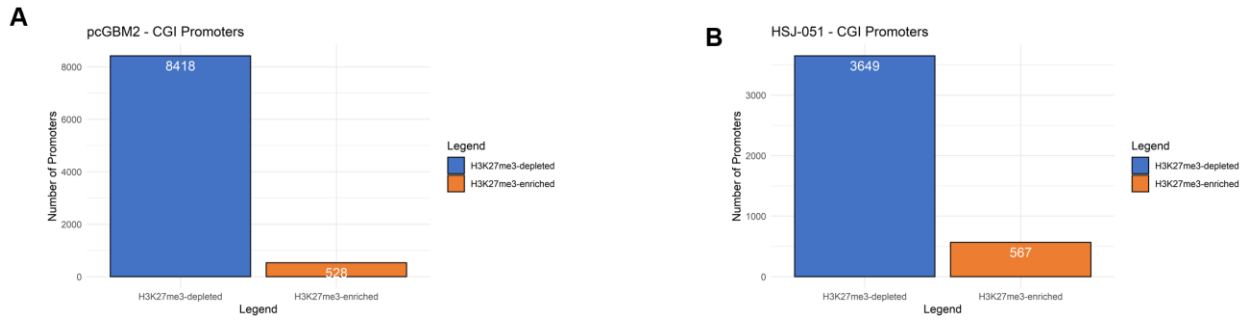

Figure 37. Comparison of H3K27me3-enriched and H3K27me3-depleted CGI promoters in pcGBM2 (WT) and HSJ51(H3-K27M) pHGG cell lines

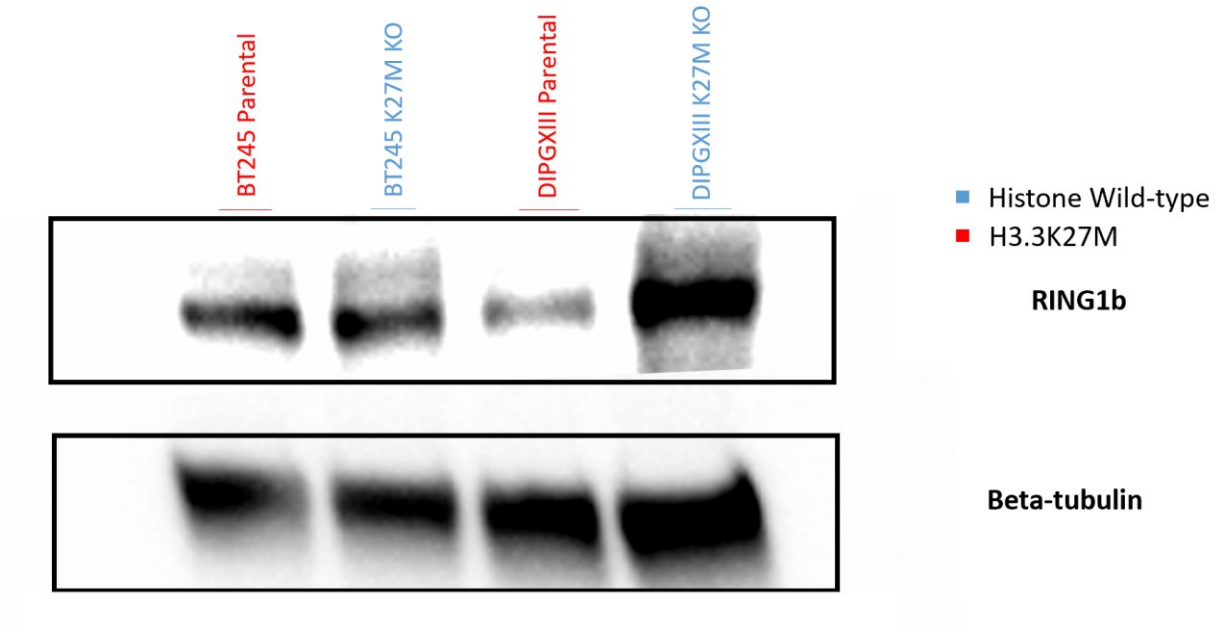

Figure 38. Western blot comparison of RING1B levels in BT245, DIPGXIII and isogenic K27M KO pHGG cell lines.

Table 3. Table showing ChIP-seq QC metrics.

Sample	ChIP	Sequencing Depth
BT245 Parental	RING1B	45.6M
DIPGXIII Parental 1	RING1B	30M
DIPGXIII K27M KO C5	RING1B	52.1M
BT245 K27M KO C2	RING1B	53.5M
DIPGXIII Parental 2	RING1B	28.9M
DIPGXIII Parental 1	H2AK119ub	97.3M
DIPGXIIII K27M KO C5	H2AK119ub	67M
BT245 Parental	H2AK119ub	68.9M
BT245 K27M KO C2	H2AK119ub	84.9M
DIPGXIII Parental 2	H2AK119ub	32.6M
BT245 Parental	H2AK119ub	28M
pcGBM2	H2AK119ub	121M
G477	H2AK119ub	72.1M
BT245 Parental	CBX2	36.5M
BT245 K27M KO C2	CBX2	26.6M
DIPGXIII Parental	CBX2	31.4M
DIPGXIII K27M KO C5	CBX2	31.9M
BT245 Parental	H3K27me3	50.9M
BT245 K27M KO C2	H3K27me3	38.4M
DIPGXIII Parental	H3K27me3	66.1M

DIPGXIII K27M KO C5	H3K27me3	50.6M
BT245 Parental	H3K27ac	38.8M
BT245 K27M KO C2	H3K27ac	30.8M
DIPGXIII Parental	H3K27ac	37.2M
DIPGXIII K27M KO C5	H3K27ac	48.1M
BT245 Parental	SUZ12	24.2M
BT245 K27M KO C4	SUZ12	71.5M
DIPGXIII Parental	SUZ12	23.1M
DIPGXIII K27M KO C5	SUZ12	56.4M
BT245 Parental	H3K27me2	73.5M
BT245 K27M KO C4	H3K27me2	82.7M
DIPGXIII Parental	H3K27me2	71.5M
DIPGXIII K27M KO C5	H3K27me2	66.2M
BT245 Parental	H3K27me1	66.5M
BT245 K27M KO C2	H3K27me1	96.4M
DIPGXIII Paental	H3K27me1	73.4M
DIPGXIII K27M KO C5	H3K27me1	70.5M
BT245 Parental	H3K36me2	31.7M
BT245 K27M KO C4	H3K36me2	47.8M
DIPGXIII Parental	H3K36me2	46.4M
DIPGXIII K27M KO C5	H3K36me2	71.2M
BT245	H3K4me3	29.2M
BT245 K27M KO C2	H3K4me3	35.1M
DIPGXIII Parental	H3K4me3	38.1M
DIPGXIIII K27M KO C5	H3K4me3	44.6M
BT245 Parental	H3K4me1	50.9M
DIPGXIII Parental	H3K4me1	62.2M

This page is available in the following languages:

Creative Commons License De

Attribution 4.0 International (CC BY 4.0)

This is a human-readable summary of (and not a substitute for) the license.

You are free to:

Share — copy and redistribute the material in any medium or format

Adapt — remix, transform, and build upon the material

for any purpose, even commercially.

The licensor cannot revoke these freedoms as long as you follow the license terms.

Under the following terms:

Attribution — You must give appropriate credit, provide a link to the license, and indicate if changes were made. You may do so in any reasonable manner, but not in any way that suggests the licensor endorses you or your use.

No additional restrictions — You may not apply legal terms or technological measures that legally restrict others from doing anything the license permits.

Notices:

You do not have to comply with the license for elements of the material in the public domain or where your use is permitted by an applicable exception or limitation.

No warranties are given. The license may not give you all of the permissions necessary for your intended use. For example, other rights such as publicity, privacy, or moral rights may limit how you use the material.